Numerical and Experimental Investigations of an Oxy-Combustion Carbon Free Power Generation System

BY

BINASH IMTEYAZ

A Dissertation Presented to the
DEANSHIP OF GRADUATE STUDIES

KING FAHD UNIVERSITY OF PETROLEUM & MINERALS

DHAHRAN, SAUDI ARABIA

In Partial Fulfillment of the
Requirements for the Degree of

DOCTOR OF PHILOSOPHY

In

MECHANICAL ENGINEERING

APRIL 2019

KING FAHD UNIVERSITY OF PETROLEUM & MINERALS

DHAHRAN- 31261, SAUDI ARABIA

DEANSHIP OF GRADUATE STUDIES

This thesis, written by **BINASH IMTEYAZ** under the direction of his thesis advisor and approved by his thesis committee, has been presented and accepted by the Dean of Graduate Studies, in partial fulfilment of the requirements for the degree of **DOCTOR OF PHILOSOPHY IN MECHANICAL ENGINEERING.**

Med Habib

Dr. M. A. HABIB
(Advisor)

Hassan Badr

Dr. H. M. BADR
(Member)

Esmail

Dr. E. MOKHEIMER
(Member)

R.B-Mansour

Dr. R. BEN-MANSOUR
(Member)

Dr. HONG G. IM
(Member)

Dr. Z. M. GASEM
Department Chairman

Dr. Salam A. Zummo
Dean of Graduate Studies

24/6/2019

Date

بسم الله الرحمن الرحيم

Dedicated to

My beloved wife & parents, whose love, support and constant prayer brought to me all the success in my life.

ACKNOWLEDGMENTS

"In the name of Allah, the Beneficent, the Merciful"

All praise belongs to Almighty Allah (s.w.t.) for bestowing me with the courage and perseverance to carry out this work sincerely. I thank Almighty Allah for giving me chance to pursue my Ph.D. successfully at King Fahd University of Petroleum and Minerals, Dhahran. I am happy to have had a chance to glorify His name in the sincerest way through this small accomplishment and ask Him to accept my efforts and facilitate me to serve His people with that which He has conferred on me.

My great thanks to King Fahd University of Petroleum and Minerals for providing me good academic platform and financial support during my Ph.D. Special thanks is also due to the KACST-TIC on CCS at KFUPM.

I wish to express my sincere gratitude and appreciation to my thesis advisor and mentor Dr. M.A. Habib for his constant guidance, motivation and support during the course of my studies. His valuable and priceless suggestions made this work interesting and challenging for me. I also wish to express my deep appreciation to Dr. Esmail Mokheimer, Dr. Hassan M. Badr, Dr. Hong G. Im and Dr. Rached Ben Mansour for their help, guidance, and constant encouragement during my PhD. I am also indebted to Dr. Medhat Nemitallah and Dr. Ahmed Abdelhafez for the valuable time he spent throughout my thesis work.

I am very grateful to Dr. Sarim Jamal, Rizwan Khan, Dr. Naef, Dr. Lawal, Zeeshan Alam and Maimoon Atif for their help and encouragement during my Masters. I would also like to acknowledge all the Mechanical Engineering faculty members with whom I took courses

during my PhD., who helped me a lot during my coursework. I also owe thanks to all the students and faculty whom I interacted with during my PhD program.

I am immensely thankful to my beloved wife, Sana, for her support, care and love throughout the ups and downs during the period of my pursuance. She has been my inspiration and motivation to move forward in my quest of knowledge. I would like to express my gratitude to my parents whose prayers and guidance I needed in each and every step of my life. Special thanks to my brother and sister for their love and support and being a source of comfort to me. I would also like to acknowledge all my family members and friends who filled my life joy and mirth.

TABLE OF CONTENTS

LIST OF FIGURES

LIST OF TABLES

ABSTRACT

Full Name : Binash Imteyaz

Thesis Title : Numerical and Experimental Investigations of an Oxy-Combustion Carbon Free Power Generation System

Major Field : Mechanical Engineering

Date of Degree : April 2019

This study proposes a carbon-free power generation system, based on oxy-combustion technology aided with ion transport membrane (*ITM*) reactor. Firstly, a detailed thermodynamic analysis of the system has been conducted to evaluate the performance and efficiency of the system based on the first and second law of thermodynamics. Two basic oxy-combustion cycles are investigated under premixed and non-premixed combustion conditions and the results are compared in terms of exergy destruction, and the first and the second law efficiencies. An air separation unit (*ASU*) is used for oxygen separation from feeding air in the premixed combustion cycle. In the non-premixed cycle, CO_2/H_2O splitting *ITM* reactors are used, where oxygen separation and in situ oxy-combustion processes occur within the reactor. A gas turbine cycle, working on conventional air combustion of methane, was selected as the base case for the comparative study. For the two basic oxy-combustion cycles, losses in the air *ASU* and the condenser were identified to be the main reason for lower efficiencies and, hence, the systems were modified to include heat recuperation cycles for better performance. Two new systems with modified oxy-combustion cycle designs were proposed. First law and second law efficiency of the modified premixed cycle was found to be *42.3%* and *52.8%*, respectively, as compared to

42.7% and *48.7%*, respectively, for the reference air-combustion cycle. The overall thermal and second law efficiency of the modified non-premixed cycle was found to be *37.8%* & *50.4%*, respectively. Keeping in mind the effect of hydrogen enrichment on the reaction rate and flame behavior, a priori explorations on its effect on the thermodynamic efficiencies of the oxy-combustion cycles were conducted. It was observed that increasing hydrogen fraction in the fuel blend increases the first and second efficiency, however, the effect was only marginal.

The experimental investigations on the combustion behavior and determination of the stability map of turbulent premixed H_2-enriched oxy-methane flames in a model gas turbine combustor were conducted. Static stability limits, in terms of flashback and blow-out limits, are recorded over a range of hydrogen fraction (*HF*) at fixed oxygen fraction (*OF*) of *30%* and fixed inlet bulk velocity of *5.2 m/s*, and the results are compared with the non-enriched case (*HF=0%*). The static stability limits are also recorded for different inlet bulk velocity (*4.4, 5.2, and 6 m/s*) and the results are compared to explore the effect of flow dynamics on operability limits of H_2-enriched flames. The stability maps are presented as a function of equivalence ratio (*0.3 to 1.0*) and *HF* (*0% to 75%*) plotted on the contours of adiabatic flame temperature (*AFT*), power density (*PD*), inlet Reynolds number (*Re*) and reacting mixture mass flow rate ($\dot{m}$) to understand the physics behind flashback and blow-out phenomena. Flame shapes are recorded using a high-speed camera and compared for different inlet velocities to explore the effects of H_2-enrichment and equivalence ratio on flame stability. The equivalence ratio at which a transition of flame stabilization from the inner shear layer (*ISL*) to the outer recirculation zone (*ORZ*) occurs is determined for different inlet bulk velocities. The value of the transition equivalence ratio was observed

to reduce while increasing the inlet bulk velocity. Flame shapes near flashback limit, as well as near blow-out limit, are compared to explore the mechanisms of flame extinction. Flame shapes are compared at fixed adiabatic flame temperature, fixed inlet velocity, and fixed flow swirl to isolate their effects and investigate the effect of kinetic rates on flame stability. It was found that the hydrogen enrichment augmented the operability window and increased the stability of oxy-flames.

Finally, a numerical study on the combustion characteristics of a premixed oxy-flame in a swirl-stabilized combustor was conducted to investigate the effect of hydrogen enrichment in methane flames. Large Eddy Simulation (*LES*) methodology was implemented to model the premixed turbulent flames in the model gas turbine combustor. The results indicated that with the hydrogen enrichment, the combustion is characterized by the typical *V*-shape swirl stabilized flames with strong inner recirculation zones. Reaction rates are enhanced, and the flames tend to be more compact and intense with the increase in hydrogen percentage until the flashback is observed. Moreover, the hydrogen enrichment increases the critical rate of strain and diminishes the possibility of flame quenching. Higher hydrogen fraction flames are also characterized by higher Damkohler number (>1000) and lower Karlovitz number (<1), indicating that the flame thickness is smaller than the smallest eddy present in the flow. The reaction is, thus, dominated by the chemical reaction rate and turbulence does not to alter the inner flame structure. The effect of equivalence ratio, Reynolds number and swirl number on the flame structure and combustion characteristics are also presented and discussed in detail.

ABSTRACT (ARABIC)

أدى خطر الاحتباس الحراري إلى إثارة ضجة في عالم الأبحاث، مع رواد من جميع أنحاء العالم، يشاركون في السباق لتخفيف انبعاثات الكربون في البيئة. يعد حرق الوقود بالأكسجين من أكثر التقنيات الواعدة والفعالة لاحتجاز الكربون نظرًا لخصائصه التي تشبه احتراق الهواء ويمكن إعادة تركيبه بسهولة في المصانع الحالية مع تعديلات طفيفة. تقترح هذه الدراسة نظامًا لتوليد الطاقة خالٍ من الكربون، استنادًا إلى تقنية احتراق الأكسجين بمساعدة مفاعل غشاء النقل الأيوني (*ITM*). أولاً، تم إجراء تحليل مفصل للديناميكا الحرارية للنظام لتقييم أداء وكفاءة النظام بناءً على القانون الأول والثاني للديناميكا الحرارية. يتم التحقيق في دورتين أساسيتين للاحتراق بالأكسجين في ظل ظروف الاحتراق المخلوط وغير المخلوط وتتم مقارنة النتائج فيما يتعلق بتدمير الطاقة وفعالية القانون الأول والثاني. يتم استخدام وحدة فصل الهواء (*ASU*) لفصل الأكسجين عن الهواء المغذي في دورة الاحتراق مسبقة الخلط، ومفاعلات *ITM* لفصل بخار الماء وثاني أكسيد الكربون، حيث يحدث فصل الأكسجين وعملية الحرق بالأكسجين في نفس الموقع داخل المفاعل، في الدورة غير مسبقة الخلط. تم اختيار دورة التوربينات الغازية، التي تعمل على احتراق الميثان بالهواء التقليدي، كحالة دراسة أساسية للمقارنة مع باقي الحلات.

بعد ذلك، تم إجراء التحقيقات التجريبية حول سلوك الاحتراق وتحديد خريطة ثبات لهب الميثان والأكسجين المخلوط مسبقا والمخصب بالهيدروجين داخل نموذج توربين غازي. يتم تسجيل حدود الثبات الاستاتيكي، من حيث انعكاس اللهب الخلفي وخروج اللهب، على مدى من نسبة الهيدروجين (*HF*) عند نسبة أكسجين ثابتة (*OF*) بنسبة 30% وسرعة مجمعة ثابتة عند المدخل تبلغ 5.2 م/ث، وتم المقارنة مع حالة الخليط غير المخصب (*HF=0%*). يتم أيضًا تسجيل حدود الثبات الاستاتيكي لسرعات دخول مختلفة (4.4، 5.2، و 6 م/ث) وتتم مقارنة النتائج لاستكشاف تأثير ديناميكا التدفق على حدود قابلية التشغيل للهب المخصب بالهيدروجين. يتم تقديم خرائط الثبات كدالة في نسبة التكافؤ (من *0.3* إلى *1.0*) ونسبة الهيدروجين (من *0٪* إلى *75٪*) المرسومة على معالم درجة حرارة اللهب القصوى (*AFT*) وكثافة القدرة (*PD*) ورقم رينولد عند المدخل (*Re*) ومعدل تدفق الكتلة الخليط المتفاعل ($\dot{m}$) لفهم الفيزياء وراء انعكاس اللهب الخلفي وظاهرة خروج اللهب. يتم تسجيل أشكال اللهب باستخدام كاميرا عالية السرعة ومقارنتها عند سرعات مدخل مختلفة لاستكشاف آثار إثراء الهيدروجين ونسبة التكافؤ على استقرار اللهب. يتم تحديد نسبة التكافؤ عند

انتقال استقرار اللهب من طبقة القص الداخلية (ISL) إلى منطقة إعادة الدوران الخارجي (ORZ) عند سرعات مدخل مختلفة. انخفضت قيمة نسبة التكافؤ التي يحدث عندها هذا الانتقال مع زيادة سرعة الدخول. تم مقارنة أشكال اللهب بالقرب من حد انعكاس اللهب الخلفي، وكذلك بالقرب من حد خروج اللهب، لاستكشاف آليات انقراض اللهب. تم مقارنة أشكال اللهب عند درجة حرارة لهب قصوى ثابتة، وسرعة مدخل ثابتة ومعدل ثابت لتدوير التدفق وذلك لعزل آثارها والتحقيق في تأثير معدلات التفاعلات على استقرار اللهب.

أخيرًا، أجريت دراسة عددية حول خصائص الاحتراق في لهب الأكسجين مسبق الخليط في احتراق مثبت الدوامة لبحث تأثير تخصيب الهيدروجين في لهب الميثان. تم تطبيق منهجية حسابات الدوامات الكبيرة (LES) لدراسة ألسنة اللهب المضطرب والمخلوط مسبقا داخل نموذج توربين غازي. أشارت النتائج إلى أنه مع تخصيب الهيدروجين، يتميز الاحتراق بنيران مستقرة دوامياً على شكل حرف V وذات منطقة إعادة تدوير داخلية قوية. تم تحسين معدلات التفاعل، وتميل النيران إلى أن تكون أكثر إحكاما وكثافة مع زيادة نسبة الهيدروجين، حتى يتم ملاحظة ارتجاع اللهب. علاوة على ذلك، فإن تخصيب الهيدروجين يزيد من معدل الإجهاد الحرج ويقلل من إمكانية إخماد اللهب. تتميز نيران اللهب ذات نسبة الهيدروجين العالي أيضًا بعدد دامكولار عالي وعدد كارلوفيتز منخفض، مما يشير إلى أن سماكة اللهب أصغر من أصغر دوامة موجودة في التدفق. وبالتالي، يكون اللهب معتمداً على معدل التفاعل الكيميائي ويكون اضطراب السريان غير قادر على تغيير هيكل اللهب الداخلي. كما تم عرض تأثير نسب التكافؤ ورقم رينولد ورقم الدوامة على هيكل اللهب وخصائص الاحتراق ومناقشتها بالتفصيل.

CHAPTER 1

INTRODUCTION

1.1 Research Background

Since the industrial revolution, the dependence on fossil fuel is on rise to meet the insatiable energy demand of the world. Although new technological developments have made the non-conventional energy resources very promising alternatives for energy supply, near future still envisages conventional sources of energy as the primary energy source. The unstinted and artless burning of fossil fuels poses some of the most detrimental impacts on the environment and the eco-system and raised the question on the balance nature has meticulously evolved though eras. Tons of industrial waste gases that are dumped to the atmosphere are affecting the very fabrics of nature among which the most alarming one is global warming. The climatic pattern of the globe is drastically affected by global warming, causing natural disasters like floods, droughts, forest-fires etc. more unpredictable and frequent. Apart from that, the rise in global average temperature is melting the polar ice-caps and glaciers. This large-scale meltdown is responsible for the rise in the sea level and endangering millions of square miles of low-lying coastlines. The last century has observed an average global temperature rise $0.8\ ^{o}C$ [1], resulting in an enormous amount of galactic and polar ice to melt. Meltdown has caused an average rise of more than six inches in the sea level and is predicted that it may further increase by *20* feet by *2100* [2]. Scientists predict that with the melting of ice sheets of Greenland and Antarctica, sea level rise could be more than *20* feet by *2100* compared to the sea level of today [2].

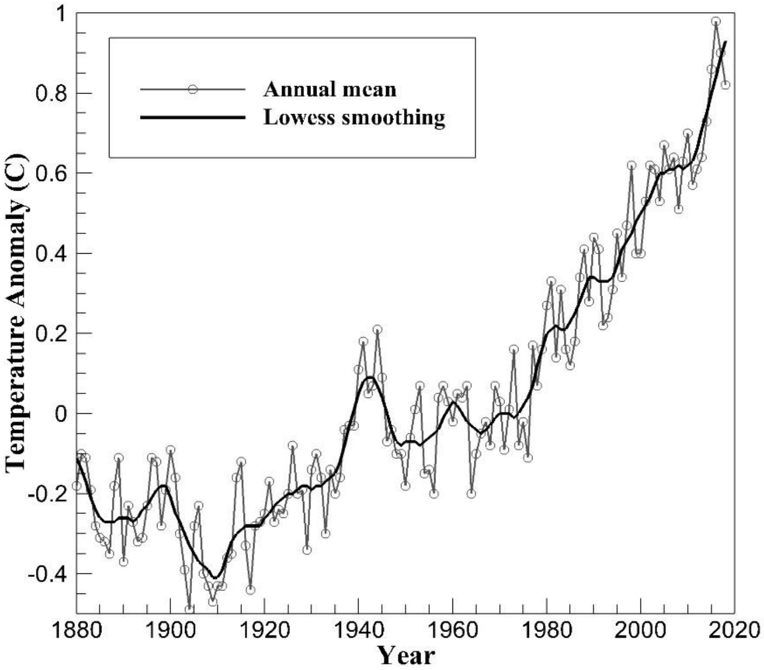

Figure 1. Average Global Temperature over the last century [1]

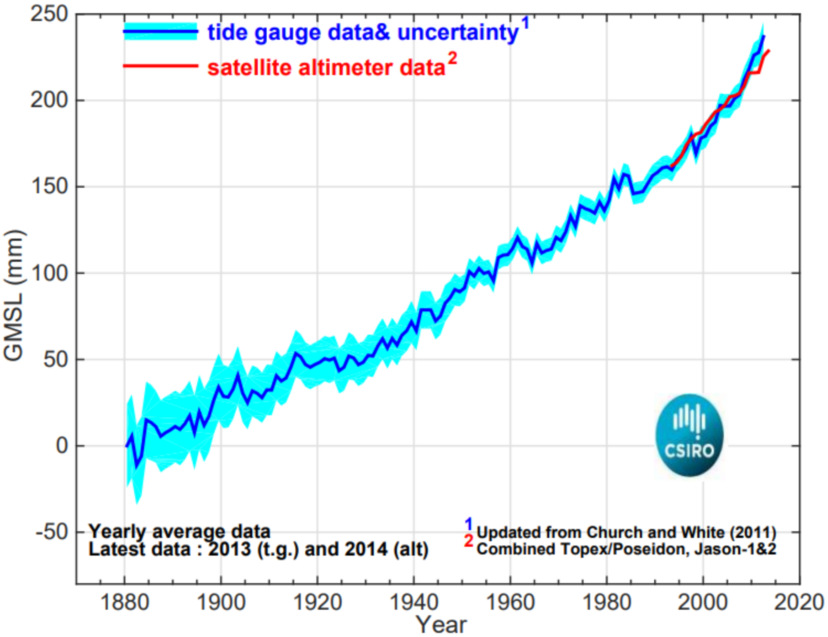

Figure 2. Global Average Absolute Sea level has risen by an alarming magnitude of *9* inches from 1870-2008 [3]

It is well known and established that the main reason for global warming is the emissions of greenhouse gases into the environment. Among the various activities that contribute to the emissions of these harmful gases is the burning of fossil fuels in various power plants, industries, automobiles etc. It is forecasted that fossil fuels will be the dominant contributor to energy supplies for various energy-intensive sectors for the next decades throughout the world [4]. Moreover, carbon dioxide is the main component of flue gas and contributes to around *77%* of Global Green House emissions [2]. Moreover, as the industrial units are still mainly dependent on the conventional sources of energy, it is expected that carbon dioxide emissions will continue to rise up to *70%* by the year *2050* [5]. Hence, there is an immediate need to check the CO_2 emission than it is too late. The threat has attracted the scientists and researchers around the world towards the peril pertaining to the CO_2

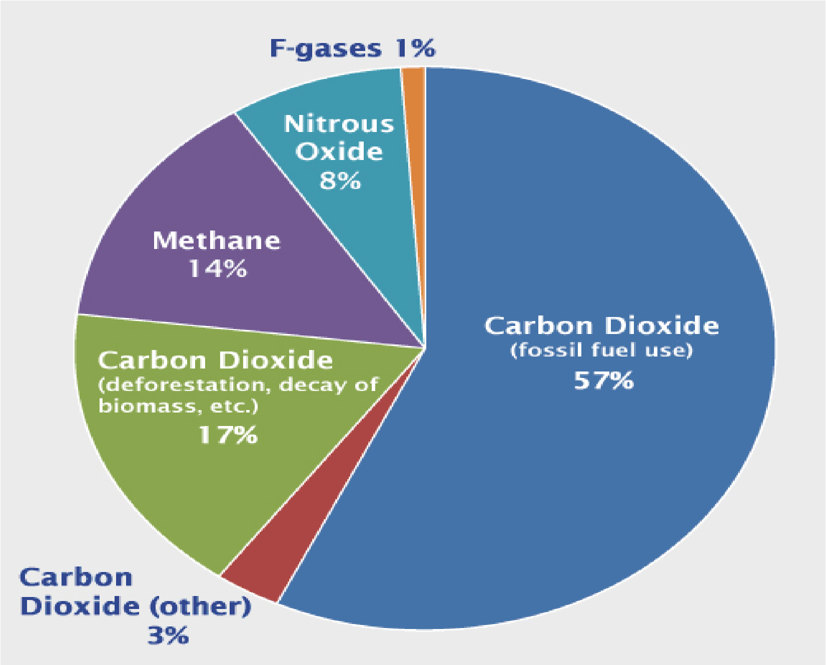

Figure 3. Relative percentage of greenhouse gases [6]

emissions and desperate measures are being taken to tackle this problem. Carbon capture & sequestration (*CCS*) technologies are being investigated to provide cost-effective and efficient ways to capture CO_2 from large point sources and subsequently transfer to proper storage. The three main categorizations of carbon capturing technologies can be stated as: (i) Post-combustion decarbonization (ii) Oxy-fuel combustion & (iii) Pre-combustion decarbonization. However, carbon capture technologies are still in its nascent stage and are not developed enough to be implemented economically in commercial units. Currently, the maximum efficiency of the power plants running with *CCS* is around *35%* [7], where the efficiency loss is of order *7-11%* [8]. Hence, it is of immense importance to revisit the *CCS* technologies and answer the challenges it is facing in the current phase.

1.2 Objectives

The objectives of this research can be summarised as follows:

- To propose a carbon-free power generation system based on oxy-combustion technology, aided with *ITM* integrated reactor.
- To perform a detailed analysis of the system to evaluate the performance of the power cycle based on the first law and second law of thermodynamics and to investigate the effect of hydrogen enrichment on the cycle efficiencies.
- To study the characteristics of premixed oxy-combustion of hydrogen-enriched methane and evaluate the effects of hydrogen enrichment, equivalence ratios and throat velocities on the flame.
- To map the static stability of hydrogen-enriched flame by finding the lean blowout limits and flashback limits.

- To develop a *CFD* model to simulate the premixed oxy-combustion of hydrogen-enriched flame and validate it with the experimental results.
- To extend the parametric study to delve further into the combustion characteristics of premixed oxy-combustion of hydrogen-enriched methane.

1.3 Thesis Outline

In this research work, a carbon-free power generation system is proposed based on oxy-fuel combustion and utilizing Ion Transport Membrane (*ITM*) technology for air separation. Thermodynamic analysis of the system based on the first law and second law of thermodynamics was conducted on the premixed and the non-premixed combustion configurations. Moreover, experimental and numerical investigations on premixed oxy-combustion of hydrogen-enriched methane in a model gas turbine reactor have been conducted.

Chapter 1 introduces to the threats and concerns of global warming and the current steps taken in efforts to mitigate the greenhouse gases emissions. The chapter further includes the motivation of the present work and defines the objectives of this thesis.

Chapter 2 discusses the current status of carbon capture technologies, prior researches conducted on the thermodynamic analysis of the oxy-combustion system as well as experimental and numerical investigations on combustion characteristics of premixed oxy-flames.

Chapter 3 describes the problem statement and the objectives of the present research work.

Chapter 4 includes the detailed theory behind the model development for the thermodynamic analysis and the computational fluid dynamics analysis. A brief summary of the governing equations and applied mathematical models have been discussed.

Chapter 5 proposes power generation systems based on oxy-combustion with premixed and non-premixed combustion configurations. The thermodynamic analysis of the systems is conducted to evaluate the energy and exergy losses in the proposed cycles. The systems are modified to minimize the exergy losses and results are compared with a conventional base case power cycle.

Chapter 6 defines the experimental setup of the premixed laboratory scale gas turbine model combustor. The static stability of hydrogen-enriched flames is studied by identifying the blowout and flashback points at various hydrogen fractions, equivalence ratios, and throat velocities. The flame visualization is obtained by capturing flame images using a high definition camera and the effects of various parameters are discussed.

Chapter 7 presents the numerical model developed to simulate the oxy-combustion in the model gas turbine reactor. The model is validated against the experimental data and various parametric studies are presented. Effects of hydrogen fractions in the fuel blends, equivalence ratios and throat velocities on the flow field, reaction rates, laminar flame speed etc. are analyzed and presented.

Chapter 8 gives the concluding remarks of the present study and suggests the recommendations for the future investigations.

CHAPTER 2

LITERATURE REVIEW

In an effort to control CO_2 emissions into the environment, researchers and scientists around the globe are exploring various technologies and solutions. One of the efficient ways to mitigate the *GHGs* emissions, from the conventional existing plants, is to implement carbon capturing and sequestration techniques. The best part of the *CCS* technologies is that they can be retro-fitted with the existing systems with slight modifications. However, there is an energy cost associated with these techniques which reduces the system efficiency. A brief description highlighting the pros and cons of *CCS* technologies is presented in the following sections.

2.1 Carbon Capture and Sequestration (*CCS*) Technologies

Carbon capture technologies have been broadly classified into three major categories based on the stage when carbon is removed from the cycle. The three classifications are (i) Pre-combustion, (ii) Post-combustion, and (iii) Oxy-combustion. The different features of these technologies are described in the following sub-sections.

2.1.1 Pre-combustion

In pre-combustion, the carbon content from the fuel is removed prior to the combustion of the fuel and hence, during combustion no CO_2 is formed. Pre-combustion is already in use in the chemical and refining industries for the production of hydrogen for more than *50* years [9]. The idea is to perform the gasification of the fuel in the presence of steam and air to partially oxidize the fuel to get carbon monoxide and hydrogen (synthesis gas). The carbon monoxide is further oxidized in the presence of steam in another reactor, known as shift reactor, to get carbon dioxide and more hydrogen is produced. The carbon dioxide is separated from the mixture and stored in the pressurized vessels for further utilization in the chemical industries or transferred for the sequestration process. The separated hydrogen is a carbon-free fuel with high calorific value and can be utilized in a reactor or a gas turbine to get a carbon-free energy system. Pre-combustion can be employed with an Integrated Gasification Combined Cycle (*IGCC*) plant, which uses natural gas and coal as fuels.

2.1.2 Oxy-fuel Combustion

Oxy-combustion process focusses on the treatment of the oxidizer instead of the fuel to get rid of carbon dioxide emission. Nitrogen is filtered out from the air prior to the combustion through the liquefaction process or membrane separation process using oxygen transport membrane (*OTM*) technique [10]. Thus, the combustion takes place in pure oxygen so that the combustion products mainly consists of CO_2 and H_2O, from where CO_2 can easily be separated from the mixture by the condensation process. However, combustion in pure oxygen results in a very high flame temperature, which can be harmful to the reactor wall and equipment. Hence, a part of flue gas (which mainly is CO_2) is recirculated into the reactor with the oxidizer to reduce the flame temperature. However, CO_2 having quite different thermophysical and radiative properties than that of nitrogen, the dynamic and thermal properties of the oxy-combustion fuel is quite different from the conventional combustion. Hence, this area requires extensive investigations to make the technology be retro-fitted to the existing plants. Although oxygen separation technologies at this stage are

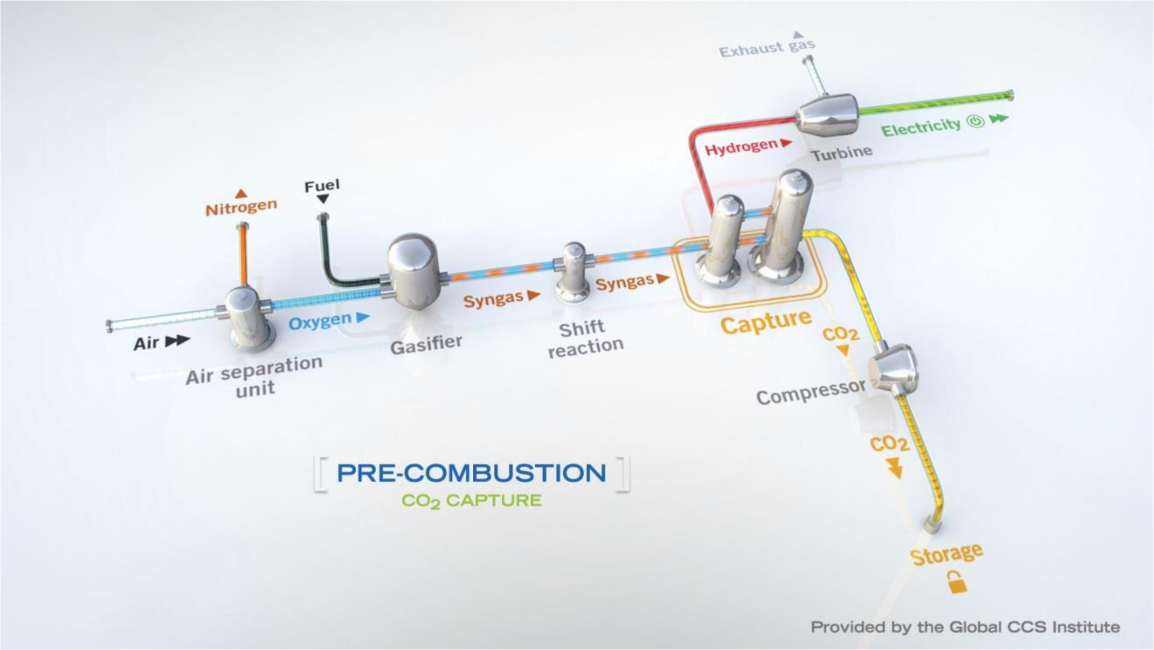

Figure 4. Schematic of Pre-combustion technique [12]

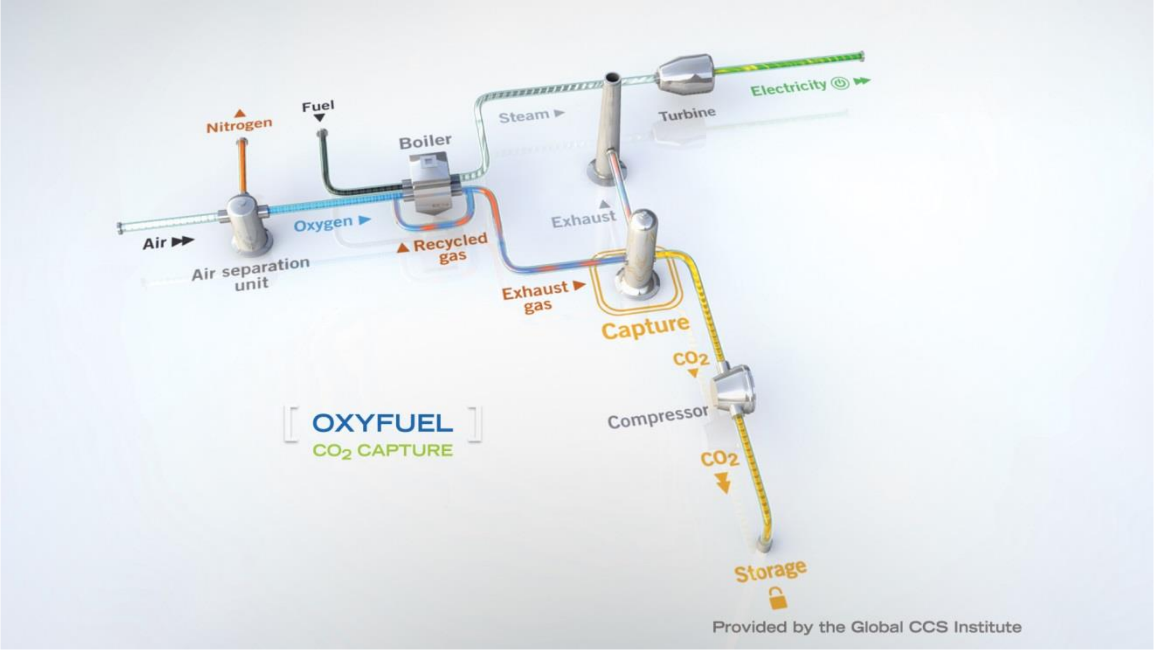

Figure 5. Schematic of Oxy-combustion technique [12]

energy intensive, contributing to a major fraction of the energy requirement, studies show that oxy-fuel combustion is feasible with the current technologies [11].

2.1.3 Post Combustion

In this process, no meddling up with the combustion process is required and the fuel is burned in the air as in conventional combustion. The idea is to capture carbon dioxide from the flue gases by absorption of CO_2 in liquid solvents, such as amine solutions. Presence of a high percentage of oxides of nitrogen and sulfur in the exhaust gases reduces the efficiency of amine solutions by forming stable and non-regenerable salts with the amines. Hence, it is required for the plants, using post-combustion carbon capturing system using amine solutions, to have de-NO_x and flue gas desulfurization facilities to get rid of these inhibitors.

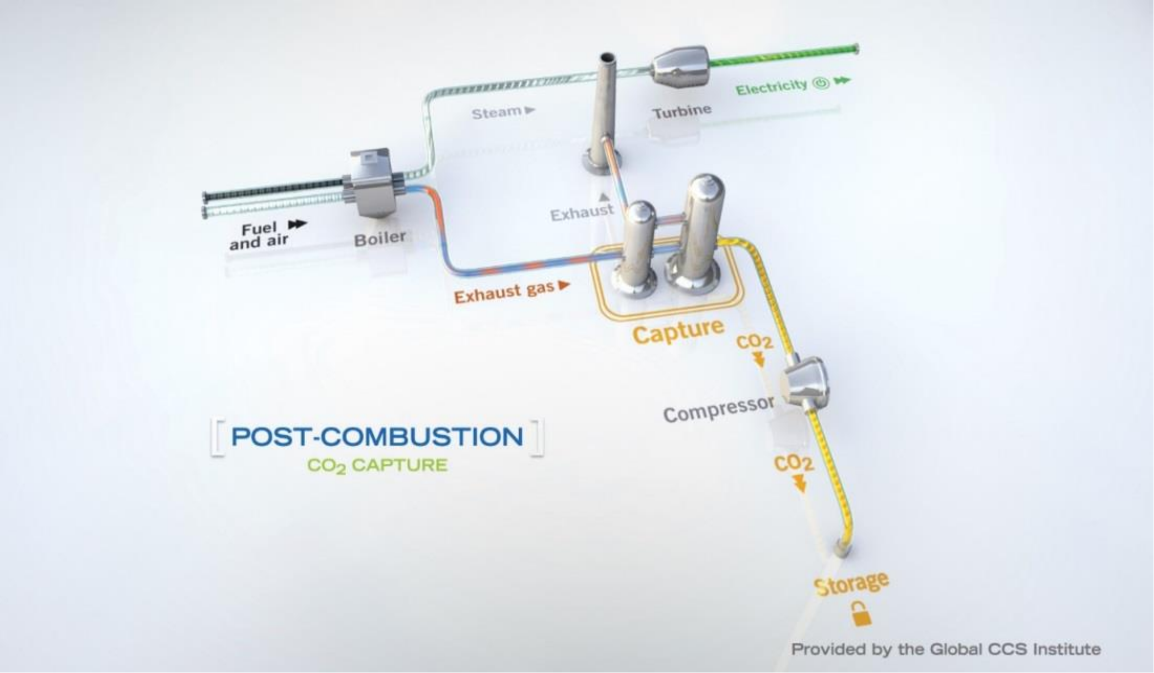

Figure 6. Schematic of Oxy-combustion technique [12]

Currently, post-combustion technology is employing organic solvents such as monoethanolamine (*MEA*) in a natural gas combined power plant and a modern pulverized coal power plant [9,13–15]. The solvent is regenerated and recycled back into the carbon capture process, resulting in a closed scrubbing cycle.

Many endeavoring efforts on using metal-organic frameworks (*MOFs*) as a post-carbon capturing material have earned them a good reputation in the research world [16]. *MOFs* are new class crystalline compounds made up of metal ions coordinated to organic ligands. These materials are characterized by a highly porous structure with great potential as adsorbents. Some *MOFs* have a selective affinity to CO_2 and are under the research stage for capturing and separating CO_2 from the flue gases. One of the biggest advantages of the post-combustion technologies is that they can easily be retrofitted to an existing plant without interfering with the reactor design by just installing the capturing unit in the exhaust system.

2.2 Thermodynamic Analysis of Oxy-fuel Power Generation System

Oxy-fuel combustion technology is considered to be a feasible tool for reducing greenhouse gas (*GHG*) emissions [17–21]. Thermodynamic analysis of oxy-fuel combustion based power generation system can be found in the literature [8,11,22,23]. Due to low second law efficiency of commercial cryogenic air separation technology, the thermal efficiency of a carbon capture and sequestration (*CCS*) based system may suffer an efficiency loss of up to 8.5 % as compared to the natural gas combined cycle (*NGCC*). Hence, cost-effective air separation technology has remained the focus of research for many of the scientists working on *CCS* integrated technologies.

2.2.1 Conventional Air Separation Technology

Simpson and Simon [8] carried out a comparative study of second law analysis of CO_2 separation technologies via oxy-fuel combustion and post-combustion carbon capture. They used a simple supercritical steam power plant using methane and propane as fuels as the base model. The effect of hydrogen to carbon ratios (*H/C*) on the energy consumptions by the separation units were investigated and the performance of oxy-fuel combustion and post-combustion configurations operating with coal were predicted by extrapolating the results. A black box model of the separation units with the isobaric and isothermal condition at the environmental dead state temperature and pressure were assumed. This assumption simplifies the 2^{nd} law analysis of the separation units by removing the complexity arising due to "carry through" exergy. Their findings show that the post-combustion separation and oxy-fuel combustion using methane as fuel reduce the system efficiency by *7.4%* and *8.9%*, respectively, while *8.2%* and *8.8%* efficiency loss was recorded for both the configurations respectively, using propane. Reduced efficiency of the post-combustion system using propane was accounted for higher carbon content per unit exergy than methane, resulting in higher power demand in the carbon separation unit (*CSU*) and sequestration compressor. Same is the case for the oxy-fuel system, however, this increased power requirement is counter-balanced by the decreased power requirement by the air separation unit (*ASU*) as the stoichiometric combustion of propane has lesser oxygen requirements per unit exergy of the fuel. Based on the results discussed above, they concluded that for fuels with higher carbon content per unit fuel exergy, the oxy-fuel system becomes more viable. Also, there exists a tipping-point equivalence ratio, which is a function of fuel carbon content and stoichiometric oxygen requirement per unit exergy of fuel, where the efficiency of the oxy-fuel combustion system exceeds the post-combustion separation configuration.

Thermodynamic analysis of a novel H_2 production technology using *CaO* sorption enhanced methane steam reforming (*SEMSR*) thermally coupled with chemical looping combustion (*CLC*) was presented by Zhu and Fan [24]. Higher purity of hydrogen can be obtained by the incorporation of *CaO* sorbent which captures CO_2 from the reformer gas to the solid phase. They used Aspen plus software package to simulate the *CLC-SEMSR* process and to assess the thermodynamic performance of the system. Total exergy of the endothermic units was calculated by:

$$\sum Ex = \left(1 - \frac{T_o}{T}\right) \sum E_i \tag{1}$$

where T and T_o represent the working temperature and the reference temperature, respectively, and $\sum E_i$ represents the sum of energy required by each unit. Physical (Ex_{ph}) and chemical exergy of material streams was calculated using the following equations:

$$Ex_{ph} = \left(H - H_o\right) - T\left(S - S_o\right) \tag{2}$$

$$Ex_{ch} = \sum y_i Ex_{o,i} + RT_o \sum y_i \ln y_i \tag{3}$$

where, *H* and *S* represents the enthalpy and entropy flow of the material stream, $Ex_{o,i}$ represents the chemical exergy of component *i* in Szargut’s reference environment model and y_i represents the molar fraction of component *i*. They found that the energy efficiency of *CLC-SEMSR* is higher with a value of *83.3%* as compared to that of *CLC-MSR* process with the efficiency of *80.6%*. Also, significantly pure H_2 *(95%)* was obtained at a comparatively lower temperature of *655 °C* with *CLC-SEMSR* technology as a comparison to *CLC-MSR* process which yields H_2 with *77.1%* purity at *900 °C*.

Exergy analysis of membrane reactor and water gas shift reactor for the production of hydrogen from natural gas was conducted by Atsonios et al. [25]. Their results suggest a total net energy efficiency of 50.65% of the system with almost *100%* CO_2 capture while the second law efficiency of the plant was found to be 48.23%. Highest exergy dissipation was contributed by the gas turbine (*GT*), the autothermal reactor *(ATR*) and the process of rich-CO_2 stream purification units. Although the air separation unit (*ASU*) requires a high amount of energy, little irreversibilities were exhibited by the unit. It was asserted that low stream to carbon ratio and high syngas delivery temperature enhance exergetic and energetic efficiency of the system. Furthermore, they concluded that the use of membrane assisted water gas shift (*WGS*) reactors is one of the most exergetically efficient carbon separation technology as the exergy loss in both the membranes and high-temperature *WGS* was found to be *2%* of the total exergy input in the system.

A high efficiency combined cycle power generation system (*CCPS*) integrated with a heat recovery steam generator, based on the oxy-combustion CO_2 capturing technology, was proposed by Pak et al. [26]. The advantages of the proposed system are high temperature working fluid, the need of compressor unit for the working fluid is obliterated, power generation is much higher than the conventional steam turbine power generation system, and highly efficient carbon capture with no NO_x formation in the oxy-combustion power generation system. Their calculations show that the proposed system enhances the power output by *23.2%* while reducing the CO_2 emission by *26.8%* with only *1.2%* efficiency loss, in comparison to the original *CCPS*. The power generating system was then modified based on the exergetic flow analyses in order to improve the power generation characteristics and CO_2 reduction capacity. The power output of the modified system was increased by *33.6%* with the same turbine inlet temperature with the reduction of *32.5%* CO_2 emission at the efficiency loss of *1.58%*, as compared to the original *CCPS*.

Fu and Gundersen [27] performed an exergy analysis of an oxy-combustion process for a supercritical pulverized coal-fired power plant with CO_2 capture. They found that the exergy loss is maximum in the combustor followed by the steam generation & reheat process and the steam turbines. Integration of CO_2 capture with the power plant costs an efficiency loss of *10.2%* points, with the air separation unit (*ASU*) contributing to 6.6% points and the CO_2 purification and compression unit (*CPU*) contributing to 3.4% points. However, the theoretical efficiency penalty related to the CO_2 capture was calculated to be only *3.4%*. The largest exergy loss related to both *ASU* and *CPU* was found to be in the compression process and hence, the overall efficiency of the CO_2 capture system can be increased by improving the performance of the compressors. They concluded that the net power efficiency can be improved by *0.2%* points by heat integration between the *ASU* and the *CPU*.

Their further investigations focused on the reduction of power consumption in the air separation unit, as the results show that the *ASU* contributes the maximum to the efficiency loss [28]. They performed an exergy analysis of a double-column distillation process, which is a low purity (*95%*) oxygen production process and investigated various measures for the improvement of *ASU* performance. They found that the highest exergy loss is accounted for the air compression unit and the air distillation process with *38.4%* and

28.2% of the total loss, respectively. The specific power consumption of the compressor unit could be decreased by *19%* by increasing the isentropic efficiency of the unit from *0.74* to *0.9*. Furthermore, the exergy losses in the air compression unit and the distillation unit could be reduced by *17.2%* and *14.7%*, respectively, by the insertion of an intermediate reboiler in the low-pressure column. They concluded that a reduction of *10%* specific power consumption for O_2 production can be achieved by employing the above-mentioned modifications.

In another investigation, they conducted a comprehensive exergy analysis for a coal-based oxy-combustion plant with carbon capture [29]. They showed that the largest exergy loss is accounted for the compression processes and the overall efficiency of the system can be increased by increasing the isentropic efficiency of the compressor, however, this modification is limited to the manufacturer's design and not in the scope of the plant designer. They also suggested that the waste heat from the compressor units can be integrated with a steam cycle by preheating the boiler feedwater is an effective way to improve the performance of the system. The thermal efficiency could be increased by 0.72% points by applying this modification, however, the heat integration problem is complex and further optimization was suggested.

2.2.2 ITM-based Air Separation Technology

Due to low second law efficiency of commercial cryogenic air separation technology, the thermal efficiency of carbon capture and sequestration (*CCS*) based system may suffer an efficiency loss of up to 8.5 % as compared to the natural gas combined cycle (*NGCC*).

Hence, cost-effective air separation technology has remained the focus of research for many of the scientists working on *CCS* integrated technologies.

The ability of ion transport membranes (*ITMs*) to selectively allow for oxygen separation with high purity at low energy cost, has made this technology for oxygen separation as one of the most promising alternatives of conventional cryogenic separation [30,31]. These perovskite membranes require oxygen chemical gradient across the surfaces to drive the oxygen permeation through the membranes. Moreover, the operating temperature should be maintained in the range from *800* to $950\ ^{o}C$ to ensure proper oxygen ion mobility in the lattice. Many attempts have been made to operate these membranes for oxygen separation using sweep inert (non-reacting) gases with reported oxygen permeation flux in the range from *0.01* to $1.0\ \mu mol/cm^2s$ [32–34]. However, for the ITM technology to be economically viable for the existing power generation systems, the required oxygen flux should be around $7\ \mu mol/cm^2s$, which is significantly higher. The oxygen permeation rate can, however, be enhanced significantly by creating a high oxygen partial pressure gradient across the membrane. This can be achieved through combing both the oxygen separation and the combustion processes in one unit called oxygen transport reactor (*OTR*), where in-situ oxy-combustion of the sweeping fuel occurs at the permeate side of the membrane using the permeated oxygen. Oxygen consumption in the combustion process creates low oxygen partial pressure at the permeate side resulting in significant improvement of the oxygen permeation flux [33].

Thermodynamic analysis of a system is crucial to assess its feasibility and success as a power generation technology. Several attempts have been made to evaluate the practicality of oxy-combustion based plants utilizing air separation units (*ASUs*) via conventional cryogenic separation [35–38] as well as membrane technologies [39–41]. Xiong et al. [35] found an exergy efficiency loss of *4.08%* in a pulverized-coal-fired power plant, using cryogenic air separation, as compared to a conventional system. They further concluded that the exergy cost of the components is *10%* higher in the oxy-combustion system than the conventional system due to additional power consumption for the air separation [36]. Moreover, the unit thermo-economic cost of the product for a component in the oxy-combustion system was found to be *1.22* times higher than that for the same component in the conventional system due to the additional monetary cost incurred due to the implementation of the oxy-combustion system. Effect of implementation of membrane technology for air separation has also been reported in some studies with varying opinions. Pfaff and Kather [39] reported slightly better exergetic efficiency of the oxy-combustion system with cryogenic air separation unit as compared to with the membrane *ASU*. However, thermo-economic analysis conducted by Osikowska et al. [41] shows 1.1% higher efficiency of a hybrid membrane-cryogenic separation based system as compared to only cryogenic separation based system. Castillo [40] also reported that with proper thermal integration, around *4%* higher efficiency can be achieved using high-temperature membrane separation technology than through conventional cryogenic separation.

A detailed analysis of an *ITM*-based power cycle and intermediate fidelity model of air separation unit using *ITM* are presented by Mancini and Mitsos [33]. The flux of oxygen vacancy was given by Fick's law as:

$$J_v = -\frac{\sigma_v}{4F^2}\nabla\mu_v = -D_v\frac{dC_v}{dy} \qquad (4)$$

where σ_v represents the oxygen ion conductivity, *F* is the Faraday's constant, μ_v is the chemical potential of oxygen vacancy, D_v is the oxygen vacancy diffusion coefficient, C_v is the oxygen vacancy concentration, and *y* is the coordinate axis normal to the membrane surface. The oxygen flux $\left(J_{O_2}\right)$ is negative of the flux of oxygen vacancy $\left(J_v\right)$ and the local oxygen flux can be obtained by integrating the above equation as:

$$J_{O_2} = \frac{D_v}{2L}\left(C_v'' - C_v'\right) \tag{5}$$

where, C_v'' and C_v' are the local vacancy concentrations at the feed side and the permeate side, respectively. Thus, oxygen transport along the membrane can be given by a simplified equation, as a function of partial pressure of oxygen on each side and forward and backward surface exchange rate constants, k_f and k_r as:

$$J_{O_2} = \frac{D_v k_r \left[\left(P_{O_2}'\right)^{1/2} - \left(P_{O_2}''\right)^{1/2}\right]}{2tk_f\left(P_{O_2}' P_{O_2}''\right)^{1/2} + D_v\left[\left(P_{O_2}'\right)^{1/2} - \left(P_{O_2}''\right)^{1/2}\right]} \tag{6}$$

The volumetric flow rate of oxygen at the permeate side is given by the conservation equation for O_2:

$$\dot{n}_{i+1,O_2} = \dot{n}_{i,O_2} + \phi A_i J_{i,O_2} + \phi V_i R_{i,O_2}''' \tag{7}$$

where *n* is the molar flow rate of oxygen, J_{i,O_2} is the local oxygen flux, and R_{i,O_2}''' is the local oxygen production rate because of the chemical reaction. Energy balance to account for the First Law of thermodynamics is given in terms of the molar enthalpies of the species

($\bar{h}$), convective heat transfer of the streams ($\dot{Q}_i$) and the enthalpy stream ($\dot{H}_{i,O_{2,ext}}$) of the oxygen permeating from the feed side to the sweep side.

$$\sum_j \dot{n}_{i+1,j}\bar{h}_j\left(T_{i+1}\right)=\sum_j \dot{n}_{i,j}\bar{h}_j\left(T_i\right)-\dot{Q}_i+\dot{H}_{i,O_{2,ext}} \tag{8}$$

The Second Law of thermodynamics is applied to account for the entropy generation due to chemical and thermal energy conversion, thermal equilibration, pressure drop and mixing of different species.

$$\dot{S}_{gen}=\sum_{Outlets}\dot{n}_j\bar{s}_j\left(T,P_j\right)-\sum_{Inlets}\dot{n}_j\bar{s}_j\left(T,P_j\right) \tag{9}$$

$$\bar{s}_j\left(T,P_j\right)=\bar{s}_j^o+\int_{T_o}^{T}\frac{\bar{C}_{pj}\left(T'\right)}{T'}dT'-R\ln\left(\frac{P_j}{P_{ref}}\right) \tag{10}$$

Mancini and Mitsos [42] performed the thermodynamic analysis of ion transport membrane reactors (*ITM*) for the reactive case and separation-only case with co-current and counter-current *ITM*s for both the cases. The feed stream was set with the inlet temperature corresponding to the lower bound of the *ITM* operation temperature (*i.e. 973 K*) and the permeate stream was set with the upper bound temperature of the *ITM* (*i.e. 1173 K*).

2.3 Premixed Oxy-combustion

The application of oxy-combustion technology for a gas turbine is associated with a set of constraints. Since the technology requires pure oxygen, which is obtained at the expense of extra energy, it is preferred based on economics to keep the operating equivalence ratio near unity i.e. stoichiometric combustion. Also, replacement of N_2 by CO_2 as a diluent within the combustor affects significantly the behavior and operability ranges of the generated flames because of the differences in chemical kinetics and thermo-physical and radiative properties [10-13]. This may result in tight operability limits of the generated premixed oxy-flames when compared to air flames due to the slower kinetics and generated flame instabilities [11]. The characteristics of premixed oxy-combustion flames have been examined extensively as per the open literature. We are to analyze briefly the most relevant ones to the present investigation.

2.3.1 Effect on the Reaction Rate and Flame Speed

Mazas et al. [43] conducted experimental and numerical analysis on the laminar flame velocity of oxygen-enhanced pre-mixed combustion of methane. They measured the flame velocity using the conical flame method and the calculations were carried out using detailed kinetic mechanism *GRI mech. 3.0*. The study was conducted at varying equivalence ratio from *0.6* to *1.5* with molar oxygen-enrichment ratio [$O_2/(O_2+N_2)$] from *0.21* to *0.5* and the effect of adding water vapor with molar fraction varying from *0* to *4.5* was analyzed. The results indicate that the laminar flame velocity decreases linearly with the water vapor fraction and is independent of the equivalence ratio for a given enrichment ratio. They concluded that the effect of the addition of water vapor on the laminar flame velocity is mainly thermodynamical one and does not affect the reaction kinetics. A numerical study on the combustion characteristics of premixed oxy-combustion of methane with various flue gas addition was carried out by Li et al. [44]. It was found that the laminar burning velocity in CO_2-dilution is restrained as compared to N_2-dilution. The flame burning velocity in CO_2-dilution was found to be close that of the air/methane stoichiometric combustion at the diluent/oxygen ratio of 200%. The adiabatic flame temperature calculation shows that at lower diluent/oxygen ratio the flame temperature difference between various inert diluents (N_2/H_2O/flue gas/CO_2) is small and the difference increases with increasing dilution ratios.

Amato et al. [18] performed an experimental and numerical investigation on premixed oxy-combustion of methane and compared it with methane-air combustion. They observed blow off in the carbon dioxide environment at a flame temperature of $300\ K$ above that of in the air combustion, at a given nozzle exit velocity. The reason was found to be slower reaction kinetics in CO_2 environment due to the kinetic inhibiting effect of CO_2. The effect of oxygen fraction in N_2 and CO_2 dilution on the premixed swirling flame in a gas turbine system is studied by Marsh et al. [45]. Their results indicate that the effect of the dilution ratio on the flame location, heat released, and the operational response is far more significant in the CO_2 diluent system than in N_2 under lean operating conditions. The observation was related to the fact that the two gases have different thermodynamic and transport properties. They also found that the formation of CO increased with increasing CO_2 fraction in the CO_2 diluent system, while NO_x emission increased with N_2 dilution. Srodowiska and Jerzak [46] conducted experimental and numerical investigations on the formation of carbon monoxide in premixed oxy-combustion of natural gas. The experiments were conducted with 5% excess oxygen and the oxygen fraction was varied from 23% to 29%. Their results indicate that increasing the oxygen fraction in the oxidizer stream increases the peak CO molar fraction near to the burner but decreases at a larger distance from the burner. The overall rate of formation of CO reduces and higher H radicals are formed with increasing oxygen fraction.

To enhance the combustibility of premixed oxy-combustion of methane, Osaka et al. [47] experimentally studied the effect of power coupling between the oxy-combustion and radio frequency (*RF*) power using the induction coil. They found that the flame can absorb *RF* power up to 1.5 kW with increased *OH* radicals in the flame and improved combustibility. Taamallah et al. [48] conducted an experimental investigation on the effect of diluent on the flame transition to the outside recirculation zone (*ORZ*) in lean premixed swirl combustor. Their findings show that the transition depends on the extinction strain rate and is independent of adiabatic flame temperature and unstretched laminar burning velocity at similar bulk flow conditions in *ORZ*. They also came up with a correlation between the inverse of the *ORZ* spinning frequency and the inverse of extinction strain rate valid for both air and oxy-combustion. Shroll et al. [49] studied the dynamic behavior of the premixed oxy-combustion flame of methane in a swirl-stabilized reactor. Flame structures in air and O_2/CO_2 environment were found to be similar in all the modes. Also, for $CH_4/O_2/CO_2$ flames, the transition from one mode to another is largely dependent on adiabatic flame temperature as in the case of CH_4/air flames, despite the laminar burning velocities and strained flame consumption speed being different.

2.3.2 Effect on the Static Stability

A detailed comparison of methane premixed flames in a swirl combustor in N_2 and CO_2 environment was carried out by Jourdaine et al. [50]. It was found that the CO_2 diluted flames are less stable than N_2 diluted flames for the investigated range of operation with the injection Reynolds number less than *20,000*. They found that the transition regimes of different shapes of the flame for CO_2-diluted flames and N_2-diluted flames almost appeared at the same swirl numbers. CO_2-diluted flames were found to be unstable for $U_b/S_L < 34$ (ratio of injection bulk velocity to laminar burning velocity), however, N_2-diluted could be stabilized for this range too. This confirms the fact that the flame stability reduces in CO_2 environment as compared to air. In another study, Jourdaine et al. [51] investigated the stabilization of premixed oxy-methane and methane-air flames in a swirl reactor. They found that the oxy-methane and methane-air flames have a very similar structure at the same equivalence ratio, given that adiabatic flame temperature and U_b/S_L are kept the same. Burnt gases temperature in *ORZ* was found to be different for CO_2 and N_2 diluent system having the same adiabatic flame temperature, however, the burnt gases' and the combustor sidewalls' temperature, as well as the stabilization of the flames near the burner outlet, were not affected. They concluded that with the suggested similarity, the stabilization and flame shapes of premixed swirling oxy-methane flame can be achieved similar to methane-air flame.

2.4 Hydrogen Enriched Combustion

An alternative method to reduce CO_2 emissions in the environment is through utilizing low carbon fuels for the power generation industry. CH_4 is characterized to be the hydrocarbon fuel that contains the least amount of carbon. Nevertheless, the unique tetrahedral molecular structure in methane demonstrates low flame propagation and high ignition temperature, leading to low burning velocity and poor ability to burn at lean conditions [52]. To tackle this problem, a fuel that has a higher burning velocity has to be mixed with natural gas. Fuel flexibility approach, mainly through hydrogen enrichment, is considered as an effective technique to control combustion instabilities within gas turbine combustors to avoid flashback, auto ignition and combustion dynamics [53–55]. Hydrogen-enriched premixed oxy-flame stability and characteristics are vital for the proper application of this technology in new or existing power plants, which is the subject of the present study. Hydrogen is an excellent additive to natural gas as it results in reduced NO_x exhaust emissions, favorable flame temperatures and extended lean flammability limits [56]. Due to its intrinsic advantages, hydrogen is regarded as a future energy carrier simply by introducing it to natural gases in internal combustion engines and gas turbines. Use of hydrogen blends and syngas in combined cycle power generation is attracting interests of the research community as an alternative to natural gas. Hydrogen enriched fuels are regarded as the prominent alternative fuels for the future energy mix [57–59]. Recycling of industrial hydrogen by-product and pre-combustion carbon removal from the fuel as a carbon capturing technique can be integrated with gas turbine combined cycle plants. It has been reported that the addition of hydrogen to hydrocarbon can reduce the soot formation and CO emissions drastically [60–64]. It has also been observed to increase the laminar flame speed and lean flammability limits of the enriched flames [65–69]. Moreover, the addition of even a small amount of hydrogen in the fuel mixture can have an impact on both the instantaneous and average characteristics of a turbulent premixed flame [70], necessitating rigorous research on the combustion dynamics of such flames with varied fuel compositions.

2.4.1 Effect on the Reaction Rate and Flame Speed

Addition of hydrogen to the fuel mixture enhances the reaction rate, which is due to the increased H, O and OH radical mole fractions in the flame as reported by Hu et al. [71].

They also concluded that the higher burning velocities are also characterized by the high radical formation in the reaction zone. Similar observations were reported by Wang et al. [52] from their numerical analysis on the effect of hydrogen addition on methane/air combustion using *GRI-Mech 3.0* mechanism. Moreover, they suggested that the addition of hydrogen reduces the formation of CH_2O and CH_3CHO, consequently reducing the aldehyde emissions in methane combustion. An increase of around *20% OH* mole fraction with the blending *20%* hydrogen with methane was reported by Schefer [72]. Due to the high combustibility of hydrogen, flames with higher hydrogen fractions are characterized by higher reaction zone temperature, although the adiabatic flame temperature of the fuel blend decreases with the hydrogen addition. Due to the higher temperature, the reaction zone expands faster, consequently inhibiting the cooler recirculation flow to the reaction zone [56].

Gersen et al. [73] investigated the ignition delay time of hydrogen/methane mixture at various composition in the rapid compression machine. They found that the ignition delay time decreases with the addition of hydrogen percentage in the mixture and can be correlated quantitively to the mole fraction of hydrogen in the fuel in accordance with the mixing law proposed by Cheng and Oppenheim [74]. Kim et al. [56] studied the effect of H_2 enrichment on methane-air premixed swirling flames. They concluded that the temperature in the reaction zone is increased while the recirculation flow is reduced due to higher combustibility of H_2 which makes the reaction faster. In addition, the effect of hydrogen enrichment of methane fuel is less than the effect of swirling in the upstream of the flame region. They also reported that NO_x emissions are reduced with the increase of H_2 concentration in the fuel.

For the better understanding of the effects of hydrogen addition to natural gas in the combustion processes, a thorough understanding of the laminar burning velocity is required since it is the essential parameter in combustion processes and an important factor for turbulent burning velocity determination. Also, it is of high importance in the optimization and design analysis of power plants combustors and internal combustion engines. Consequently, extensive research has been conducted about the laminar burning velocity of H_2-enriched methane-air premixed flames over at various equivalence ratios [15–20]. The results show that the increase of H_2 percentage in the fuel mixture causes an increase in the flame speed and the laminar burning velocity.

The laminar burning velocities tend to increase linearly with the addition of hydrogen in the fuel blends [71,81]. The unstretched flame propagation speed and the unstretched laminar burning velocity were reported to increase with the addition of hydrogen in the fuel blend in a study conducted by Tang et al. [82]. They also found that this dependence gets even more remarkable at higher hydrogen fraction. Sankaran And Im [83] concluded that the high laminar burning velocity of H_2 is essentially because of higher molecular diffusivity of H_2 and the enhancement of H, O and OH radicals formation in hydrogen-rich flames. Further, in the lean mixture, the addition of hydrogen to a hydrocarbon has been found to increase the turbulent burning velocity monotonically [84]. In the rich mixture, however, hydrogen addition had no apparent effect on the burning velocity but was reported to be dependent on the type hydrocarbon. A similar dependence of turbulent burning velocity on hydrogen fraction was reported by Halter et al. [70] in their investigation on hydrogen addition in premixed methane/air flames. They further concluded that the combustion intensity S_T/S_L increases with hydrogen addition, implying that the turbulent burning velocity increases faster than the laminar burning velocity with hydrogen addition. This was attributed to the fact that with the hydrogen addition, flame front curvature distribution tends to enlarge slightly implying a higher probability of larger curvatures. This enhances the smaller scale flame wrinkling resulting in higher turbulent burning velocity. Similar findings were reported by Daniele et al. [85,86].

2.4.2 Effect on the Static Stability

Schefer [72] conducted an experimental study on the flame stability with hydrogen addition. He found that the lean blowout limit (*LBO*) is maximum at the stoichiometric condition and reduces for both the lean and rich conditions. Moreover, he reported that by the addition of up to *20%* hydrogen in the fuel mixture, the lean blowout limit could be reduced by around *15%*. A laboratory scale investigation on low swirl injector (*LSI*) was conducted by Cheng and Littlejohn [87] to study the combustion characteristics of pure hydrogen and H_2-N_2 dilution with air with the aim to implement it in the gas turbines of the integrated gasification combined cycle (*IGCC*). They found an optimum swirl number *0.51* for H_2 in the investigated various *LSI* configurations as compared to *0.54* for the hydrocarbon *LSI*. The *LBO* limit was found to occur at almost a constant equivalence ratio of *0.17* at varying bulk velocities, indicating that the *LBO* of *LSI* hardly depends on the Reynolds number. Another parameter which has been found to be fairly successful in predicting the *LBO* limit is Damkohler number. Zhang et al. reported an interesting finding that the *LBO* was observed to occur at a Damkohler number of *0.4* with various compositions of $H_2/CO/CH_4$ fuel blends.

Ghoniem et al. [88] investigated stability and emission control of hydrogen enrichment in premixed combustion and they concluded that hydrogen addition widens the flame extinction limits by feeding more air to the primary stream, thus reducing NO_x. Chen and Zheng [89] investigated oxy-fuel characteristics of H_2-enriched biogas diffusion flames. They reported that oxy-fuel diffusion flames can be stabilized with a small hydrogen addition to the fuel mixture and highly diluted O_2 concentration at a relatively low preheating temperature in the oxidizer flow. Riahi et al. [90] experimentally studied non-premixed flames characteristics at stoichiometric conditions enriched by hydrogen (varying from *0* to *15%*) and oxygen (varying from *20* to *50%*). They concluded that the addition of hydrogen and oxygen enhances the flame stability and eliminates lifted flames. Sanusi et al. [91] conducted an experimental study on oxy-combustion of non-premixed hydrogen-enriched methane flames that contains CO_2 diluents. Hydrogen contents were varied from *0* to *20%* in CH_4/H_2 fuel mixtures. The results agreed with the previously reported findings by Ghoniem et al. [88] that the addition of hydrogen extends the stability limits of the oxy-combustion flames.

2.5 Permeation Through ITM

Ion transport membranes (*ITMs*) are made from ionic and mixed conducting ceramic oxide which selectively conducts oxygen ions at elevated temperatures. *ITMs* show great potentials to be integrated with oxy-combustion technology where it can be used to separate oxygen from air, either in non-reacting sweep gas configuration or reaction driven oxygen separation. Several studies have been conducted to model the oxygen permeation through the membrane as a function of temperature, oxygen partial pressure, reaction rates etc.

Literature shows a wide range of mathematical correlations which can be grouped into two major categories: (i) *1-D* model, (ii) Point defect model and (iii) Detailed model.

2.5.1 *1-D* Model

Qui et al. [92] conducted experimental studies on the oxygen permeation through $SrCo_{0.80}Fe_{0.20}O_{3-\delta}$ over a temperature range of 620 – 920 °C. *1-D* model given by Wagner equation was used to give the permeation flux due to bulk oxygen ion transport:

$$J_{O_2} = \frac{RT}{4^2 F^2 L} \bar{\sigma}_i \ln \frac{p_{O_2}^{'}}{p_{O_2}^{''}} \qquad (11)$$

The permeation rate was calculated for different oxygen partial pressure on the oxygen-rich side and membrane thickness. They found an apparent activation energy of *22 kcal/mol* for the overall permeation rate at temperatures below *770 °C*. The results indicate that the permeation flux is highly dependent on the temperature, however, shows little dependence on the disc thickness. They concluded that the surface exchange reaction is the rate-limiting step in the overall permeation.

Qi et al. [93] prepared *LSCF* membranes with four different methods having different compositions. It was found that the activation energy for the oxygen flux decreases with the grain size. They assumed bulk diffusion as the rate-limiting approach and the simplified oxygen permeation equation was given as:

$$J_{O_2} = \frac{RT\sigma_i^o}{8F^2L}\left(P_{O_2}^{''\,-n} - P_{O_2}^{'\,-n}\right) \qquad (12)$$

where, $P_{O_2}^{'\,-n}$ and $P_{O_2}^{''\,-n}$ are the oxygen partial pressures at the feed side and permeate side respectively, F is Faraday's constant, L is the membrane thickness, σ_i^o is the oxygen ion conductivity at oxygen partial pressure of *1 atm* and *T* is the temperature. The obtained oxygen permeation flux data was regressed to the Arrhenius equation and the pre-exponential constant and the activation energy for different materials were calculated.

$$J_{O_2} = K^o \exp(E / RT) \qquad (13)$$

The parameters are tabulated as below:

Table 1. Parameters for the *1-D* model

	Methods			
	CA	*SS*	*SP*	*CP*
Activation energy *E* (*kJ/mol*)	*90.7*	*92.7*	*127.8*	*81.9*
Pre-exponential constant K^o (*mol/cm*^{2}*.s*)	4.85×10^{-4}	7.91×10^{-4}	3.7×10^{-2}	2.81×10^{-5}

2.5.2 Point Defect Model

Hassel et al. [94] performed an analysis of oxygen permeation through $La_{0.75}Ca_{0.25}CrO_{3-\delta}$ perovskite using point defect model. The nonstoichiometry is a function of the oxygen partial pressure and hence, the oxygen permeation current density was calculated using:

$$J_{O^{2-}} = \frac{2FD_V}{LV_m} \times \left[y\ln\left(y-2\delta\right) + 3\ln\left(3-\delta\right) + \left(1-y\right)\ln\left(1-y+2\delta\right) \right] \tag{14}$$

where, F is Faraday constant, D_v is the vacancy diffusion coefficient, L is the membrane thickness, V_m is the molar volume of the perovskite, y is the mole fraction *Ca* and δ is the nonstoichiometry. The oxygen permeation model parameters values are:

$$T = 1273K; \quad L = 1\times10^{-3}m; \quad y = 0.25;$$
$$V_m = 3.4\times10^{-5}m^3mol^{-}1; \quad D_V = 10^{-9}m^2s^{-1}$$

They concluded that the oxygen permeation depends primarily on the oxygen partial pressure at the low oxygen partial pressure side at when the nonstoichiometry of the perovskite is small.

Oxygen nonstoichiometry of two *LSCF* ceramics, namely $La_{0.1}Sr_{0.9}Co_{0.9}Fe_{0.5}O_{3-\delta}$ (*LSCF-1*) and $La_{0.1}Sr_{0.9}Co_{0.9}Fe_{0.1}O_{3-\delta}$ (*LSCF-2*) was determined experimentally by Yang and Lin [95]. They correlated. Several experiments were conducted at various temperatures and oxygen partial pressures and a semi-empirical equation using point defect model for oxygen permeation current density was presented.

$$J_{O^{2-}} = \frac{3FD_V}{LV_m n} \ln\left(\frac{1+KP_{O_2}^{'n}}{1+KP_{O_2}^{''n}} \right) \qquad (15)$$

where L is the membrane thickness, V_m is the molar volume of the perovskite-type ceramics and $K \text{ and } n$ are the constants dependent only on the temperature. The constants were given as a function of temperature and the correlations were established by regressing the experimental results:

$$K = C_1 e^{-\frac{C_2}{T}} \qquad (16)$$

$$n = C_3 + C_4 T \qquad (17)$$

The regression constants for various type of perovskite membranes are presented below:

Table 2. Parameters for point defect model

	$K\left(atm^{-n}\right)$		n	
	$C_1\left(atm^{-n}\right)$	$C_2\left(K\right)$	C_3	$C_4\left(K^{-1}\right)$
LSCF-1	*0.4087*	*1007.6*	1.205×10^{-4}	*-0.1335*
LSCF-2	*0.4656*	*1255.0*	1.104×10^{-4}	*-0.1523*
$SrCo_{0.8}Fe_{0.2}O_{3-\delta}$	*0.3177*	*703.8*	1.7×10^{-5}	*-0.06048*
$La_{0.3}Sr_{0.7}CoO_{3-\delta}$	*0.816*	*2621.8*	2.005×10^{-4}	*-0.2685*
$SrCe_{0.8}Fe_{0.2}O_{3-\delta}$	*0.1071*	*484.5*	3.7×10^{-5}	*-0.06338*

2.5.3 Detailed Model

An experimental investigation was conducted by Xu and Thomson [96] to the study the oxygen permeation characteristics through $La_{0.6}Sr_{0.4}Co_{0.2}Fe_{0.8}O_{3-\delta}$ (*LSCF*) membrane. They developed a mathematical model to predict the oxygen permeation through membranes with high electronic to ionic conductivity ratio. Oxygen flux can be given in the terms of oxygen partial pressures across the membrane as:

$$J_{O_2} = \frac{D_V k_r (P_{O_2}^{'0.5} - P_{O_2}^{''0.5})}{2Lk_f (P_{O_2}^{'} P_{O_2}^{''})^{0.5} + D_V (P_{O_2}^{'0.5} + P_{O_2}^{''0.5})} \qquad (18)$$

where the oxygen vacancy bulk diffusion coefficient (D_V)is given as:

$$D_V = D_V^o \exp\left(-\frac{E_D}{RT}\right);\ with\ D_V^o = 1.58\times10^{-2} cm^2/s\ and\ E_D = 73.6\, kJ/mol$$

forward surface exchange rate constant is given as:

$$k_f = k_f^o \exp\left(-\frac{E_f}{RT}\right)\ with\ k_f^o = 5.90\times10^6 cm/atm^{0.5}\cdot s\ \ and\ E_f = 226.9\, kJ/mol$$

and reverse surface exchange rate constant is given as:

$$k_r = k_r^o \exp\left(-\frac{E_r}{RT}\right);\ k_r^o = 2.07\times10^4 mol/cm^2\cdot s;\ E_r = 241.3\, kJ/mol$$

They affirmed that the rate-limiting step at low temperatures (around *760 ^oC*) for the oxygen permeation through the membranes is the surface exchange reaction at the low oxygen partial side. However, at higher temperatures (around *950 ^oC*) the permeation flux is dominantly governed by the bulk diffusion. After conducting a series of experiments at different temperatures and with different disk thickness, they concluded that the model is applicable to perovskite-type membranes with high electronic to ion conductivity ratio at different permeation conditions.

Wang et al. [97] prepared $Ba_{0.5}Sr_{0.5}Co_{0.8}Fe_{0.2}O_{3-\delta}$ membrane by plastic extrusion method and performed experimental investigations on the oxygen flux in the temperature range of *700* to *900 °C*. The results indicated that the oxygen permeation is governed by bulk diffusion rather than the surface exchange reaction and the oxygen flux can be given by:

$$J_{O_2} = \frac{\pi L C_i D_a}{2S \ln\left(r_1 / r_2\right)} \ln\left(\frac{P_{O_2}^{'}}{P_{O_2}^{''}} \right) \tag{19}$$

where, L is the length of the membrane tube, r_1 and r_2 are the outer and inner radius of the tube, S is the surface area of the tube, C_i (mol/cm^3) is the density of the oxygen ion, D_a is the ambipolar ion-electron hole diffusion coefficient, $P_{O_2}^{'}$ is the oxygen partial pressure on the feed side and $P_{O_2}^{''}$ is the oxygen partial pressure on the permeate side. Ambipolar oxygen ion-electron hole diffusion coefficient (D_a) and the vacancy diffusion coefficient ($D_v = D_a\left(3-\delta\right)/\delta$) at different temperatures are given in to explain the diffusion of oxygen on the airside of the OTM, as:

.

Table 3. D_a and D_v for detailed model

Temperature (^oC)	*700*	*750*	*800*	*825*	*850*	*875*	*900*
$D_a\left(cm^2/s\right)\left(\times 10^{-6}\right)$	*0.77*	*1.16*	*1.68*	*1.87*	*2.34*	*2.83*	*3.31*
$D_v\left(cm^2/s\right)\left(\times 10^{-5}\right)$	*0.82*	*1.17*	*1.62*	*1.75*	*2.14*	*2.53*	*2.82*

A very detailed model for oxygen flux across a composite oxygen transport membrane was developed by van Hassel [98]. The oxygen flux was given, assuming the dusty gas model to explain the diffusion of oxygen on the airside of the OTM, as:

$$J_{O_2} = -\frac{\varepsilon}{\tau}\frac{1}{\dfrac{1}{D_{Kn,O_2}}+\dfrac{1-x_{O_2}}{D_{molO_2,N_2}}}\frac{P_{air}}{R_gT}\frac{1}{t_{pa}}\left(\frac{dx_{O_2}}{dx}\right) \tag{20}$$

where, x_{O_2} is the oxygen mole fraction, P_{air} is the airside absolute pressure, ε is the porosity, τ is the tortuosity, x is the dimensionless coordinate and t_{pa} is the thickness of the porous layer on the airside. $D_{molO_2,N_2}\left(m^2/s\right)$ is the molecular diffusion coefficient oxygen in an O_2/N_2 mixture and is given as:

$$D_{molO_2,N_2} = \frac{0.00266\times 10^5 T^{1/2}}{P_{air}\left(10^{-3}\dfrac{Mw_{O_2}Mw_{N_2}}{Mw_{O_2}+Mw_{N_2}}\right)^{1/2}\sigma_{O_2,N_2}\Omega_D} \tag{21}$$

Where, Mw_{N_2} is the molar weight of nitrogen, Mw_{O_2} is the molar weight of oxygen, $\sigma_{O_2,N_2}\left(\overset{\circ}{A}\right)$ is the characteristic length and Ω_D is the diffusion-collision integral. D_{Kn,O_2} is the Knudsen diffusion coefficient and is given by:

$$D_{Kn,O_2} = \frac{2}{3} r \sqrt{\frac{8R_g T}{\pi M_{O_2}}} \qquad (22)$$

where, R_g is the molar gas constant, T is the absolute temperature, r is the pore radius and M_{O_2} is the oxygen molecular weight.

Liu and Galavas [99] prepared a $Ba_{0.5}Sr_{0.5}Co_{0.8}Fe_{0.2}O_{3-\delta}$ ($BSCFO$) hollow tubular membrane and conducted a series of experiments varying different parameters. He proposed that the oxygen permeation flux can be given by:

$$J_{O_2} = Ak(T)G\left[\left(P_{O_2}^{'}\right)^n - \left(P_{O_2}^{''}\right)^n\right],\ n<1 \qquad (23)$$

where $k(T)$ is a temperature factor and G is the geometric factor. However, they did not try to regress the data to this model with the presumption that the surface exchange reaction may also affect the permeation rate. Tan et al. [100] performed an experimental study to measure the oxygen permeation flux in a hollow fiber membrane reactor using *LSCF* membrane with methane oxidative coupling reaction. The oxygen permeation flux was calculated using the equation:

$$F_{O_2} = \frac{0.79 F_{Air} x'_{O_2}}{1 - x'_{O_2}} \tag{24}$$

where F_{Air} is the air feed flow rate and x'_{O_2} is the outlet molar fraction of oxygen in the air stream.

A compromise between a highly detailed model and a black-box model to predict the oxygen flux through an ion transport membrane was considered by Mancini and Mitsos [33]. They developed a quasi-two-dimensional model using fundamental conservation equations, semi-empirical oxygen transport equations, and simplified fuel oxidation kinetic reaction. The oxygen flux was given as a function of the membrane temperature, the feed and permeate oxygen partial pressures and empirical constants depending on the material type:

$$J_{O_2} = A \exp(-B / T_M) \left[\left(P'_{O_2} \right)^n - \left(P''_{O_2} \right)^n \right] \tag{25}$$

where, the constant A takes account of the diffusion coefficient and the membrane thickness, B is the effective activation energy taking into the consideration of both diffusion coefficient and surface exchange kinetics. The curve fits for *LNO* and *LSCF* membrane are listed below:

Table 4. Curve fits for *LNO* and *LSCF* membranes

Membrane type	n	$A\left[mol\, m^{-2} s^{-1} pa^{-n}\right]$	$B\left[K\right]$	Temperature range (*K*)	*O₂* partial pressure range (*Bar*)
LSCF	*0.5*	*26.75*	*16,510*	*1023-1233*	*6×10^{-3} - 1*

LNO	*0.25*	*2.011*		*10,240*	*1123-1273*	*8×10^{-4} – 2.1*

Behrouzifar et al. [101] synthesized a *BSCF* membrane by a sintering process and performed experimental studies on the oxygen permeation flux at various temperature, feed and permeate side oxygen partial pressure, flow rates and membrane thickness. They developed a mathematical model based on the Nernst-Planck equation, to predict the oxygen flux across the membrane. The model was capable of considering the surface exchange kinetics and bulk diffusion and can be given as:

$$J_{O_2} = \frac{\left(k_r / k_f\right)\left[\left(1/ p''^{*\,n}_{O_2}\right)\right] - \left(1/ p'^{*\,n}_{O_2}\right)}{\left[1/\left(k_f\, p'^{*\,n}_{O_2}\right)\right] + \left[2L / D_V\right] + \left[1/\left(k_f\, p''^{*\,n}_{O_2}\right)\right]} \qquad (26)$$

where the oxygen vacancy diffusion coefficient D_V and surface exchange forward and backward reaction constants k_f and k_r were given in terms of Arrhenius equation as:

$$D_V = D_V^o \exp\left(-\frac{E_D}{RT}\right) \qquad (27)$$

$$k_f = k_f^o \exp\left(-\frac{E_f}{RT}\right) \qquad (28)$$

$$k_r = k_r^o \exp\left(-\frac{E_r}{RT}\right) \qquad (29)$$

The equation uses modified feed and permeate side partial pressures $p'^{*}_{O_2}$ and $p''^{*}_{O_2}$, which takes into account the effect of feed and sweep gas flow rates on the oxygen flux and can be given as:

$$p'^{*}_{O_2} = \left(a' + b'\,\mathrm{Re}'^{c'}\right) p'_{O_2} \tag{30}$$

$$p''^{*}_{O_2} = \left(a'' + b''\,\mathrm{Re}''^{c''}\right) p''_{O_2} \tag{31}$$

where all the parameters were evaluated by regressing the experimental data and are summarized below:

Table 5. Parameters for detailed model

Parameter	Value	Dimension
D_V^o	*5.9807 × 10^{-5}*	*m^2/s*
k_f^o	*4.1688 × 10*	*m/atm^n s*
k_r^o	*1.1660 × 10^4*	*mol/m^2 s*
E_D	*9.2709 × 10^4*	*J/mol*
E_f	*1.4668 × 10^5*	*J/mol*
E_r	*1.0291 × 10^5*	*J/mol*
n	*0.2500*	-
a'	*0.1015*	-
b'	*1.8687*	-
c'	*0.4525*	-
a''	*0.1891*	-

b"	*9.3439*	-
c"	*0.1320*	-

CHAPTER 3

PROBLEM STATEMENT AND METHODOLOGY

3.1 Problem Statement

Present work can be categorized into three main sub-headings. In the first part, a carbon-free oxy-combustion based power generation system is proposed and a detailed thermodynamic analysis of the system is carried out. The second part focusses on the experimental investigations of oxy-combustion in a pre-mixed vertical reactor. And in the third part, a computational fluid dynamics (*CFD*) analysis of the premixed reactor gas turbine reactor is conducted.

3.1.1 Thermodynamic Analysis of Carbon-free Power Generation System

This work proposes two novel power systems incorporated with carbon capture via oxy-combustion. The first system is based on premixed oxy-combustion cycle where oxygen is separated from the air and mixed with the fuel, before it is fed into the combustion chamber, using an ITM-ASU. The second system utilizes an ITM integrated reactor, where oxygen separation and oxy-combustion process occurs simultaneously at the feed-side and permeate-side of the membrane, respectively. The thermodynamic analysis of the power generation system and air separation unit is conducted. The exergy destruction in various components of the power generation system is investigated and different cycle designs are studied in an attempt to improve the overall efficiency of the proposed plants.

3.1.1.1 Non-premixed combustion-based system

A carbon-free oxy-combustion based power generation system is proposed and the schematic diagram is shown in Figure 7. The basic energy inputs of the system are methane and solar radiation. Methane is fed into a solar reformer where it reacts with steam to form syngas. Syngas, which is basically carbon monoxide and hydrogen, is fed into an ITM integrated reactor, where the fuel is burned in oxygen plus carbon dioxide environment. The hot flue gas is fed into a turbine to convert the chemical energy into mechanical energy, which is used to drive a generator to produce electricity. The exhaust from the turbine, which constitutes carbon dioxide and water vapor, is passed through a condenser to separate CO_2 from H_2O. Then a part of the separated CO_2 is recirculated into the oxy-fuel reactor and the rest is fed to the other side of the *ITM* the reactor, where splitting of CO_2 takes place. CO_2 splits into carbon monoxide and oxygen in an endothermic reaction. Due to induced oxygen partial pressure across the *ITM* reactor, O_2 permeates to the combustion side of the reactor where it reacts with the syngas in the oxy-combustion process. Similarly, H_2O is fed to one side of the *ITM* reactor, where steam splits into H_2 and O_2 components and again the permeation of O_2 to the combustion side of the reactor takes place. The by-products of the splitters, hydrogen and carbon monoxide, is stored and can be used as a power source for the night time.

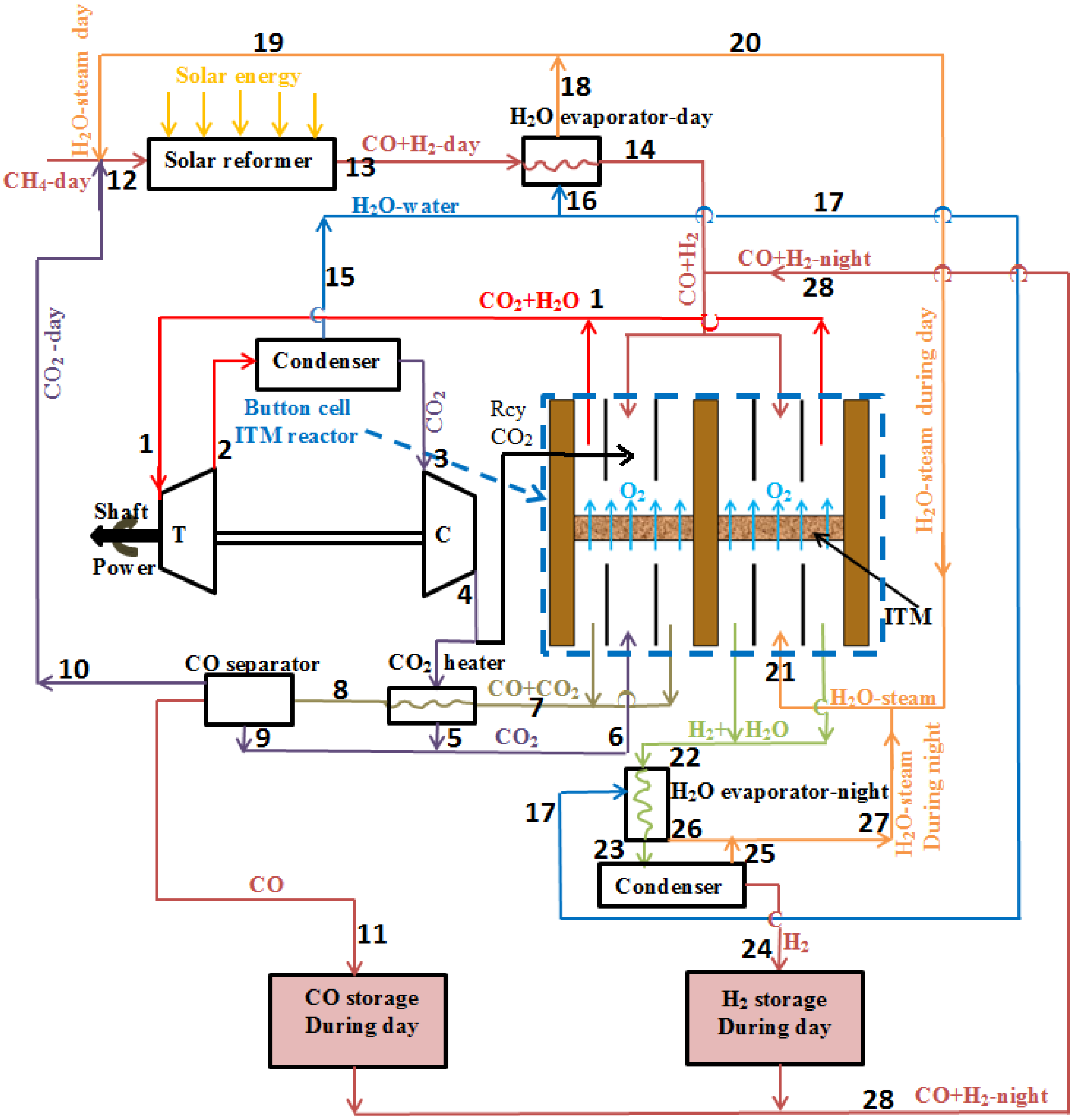

Figure 7. Schematic diagram of a carbon-free power generation system based on ITM integrated oxy-combustion reactor

3.1.1.2 Premixed combustion-based system

A premixed combustion based power generation system is proposed which utilizes an air separation unit (*ASU*) using *ITM* technology to separate oxygen from air for the oxy-combustion cycle. Atmospheric air is compressed at high pressure prior to its feeding to an *ITM* based *ASU*. The air is further heated to the operating range of the *ITMs* and a highly pure stream of oxygen is obtained from the *ASU*. The separated oxygen is fed to the combustion chamber along with methane and recycled CO_2 to obtain the hot flue gases which are used to extract power from a gas turbine. The exhaust from the turbine is condensed to separate CO_2 from water vapor. The captured CO_2 is then compressed and a part of it is recirculated to the combustion chamber while the rest is stored for sequestration.

As discussed earlier, hydrogen enrichment in the fuel blend has an inherent benefit of better combustion behavior and flame stability. Hence, the integration of hydrogen enrichment in oxy-combustion technology may be advantageous on two fronts: (a) improving the flame stability and behavior in CO_2 rich environment and (b) reducing CO_2 emission by replacing carbon rich fuels. Therefore, the study was extended to assess the effect of hydrogen enrichment on the system efficiency in terms of the first and second of thermodynamics.

3.1.2 Experimental Investigations of Hydrogen Enriched Methane Combustion

In this section, premixed oxy-combustion of hydrogen-enriched methane has been investigated. Figure 8 shows the schematic diagram of the experimental setup of the oxy-combustion reactor. As shown in the figure, four different gases namely, oxygen, carbon dioxide, hydrogen, and methane, are fed into the mixing chamber via mass flow controllers which are controlled using a computer system. The reacting mixture is then passed through a swirler followed by a convergent-divergent nozzle which ensures a gradual expansion of the gases into the combustion chamber. The flame is surrounded by a quartz glass so that the flame visualization and analysis can be conducted. The upper side of the reactor is equipped with a thermocouple to measure the axial and radial temperature profile along the reactor length. We investigated the effect of hydrogen enrichment level on stability limits as compared to the operation without hydrogen enrichment. The oxygen fraction in the oxidizer stream was kept at *30%* by volume, resembling closest to the air combustion environment [7,32-35]. The stability maps are recorded at different inlet velocities to explore the effect of flow dynamics on operability limits of the hydrogen-enriched flames. The obtained stability map at fixed inlet velocity, the function of *HF* and equivalence ratio at fixed *OF*, is compared with the obtained map at the same velocity, but the function of *OF* and equivalence ratio for pure methane, to explore the effects of oxygen and hydrogen

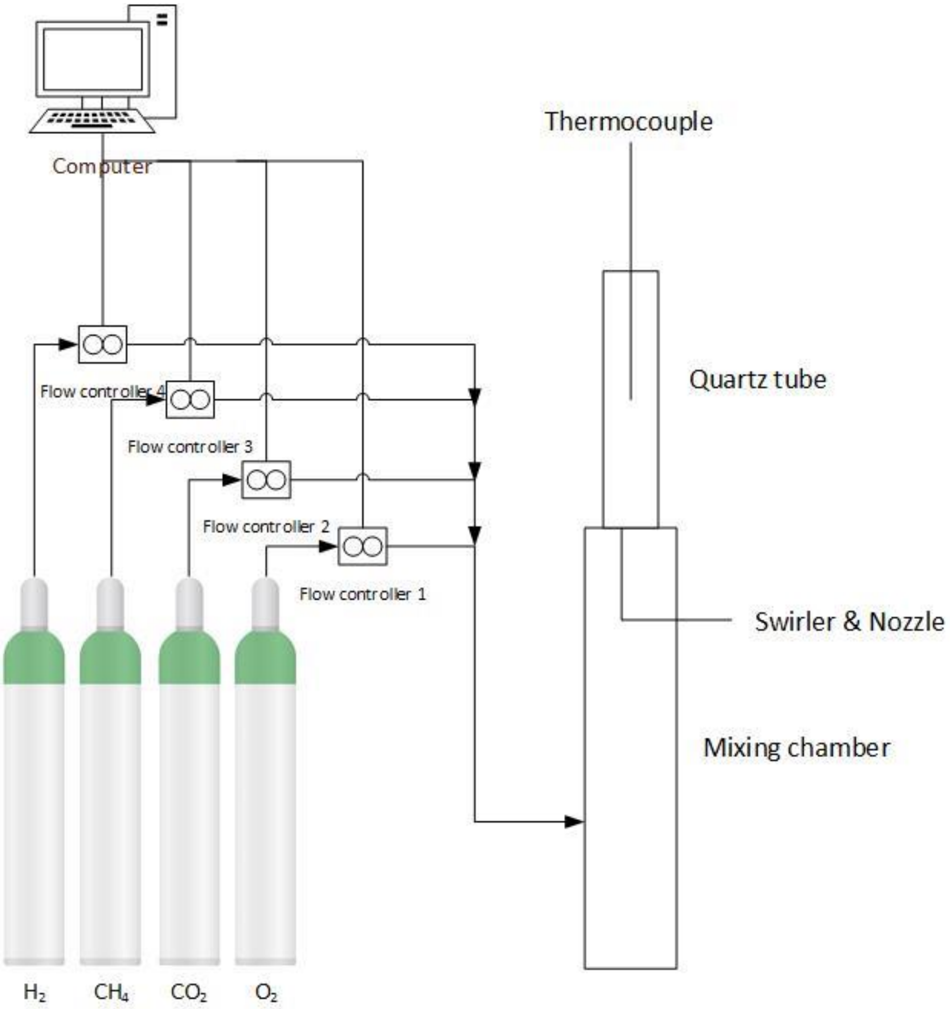

Figure 8. Schematic diagram of the experimental setup

enrichment on shifting the operability range of the generated flame. The flame shapes near flashback limit, as well as near blow-out limit, are compared to explore the mechanisms of flame extinction. Flame shapes are compared at fixed adiabatic flame temperature, fixed inlet velocity, and fixed flow swirl to isolate their effects and investigate the effect of kinetic rates. The effect of inlet flow velocity on the flame shape at a fixed adiabatic flame temperature and fixed inlet swirl is also investigated.

3.1.3 CFD Analysis of Hydrogen Enriched Methane Combustion

A computational fluid dynamics (*CFD*) model has been developed to simulate the premixed oxy-combustion of hydrogen-enriched methane in the model gas turbine combustor. The numerical model is developed on the commercial software package Ansys Fluent 19.1 and the results are validated against the experimental data. The model utilizes a partially premixed model by solving the transport equation for the mixture fraction to calculate the scalar variables. Large Eddy Simulation (*LES*) of the flow field was carried out to predict the turbulence structure in the reactor. The study contributes to the understanding of static stability and flame behavior for different hydrogen blends in the fuel stream, equivalence ratios and throat velocities in a premixed swirl-stabilized model gas turbine reactor.

3.2 Mathematical Modeling

3.2.1 Thermodynamic Analysis

Exergy can be defined as the maximum possible useful work that can be obtained from a system by bringing the system into equilibrium with the atmosphere. It can be said that the exergy measures the quantity of the qualitative energy of a system. Total exergy (Ex)is the summation of physical exergy (Ex_{ph}), kinetic exergy (Ex_{kn}), potential exergy (Ex_{pt}) and chemical exergy (Ex_{ch}).

$$Ex = Ex_{ph} + Ex_{kn} + Ex_{pt} + Ex_{ch} \tag{32}$$

Kinetic exergy and potential exergy are due to the velocity and elevation in a thermodynamic system, and hence, these are neglected in the power cycle considered in this work. Physical exergy and chemical exergy of the species are considered for the calculation of system efficiency. Physical exergy is defined as the maximum useful work that can be obtained from a process where a system at its initial temperature and pressure (*T & P*) changes its state to get into equilibrium with the environment to attain the temperature and pressure (T_o & P_o). Chemical exergy is the measure of how far the chemical composition of a system departs from the environment at normal temperature and pressure.

Environment state is defined as the state with normal temperature/pressure as well as with the same chemical composition as that of the atmosphere. Physical exergy is calculated as follows:

$$Ex_{ph} = \Delta h - T_o \Delta s = (h - h_o) - T_o (s - s_o) \tag{33}$$

Here, *h and s* represent the specific enthalpy and specific entropy of the system, respectively, and subscript '*o*' is the environmental state.

Chemical exergy of a gaseous component can be calculated as:

$$Ex_{ch,k} = -RT_o \ln x_k^o \tag{34}$$

where R is the universal gas constant and x_k^o is the mole fraction of that component in the environmental state. Generally, a system contains many different components as a mixture. The total chemical exergy of the system can be given as:

$$Ex_{ch} = \sum x_k Ex_{ch,k} + RT_o \sum x_k \ln x_k \tag{35}$$

3.2.2 Computational Fluid Dynamics

Turbulent combustion modeling is a broad subject, which involves a wide range of coupled problems like fluid properties, detailed chemical reaction scheme, two or three phase system and radiative heat transfer [102]. The turbulence model is governed by the classical Navier-Stokes, species, and energy transport equations in modified form by incorporating Reynolds and Favre averaging [102]. These partial differential equations are discretized and approximated by algebraic equations for a finite number of volumes in the domain [103].

3.2.2.1 General Conservation Equations

In the present numerical model, the mass, momentum, energy, and species transport conservation equations were numerically solved for the scalar quantities. The flow field, thermal field, and species concentration are obtained through the solution of the *3-D* elliptic conservation equations inside the reactor. All of these conservation equations including mass, momentum, energy, and species transport can be written in a general form as a function of the parameters which are the Reynolds averaged and fluctuating values of the general dependent variable as flows [19]:

$$\frac{\partial}{\partial x_j}\left(\overline{\rho}\,\overline{U}_j\Phi + \overline{\rho}\,\overline{u_j\phi}\right) = \frac{\partial}{\partial x_j}\left[\Gamma_\phi \frac{\partial \Phi}{\partial x_j}\right] + \overline{\rho} S_\Phi \tag{36}$$

Where, $\overline{\rho}$ is the density, $\overline{U}$ is the velocity component, $\overline{u_i}$ is the turbulent velocity component, Γ_Φ is the diffusion coefficient, and S_Φ is the source term. When 'Φ' equals to one, this equation represents the mass conservation equation; and when equals the velocity, it represents the momentum equation. When *‘Φ’* equals the enthalpy, this equation represents the energy equation; and finally, when equals the scalar mass fraction, this equation represents the species transport equation. The continuity and momentum equations linkage was based on SIMPLE method.

3.2.2.2 Turbulence-chemistry Interaction

The turbulence in the flow can be categorized into large eddies, typically of the scale of the characteristic length of the mean flow, and small eddies, which are responsible for the dissipation of turbulence kinetic energy. Large eddy simulation (*LES*) model was employed to solve the turbulence by filtering out the small eddies. Low-pass filtering operation for a quantity φ can be obtained using the equation [104]:

$$\overline{\varphi}(x,t)=\int G(r,x)\varphi(x-r,t)\,dr \tag{37}$$

where the integration is done over the entire domain and G is the filter function that determines the scale of the resolved eddies. Using filtering function, continuity and Navier-Stokes equations yield the following form:

$$\frac{\partial\rho}{\partial t}+\frac{\partial}{\partial x_i}\left(\rho\overline{u}_i\right)=0 \tag{38}$$

$$\frac{\partial}{\partial t}\left(\rho\overline{u}_i\right)+\frac{\partial}{\partial x_j}\left(\rho\overline{u}_i\overline{u}_j\right)=\frac{\partial}{\partial x_j}\left(\mu\frac{\partial\sigma_{ij}}{\partial x_j}\right)-\frac{\partial\overline{p}}{\partial x_i}-\frac{\partial\tau_{ij}}{\partial x_j} \tag{39}$$

where, σ_{ij} is the stress tensor due to molecular viscosity and is given by:

$$\sigma_{ij} \equiv \left[\mu\left(\frac{\partial \bar{u}_i}{\partial x_j}+\frac{\partial \bar{u}_j}{\partial x_i}\right)\right]-\frac{2}{3}\mu\frac{\partial \bar{u}_l}{\partial x_l}\delta_{ij} \tag{40}$$

and τ_{ij} is the subgrid-scale stress given by:

$$\tau_{ij} \equiv \rho\overline{u_i u_j}-\rho\bar{u}_i\bar{u}_j \tag{41}$$

The subgrid-scale stresses resulting from the filtering operation has to be modeled. Isotropic part of the subgrid-scale stress is merged with the filtered static pressure term and the deviator part is modeled using turbulent viscosity as:

$$\tau_{ij} = -2\mu_t\bar{S}_{ij} \tag{42}$$

where μ_t is the turbulent viscosity and $\bar{S}_{ij}$ is the rate of strain tensor. The turbulent viscosity was solved using Wall-Adapting Local Eddy-viscosity (*WALE*) model given by [105]:

$$\mu_t = \rho L_s^2\frac{\left(S_{ij}^d S_{ij}^d\right)^{3/2}}{\left(\bar{S}_{ij}\bar{S}_{ij}\right)^{5/2}+\left(S_{ij}^d S_{ij}^d\right)^{5/4}} \tag{43}$$

where, L_s (the mixing length for subgrid-scale) and S_{ij}^d are given by:

$$L_s = \min\left(\kappa d, C_w V^{1/3}\right)$$

$$S_{ij}^d = \frac{1}{2}\left(\bar{g}_{ij}^2\bar{g}_{ji}^2\right)-\frac{1}{3}\delta_{ij}\bar{g}_{kk}^2, \quad \bar{g}_{ij} = \frac{\partial \bar{u}_i}{\partial x_j}$$

where, κ is the von Karman constant, d is the distance to the closest wall, C_w is the *WALE* constant and V is the volume of the computational cell.

3.2.2.3 Radiation Model

Discreet Ordinate (*DO*) model is used to solve radiative heat transfer in the reactor, with 5 flow iterations per radiative iteration. The *DO* model solves the radiative transfer equation by dividing the entire solid angle into a finite number of angular spans, each associated with a vector direction $\vec{s}$ fixed in the global Cartesian system *(x,y,z)* [106].

$$\frac{dI(\vec{r},\vec{s})}{ds}+(a+\sigma_s)I(\vec{r},\vec{s})=an^2\frac{\sigma T^4}{\pi}+\frac{\sigma_s}{4\pi}\int_0^{4\pi}I(\vec{r},\vec{s}\,')\Phi(\vec{s}.\vec{s}\,')d\Omega' \qquad (44)$$

Where $\vec{r}$ is the position vector, $\vec{s}$ is the direction vector, $\vec{s}\,'$ is the scattering direction vector, s is the path length, a is the absorption coefficient, σ_s is the scattering coefficient, I is the radiation intensity, T is the local temperature, Φ is the phase function and Ω' is the solid angle. Here *'n'* is the refractive index and taken as unity. The absorption coefficient of the gas mixture is determined by the domain based Weighted sum-of-gray-gas model (*WSGGM*). The internal emissivity of all the walls is taken as 0.7.

3.3 Methodology

3.3.1 Thermodynamic Analysis of the Power Generation System

For the first law and the second law analysis of the power generation system, commercially available process simulation software Aspen Hysys is to be used. The process diagram of the proposed system is presented in Figure 7. All the components required for the system, like oxygen, carbon dioxide, carbon monoxide, hydrogen, methane, and water, are selected from the component list in the ‘Simulation Basis’. Peng Robinson fluid package was added to the basis and the reaction sets for combustion, gasification, and splitting were defined. Gasification of methane in the presence of steam is modeled in a conversion reactor. The heat required for the endothermic reaction can be obtained from a solar concentrator and has been assumed as heat input for the reactor. In another conversion reactor, oxy-combustion of syngas produced from the gasifier is simulated, where some of the carbon dioxide is recirculated from the exhaust to the combustion chamber. The amount of recirculated carbon dioxide is fixed such that the adiabatic flame temperature inside the combustion chamber is maintained at *1200 K*. As the proposed reactor is an *ITM* integrated oxy-combustion reactor, the flame temperature is deliberately selected within the working range of *ITM*. Exhaust gases are used to power a turbine where the gases expand from 10 atm pressure to *1 atm* pressure. The turbine-compressor system is fixed to deliver a net output work of *1 MW* using ‘Adjust’ command of the Hysys. A recovery heat exchanger is set at the exhaust of the compressor to further heat up carbon dioxide being fed to the CO_2-splitter. Another conversion reactor used to set up the CO_2 splitting reaction. The reactor temperature is kept at *1200 K* and a heat source is assumed. The tolerance for the convergence of output power is set to *5 kW* and temperature tolerance is fixed at *5 K*. The simulation is run until the solution is converged for *1 MW* of net output power.

3.3.2 Investigation on Hydrogen-enriched Oxy-combustion

Oxy-combustion of hydrogen-enriched flame is to be investigated in a premixed vertical reactor. The work will be divided into two parts: (*i*) experimental investigation and (*ii*) numerical simulations.

The experimental setup is presented in Figure 8. Oxygen, hydrogen, methane and carbon dioxide cylinders are used for the experiments with four mass flow meters attached to them respectively. The flow rates of each gas are controlled using a computer attached to the flow meters. The gases are fed to the mixing chamber on the reactor as shown in the figure. At the exit of the mixing chamber, a swirler is attached followed by the throat of *2 cm* diameter. The inlet velocity of the premixed gases was set to *5.2 m/s*. The hydrogen fraction in the fuel stream was varied from *0%* to *70%* and the range of equivalence ratio was considered from *0.3* to *1.0* for the proposed study. The stable flame region was analyzed by finding the blow off and the flashback limits. Effect of equivalence ratio and hydrogen fraction of flame structure is visualized in the stable region. Horizontal and vertical flame temperature is measured using thermocouple attached to a movable probe.

In the numerical part, a *CFD* code has been developed in a commercially available Fluent package to simulate the oxy-combustion of the hydrogen-enriched methane. A *3-D* axis-symmetric quadrant geometry of the reactor is considered for the numerical model and the results are validated against the experimental data. Partially premixed model is utilized to solve the mixture fraction transport equation. Radiation heat transfer is modeled using discrete ordinate (*DO*) model. The absorption coefficient of the mixture is calculated using the weighted sum of grey gas model. Large Eddy Simulation (*LES*) is used to filter out the smaller eddies and is solved using the *WALE* model.

CHAPTER 4

THERMODYNAMIC ANALYSIS OF THE OXY-COMBUSTION CYCLES

4.1 System Description

The present study considers different power generation systems and compares the results in terms of exergy destruction of all the components and first and second law efficiencies of each system. Two oxy-combustion based power generation systems, premixed and non-premixed, are evaluated. Both the systems employ *ITM* based oxygen separation units to aid the combustion in a nitrogen-free environment in a gas turbine cycle. The two oxy-combustion cases are compared with a conventional base case system based on air combustion of methane to obtain useful work through a gas turbine cycle. The overall thermal efficiencies of the systems are assessed and compared to the base case. The second law efficiency of the systems, as well as exergy destructions in the components, are calculated and the sources of maximum exergy losses are identified. Based on the obtained thermal and exergy losses, an attempt is made to minimize the losses and increase the overall efficiencies of the systems through the modification of the system design. Based on that, the additional two modified cycles, considering premixed and non-premixed conditions, are also proposed.

4.1.1 Base Case Air-combustion Cycle

A simple power generation system based on conventional combustion in a gas turbine combustor is selected as the base case for this study. The fuel used is methane which is the primary fuel used in all of the cases presented in this study. The system considered is a combined cycle gas turbine comprising of basic components to eliminate the intricacies of the thermodynamic calculations of a real gas turbine cycle. The power generation system consists of a compressor, a combustor, and a turbine with heat recuperation from the exhaust gases through a high-pressure and a low-pressure steam turbine. The heat recuperation system also consists of three heat exchangers, a condenser and a pump, configured as presented in the schematic diagram of the combined cycle power system in Figure 9. The first step is to suck the atmospheric air and compress it to high pressure to

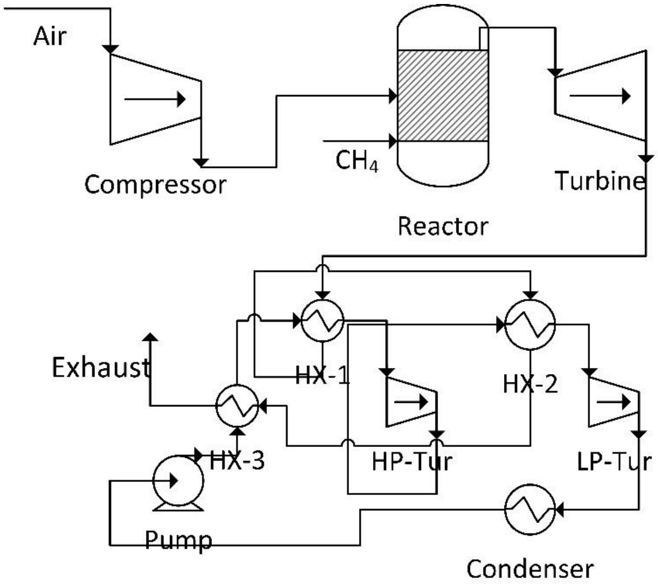

Figure 9. Schematic diagram of the base case power system

be fed to the combustor. The oxidizer and fuel are mixed and burned in the high-pressure combustion chamber of the gas turbine which delivers the running power to the rotor during expansion, and the exhaust gas from the gas turbine is fed to the steam turbine cycle for heat recuperation. The conventional air combustion base case is selected such that the proposed carbon capture systems can be compared in terms of thermodynamic efficiencies and exergy losses.

4.1.2 Oxy-combustion Cycles

Two oxy-combustion cycles are investigated under premixed and non-premixed combustion conditions. In both systems, a separation unit is used for oxygen separation either from the air in case of the premixed combustion cycle or from CO_2/H_2O in case of the non-premixed combustion cycle. The black box modeling assumption was applied to model the separation of oxygen from the air in case of a premixed oxy-combustion cycle, and from CO_2/H_2O stream in case of non-premixed integrated oxy-combustion cycle. The model ignores the actual mechanism of the separation process but rather deals with the exergy balance to the control volume of the separation unit with the unit's second law efficiency as the dominant variable of the process. The separator considered in this study is an *IT*M-based unit, which works on the oxygen partial pressure gradient across the membrane maintained at an elevated temperature in the range from *1100* to *1200 K*. The separation units produce two product streams of oxygen and waste gas from a single inlet stream. The energy stream is supplied to the unit to achieve the desired temperature and pressure suitable for efficient oxygen permeation through the membrane. A diagram of the separation unit is shown in Figure 10. The product stream is high purity oxygen as the *ITM* allows highly selective permeation. The waste stream consists of residual gases in the stream. The inlet condition of the stream is calculated from the upstream and by defining the outlet temperature, pressure and composition of the outlet stream and the thermodynamic state of the system are well defined. First law analysis requires energy balance across the control volume and can be given as:

$$m_i h_i + W + Q = m_p h_p + m_w h_w \tag{45}$$

The exergy balance equation for the separation unit is given by:

$$\begin{aligned} & m_i \left[(h_i - h_o) - T_o (s_i - s_o) \right] + W + Q \left(1 - {T_o}/{T} \right) \\ & = Ex_{des} + m_p \left[(h_p - h_o) - T_o (s_p - s_o) \right] + m_w \left[(h_w - h_o) - T_o (s_w - s_o) \right] \end{aligned} \tag{46}$$

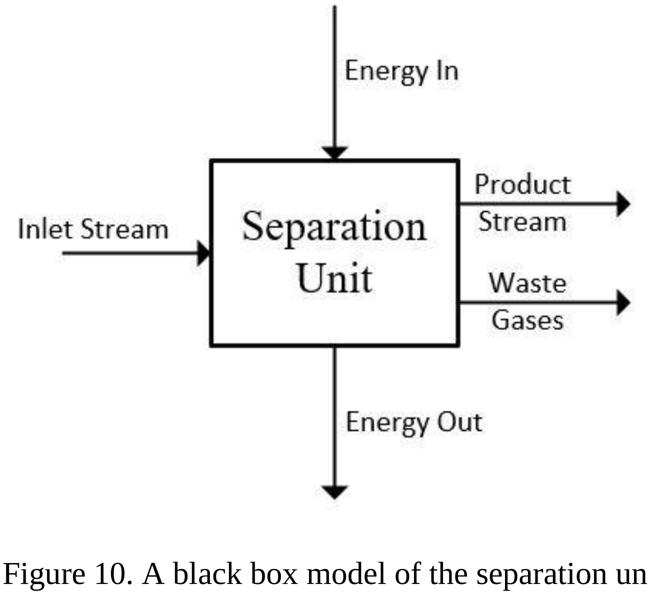

Figure 10. A black box model of the separation unit.

4.1.2.1 Premixed Oxy-combustion Cycle

The proposed cycle is based on premixed oxy-combustion of methane in a gas turbine cycle, as shown in Figure 11. An air separation unit (*ASU*) based on the oxygen permeation through an *ITM* is implemented to provide the oxygen for the oxy-combustion process. The unit comprises a compressor to supply high-pressure air to the separation chamber, where oxygen is separated through the membrane at an elevated temperature. The model assumes a heat source for the *ASU* which can be extracted from a renewable energy source, most probably solar energy. The separated pure oxygen is used directly in the combustor for the premixed oxy-combustion of methane. A portion of the exhaust CO_2 is recycled into the combustion chamber to maintain the desired temperature for the gas turbine material. The flue gas is expanded in the gas turbine to extract the useful work and then directed to a condenser. The flue gas, which is a mainly carbon dioxide and water vapor, is cooled down to condense the water vapor out, and a highly-concentrated stream of CO_2 is obtained. The captured CO_2 is further compressed and a portion of it is recirculated into the combustion

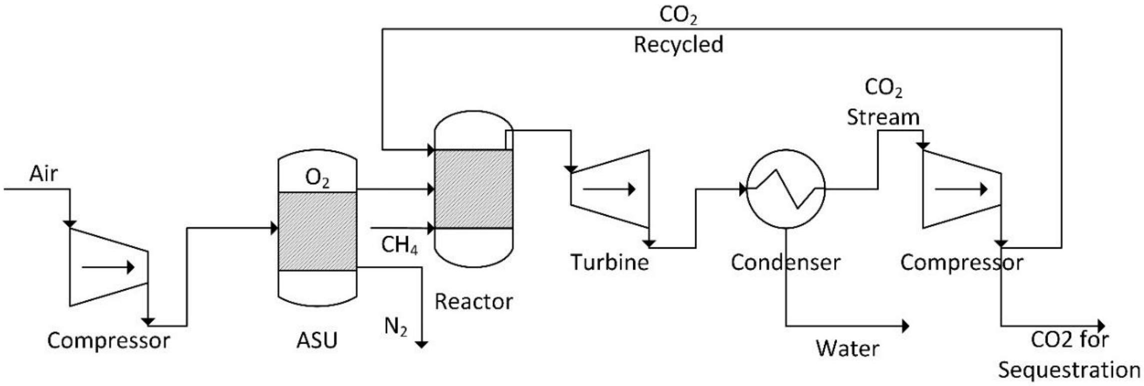

Figure 11. Schematic diagram of a single stage premixed oxy-combustion based cycle.

chamber and the rest is stored for sequestration. The first and second law efficiencies of the system can be given respectively as:

$$\eta_{th} = \frac{W_{useful}}{\left(LHV_{CH_4} + Q_{in,ASU}\right)} \tag{47}$$

$$\eta_{II} = \frac{W_{useful}}{\sum W_{rev,i}} \tag{48}$$

Where W_{useful} is the net useful work obtained from the cycle, LHV_{CH_4} is the lower heating value of the fuel stream, $Q_{in,ASU}$ is the heat required for the air separation unit, and $W_{rev,i}$ is the theoretical reversible work that can be obtained from the component '*i*' by bringing the system to the environmental dead state.

4.1.2.2 Non-premixed oxy-combustion cycle

Another oxy-combustion cycle integrated with a steam reformer and an *ITM* reactor is also proposed in the present study. The cycle diagram is presented in Figure 12. The cycle implements pre-treatment of methane in a solar reformer to obtain syngas to be utilized in the combustion chamber. As discussed earlier, the reaction kinetics are significantly diminished in an oxy-combustion flame, and several studies suggested the introduction of hydrogen in the fuel stream to overcome this issue. Syngas, which basically comprises carbon monoxide and hydrogen, has the potential to deal with this issue and, hence, has been implemented in the cycle. The syngas produced in the reformer is introduced into the combustion chamber which is integrated with an *ITM* separation unit. The idea is to create a high oxygen partial pressure gradient for higher oxygen flux due to rapid consumption of oxygen on the permeate side through combustion [33]. The exhaust gases are utilized to run the turbine to extract the useful work and, then, water is separated out via condensation to obtain CO_2 rich stream. A portion of CO_2 is recycled into the combustion chamber after being compressed and the rest is transferred to the CO_2 splitter. Similarly, condensate water is fed to the H_2O splitter. The purpose of both splitters is to provide oxygen to the *IT*M reactor for combustion while the residual gases from the splitters, which is basically concentrated CO/H_2, can be stored as an energy source when solar energy is not available for the steam reformer during the night mode of operation. Both splitters are equipped with heat exchangers for heat recuperation from the residual gases. The first law efficiency of the system can be given as:

$$\eta_{th} = \frac{W_{useful}}{\left(LHV_{CH_4} + \sum Q_{in,i} - LHV_{H_2} - LHV_{CO}\right)} \qquad (49)$$

Where W_{useful} is the net work output of the system, LHV_{CH_4} is the lower heating value of methane fed to the gasifier, $\sum Q_{in,i}$ is the heat required in the components namely gasifier, H_2O splitter, and CO_2 splitter, and LHV_{H_2} LHV_{CO} are the lower heating values of hydrogen and carbon monoxide obtained from the H_2O and CO_2 splitters, respectively. Second law efficiency of the system can be given as:

$$\eta_{II} = \frac{W_{useful}}{\sum W_{rev,i}} \qquad (50)$$

Where, W_{useful} is the net-work output of the system, and $W_{rev,i}$ is the theoretical reversible work that can be extracted from the individual components by bringing the system to the environmental dead state.

4.2 Operating Parameters

The operating parameters of all the three systems were chosen based on the operational range of the different components and were kept the same for all the cases for a fair comparison. The inlet temperature and pressure were set to the environmental dead state conditions for all the cases. For a combustor working under oxy-combustion conditions, the equivalence ratio must be maintained close to stoichiometry, as lean combustion will

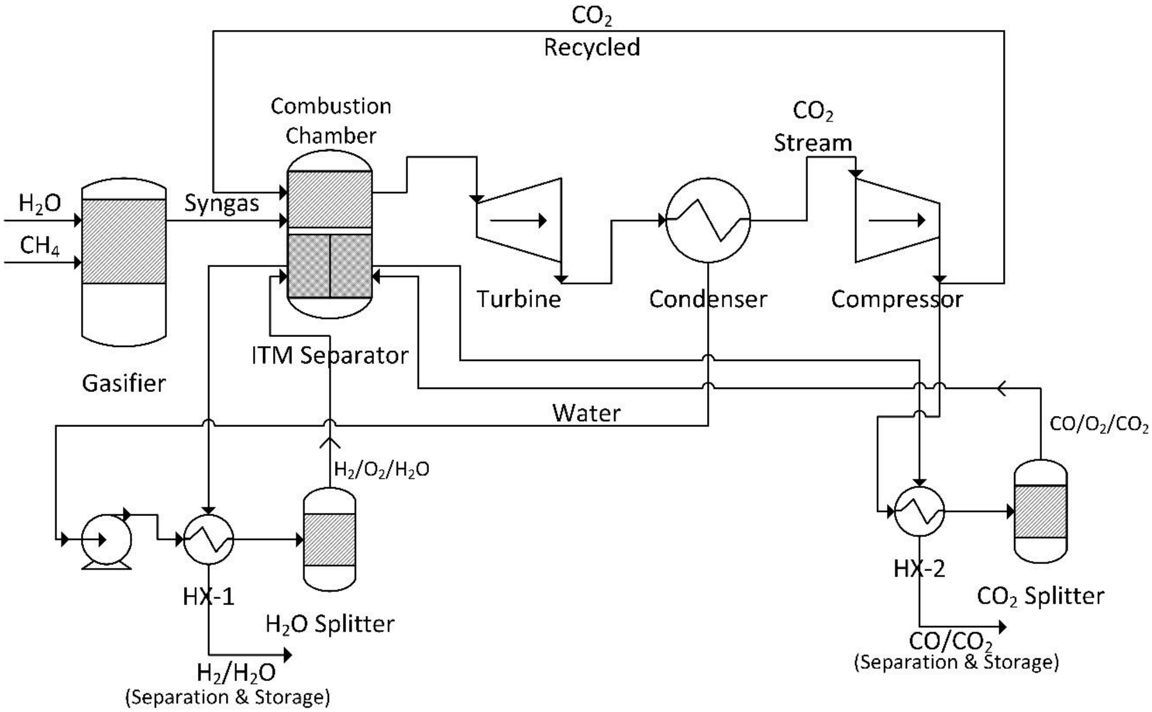

Figure 12. Schematic diagram of a single stage non-premixed oxy-combustion based cycle.

significantly affect the purpose of carbon capture as well as the energy cost associated with oxygen separation. Hence, an equivalence ratio of one (stoichiometric) was set for both the oxy-combustion cases. The operating parameters of the base case air-combustion cycle, the premixed oxy-combustion cycle and the non-premixed oxy-combustion cycle is presented in Table 6, Table 7 and Table 8, respectively.

The exhaust temperature of the reactor was set to *1200 K*, which is within the operating temperature range of a gas turbine combustor. Moreover, the non-premixed case utilizes the integrated *ITM* reactor, which needs to be operated within this temperature range too for efficient permeation. The temperature of the reactor is controlled by adjusting the recycled CO_2 flow rate into the combustion chamber. For the conventional air combustion base case, the temperature is controlled by adjusting the lean ratio of the reacting mixture.

Table 6. Operating parameters for the base case air-combustion cycle (Figure 9).

Components	*Temperature (K)*		*Pressure (bar)*		*Isentropic Efficiency*
	Inlet	*Outlet*	*Inlet*	*Outlet*	
Compressor	*298*	*664.2*	*1*	*15*	*90%*
Reactor	*664.2*	*1200*	*15*	*15*	-
Turbine	*1200*	*672.4*	*15*	*1*	*90%*

Table 7. Operating parameters for the premixed oxy-combustion cycle (Figure 11).

Components	*Temperature (K)*		*Pressure (bar)*		*Isentropic*
	Inlet	*Outlet*	*Inlet*	*Outlet*	*Efficiency*
ASU-Compressor	*298*	*664.2*	*1*	*15*	*90%*
ASU	*664.2*	*1200*	*15*	*15*	*-*
Reactor	*573.9*	*1200*	*15*	*15*	*-*
Turbine	*1200*	*826.5*	*15*	*1*	*90%*
Condenser	*826.5*	*298*	*1*	*1*	*-*
CO_2-Compressor	*300*	*543*	*1*	*15*	*90%*

Table 8. Operating parameters for the non-premixed oxy-combustion cycle (Figure 12).

Components	*Temperature (K)*		*Pressure (bar)*		*Isentropic*
	Inlet	*Outlet*	*Inlet*	*Outlet*	*Efficiency*
Gasifier	*298*	*873*	*15*	*15*	*-*
Reactor	*596.4*	*1200*	*15*	*15*	*-*
Turbine	*1200*	*824.6*	*15*	*1*	*90%*
Condenser	*824.6*	*298*	*1*	*1*	*-*
CO_2-Compressor	*300*	*544.4*	*1*	*15*	*90%*
CO_2 Splitter	*1000*	*1200*	*15*	*15*	*-*
H_2O Splitter	*610*	*1200*	*15*	*15*	*-*

The isentropic efficiency of all turbines and compressors is assumed to be *90%*, and the effectiveness of all heat exchangers is assumed to be *0.95*. Fuel consumption is normalized by the net useful power obtained from the system, and other flow rates are adjusted accordingly. All the calculations and results are for per megawatt (MW) of useful work. Commercial process simulator *Aspen Hysys V7.3* was used to model and simulate the different proposed systems. Peng Robinson equation of state was chosen for the calculation of the properties of gases and mixtures for all proposed systems.

4.3 Results and Discussions

4.3.1 Base case (conventional gas turbine air-combustion cycle)

The base case assumed in this study works on the conventional methane combined cycle gas turbine for power generation. All the results are normalized for *1.0 MW* power output of the turbine. The thermal efficiency of the single stage cycle has been found to be *42.7%* based on the lower heating value of the fuel. Methane consumption for this cycle is *0.047 kg/s* per unit *MW* of power generation. Figure 13 presents the exergy destructions in the various components of the system. It is obvious to find the highest exergy losses in the reactor due to highly irreversible reactions taking place inside the combustion chamber. Exergy destruction in the reactor is found to be *870 kW* per unit *MW* of useful power, which constitutes *82.7%* of the total exergy destruction in the system. The exergy destruction in the turbine is calculated to be *10.9%* and that value in the compressor is calculated to be *6.4%,* which has a second law efficiency of *0.95* each. The second law efficiency of the whole system has been calculated to be *48.7%.*

4.3.2 Non-premixed Oxy-combustion Cycle

The *ITM* integrated reactor system working on the non-premixed oxy-combustion gas turbine cycle is presented in this section. The system is also equipped with a gasifier as shown in Figure 12. Thermodynamic efficiency of the system was found to be *26.4%*, which shows much-improved efficiency than the premixed case; however, still lagging behind the base case by *16.3%*. The most energy intensive unit in the system is the H_2O splitter, followed by the gasifier, and the CO_2 splitter. However, these units are generally equipped with solar power and, hence, add to the CO_2 mitigation efforts. Methane consumption is calculated to be *0.046 kg/s* per unit *MW* of power produced, which is much lower than that value of the premixed case. This can be attributed to the addition of the gasifier, where the energy content of the fuel is increased by converting it into syngas. The exergy destruction in the various components is shown in Figure 14. Highest exergy loss

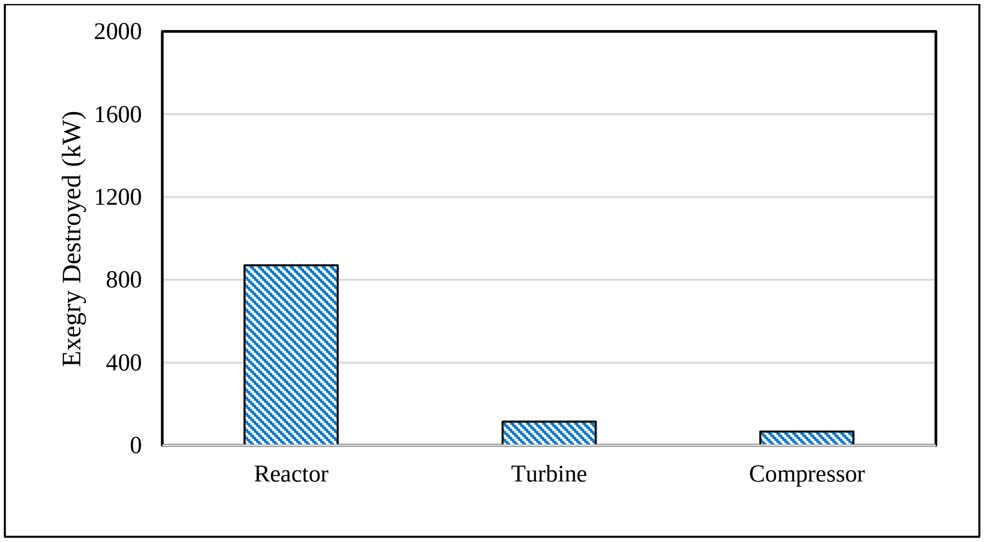

Figure 13. Exergy destruction per *MW* of useful power output in various components of the base case system.

was encountered in the H_2O splitter followed by the condenser, the reactor, the gasifier, and the CO_2 splitter. Large exergy losses in the H_2O splitter, the gasifier, and the CO_2 splitter is due to highly endothermic reactions taking place within the units. Condenser contributes to *939 kW* of exergy loss per unit *MW* of power generation, constituting *21.6%* of the total exergy loss. High exergy destruction in the condenser is due to high temperature gradient between the inlet and exit streams. Exergy destruction in the reactor was found to be *803 kW* as compared to *870 kW* per unit *MW* of power generation for the base case. The reduction in exergy loss in the reactor can be attributed to the increased energy content of the fuel due to gasification. The overall second law efficiency of the cycle was found to be *36.0%,* which still is *12.7%* lower than that of the base case.

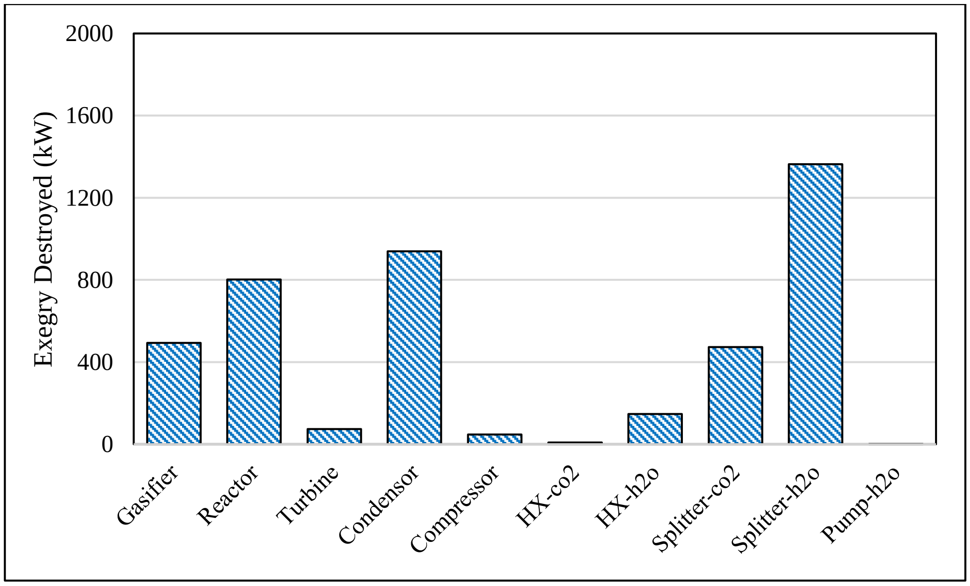

Figure 14. Exergy destruction per *MW* of useful power output in various components of the non-premixed oxy-combustion cycle.

4.3.3 Premixed Oxy-combustion Cycle

The proposed premixed oxy-combustion cycle integrated with an *ASU* based on *ITM* technology, as shown in Figure 11, is presented in this section. The first law efficiency of the system is calculated to be *15.9 %*, which is quite low when compared to the conventional cycle. The cycle consumes fuel in the rate of *0.1 kg/s* per unit *MW* of power production, which is more than two times higher than the base case requirement. The lower thermodynamic efficiency can be attributed to the energy cost associated with the process of air separation. It has been found that a total energy requirement for the ASU, including the air compressor, is *1770 kW* per unit *MW* of power generation, which is basically *25.4%* of the total energy requirement for the cycle. The energy cost associated with the oxygen production using the *ITM* separator is found to be *4.3 MJ/kg* of oxygen. Although exergy loss in the *ASU* contributes only a minor value, as can be seen from Figure 15, it is to be

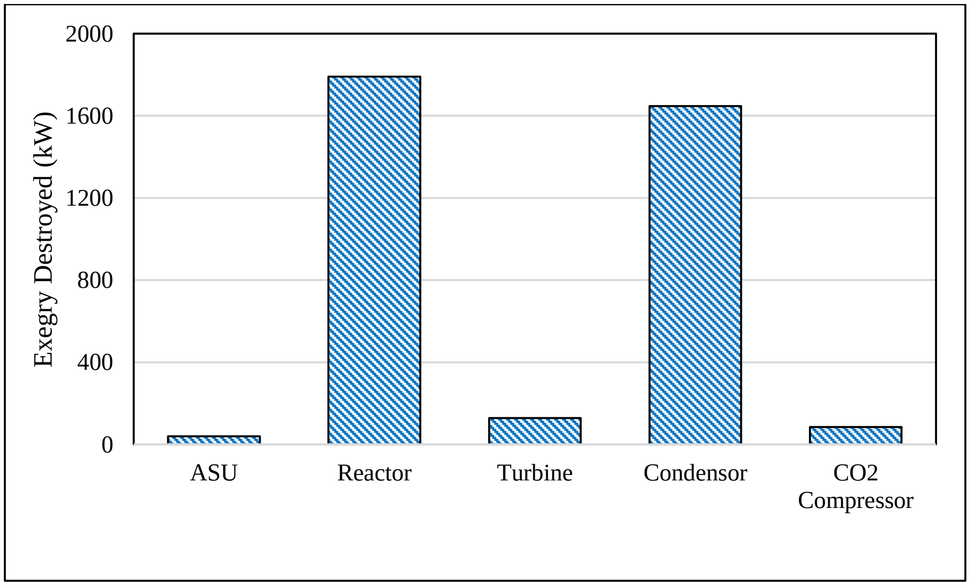

Figure 15. Exergy destruction per *MW* of useful power output in various components of the premixed oxy-combustion cycle.

noted that most of the energy is wasted to the environment through nitrogen waste at high temperature. Highest exergy losses can be observed in the reactor and in the condenser, constituting *48.5%* and *44.6%* of the total exergy destruction of the system, respectively. Exergy destruction in the reactor is *920 kW* higher than that value of the base case for the same *1.0 MW* of power generation. High exergy loss in the condenser can be attributed to the large temperature gradient in the condenser as compensation to achieve high CO_2 purity of about *94.5%*. The second law efficiency of the whole cycle has been found to be *21.3%*, which is again much lower than that of the base case. Significant reduction in the second law efficiency of the system is mainly due to the large exergy loss in the condenser, which is basically bypassed in the base case, where there is no need to separate flue gases for sequestration. Hence, the second law efficiency of the system can be achieved by reducing the temperature gradient across the condenser by integrating it with a recuperation cycle.

4.3.4 Modified Non-premixed Oxy-combustion Cycle

The non-premixed oxy-combustion cycle has been modified to implement the heat recuperation from the exhaust gas out of the gas turbine, as shown in Figure 16. The flue gas is fed to a series of heat exchangers to produce steam to obtain work in two stages via high-pressure and low-pressure turbines. The whole system is normalized for *1.0 MW* of useful work generated from the system.

The thermal efficiency of the modified system was calculated to be *37.8%*, which is *4.9%* lower than that of the assumed base case cycle. The energy requirement of all the components has been decreased by around *30%* per unit *MW* of the power produced, due to the improved overall efficiency of the plant. It can be seen that the first law efficiency of the modified non-premixed cycle is, however, lower than that of the modified pre-mixed cycle. Figure 17 presents the exergy destruction in all the components in the cycle. The cycle is able to extract much work from the flue gases, thus, reducing the exergy loss in the condenser. The exergy destruction in the condenser has been reduced to only *4.9%* of the total value as compared to *21.6%* for the previous case. The second law efficiency of the system, thus, approached *50.4%*, which is better than the base case considered in the present study.

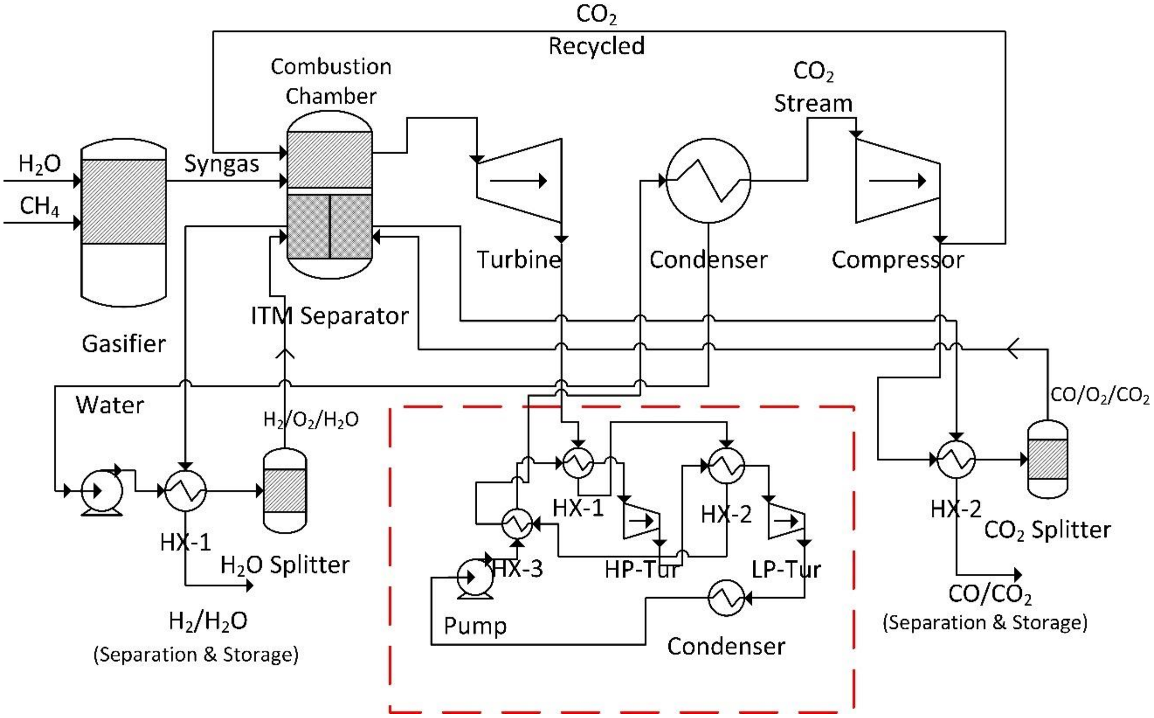

Figure 16. Schematic diagram of the non-premixed oxy-combustion system with heat recuperation.

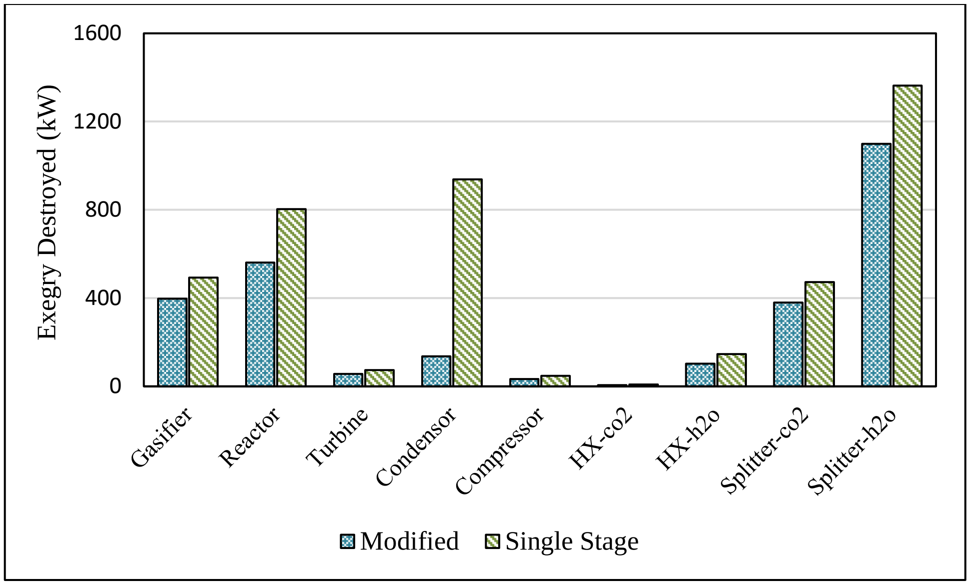

Figure 17. Exergy destruction per *MW* of useful power output in various components of the modified non-pre-mixed combustion cycle.

4.3.5 Modified Premixed Oxy-combustion Cycle

The premixed oxy-combustion cycle discussed earlier, was found to have very low first law and second law efficiencies. The results presented above show that the energy can be extracted from the *ASU* and the condenser using heat recuperation cycles to increase the efficiency of the system. The waste gas from the *ASU*, which is mainly the separated nitrogen, exits at a temperature of *1200 K* and has high energy content that can be used to run a secondary gas turbine. Similarly, energy from flue gases exhausted from the gas turbine can be utilized to regenerate some power using steam cycles. The schematic of the modified cycle is presented in Figure 18. The exhausts from the *ASU* and the gas turbine is directed to a set of heat recuperation units consisting of four heat exchangers and two steam turbines (a high-pressure turbine and a low-pressure turbine). After heat extraction, nitrogen is dumped into the environment and flue gases are redirected to the condenser for the separation of CO_2. The system has been normalized such that the power output of the combined system is *1.0 MW*.

The first law efficiency of the modified system was found to be *42.3%*, which is much higher than that of the previous cycle and very close to the base case cycle efficiency. Fuel consumption was calculated to be *0.049 kg/s/MW* as compared to *0.047 kg/s/MW* for the base case cycle. Total heat requirement by the *ASU* has been reduced to *408 kW* per unit *MW* of useful work obtained from the system, which constitutes 17.3% of the total heat input. This share has been reduced by more than half as compared to the previous case, thanks to energy recovery from the waste gases. The oxygen separation cost was calculated to be *2.2 MJ/kg* of oxygen, which is still much higher than that of the conventional separation cost of *0.725 MJ/kg* of oxygen [107]. It can be seen from Figure 19 that the exergy loss in the condenser has been reduced significantly by implementing the heat recuperation. The exergy loss in the condenser constitutes to *13.2%* of the system total, as compared to *44.6%* for the previous case. The second law efficiency of the cycle, thus, improved by *31.5%* with an overall efficiency of *52.8%*, which is even higher than the base case cycle efficiency.

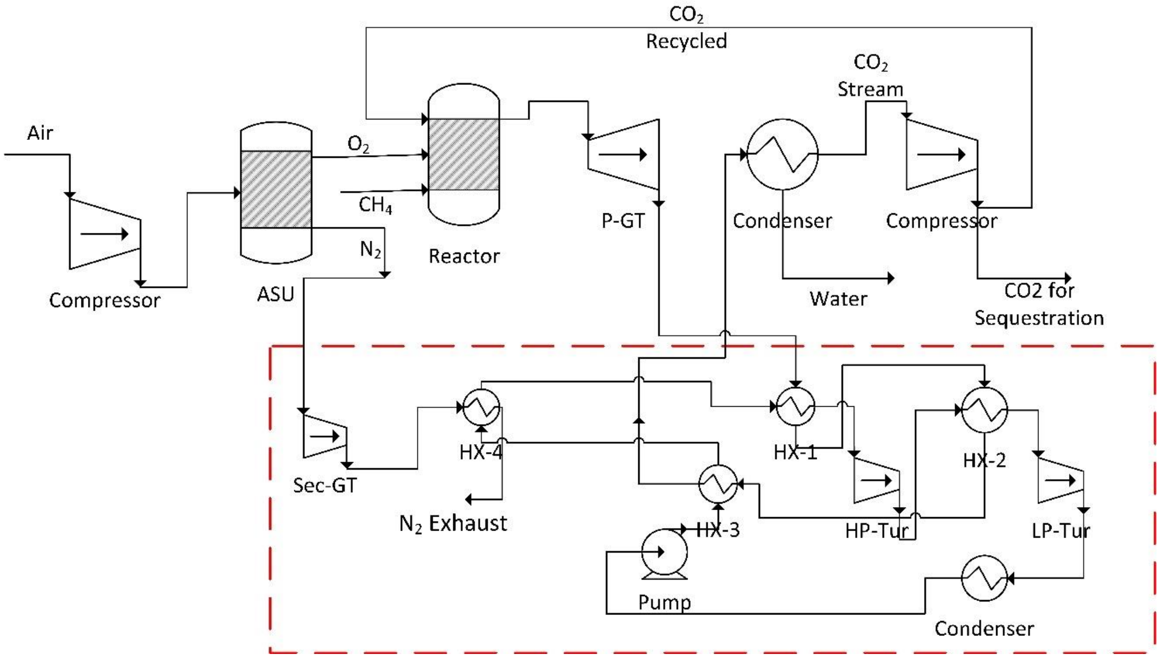

Figure 18. Schematic diagram of the premixed oxy-combustion system with heat recuperation.

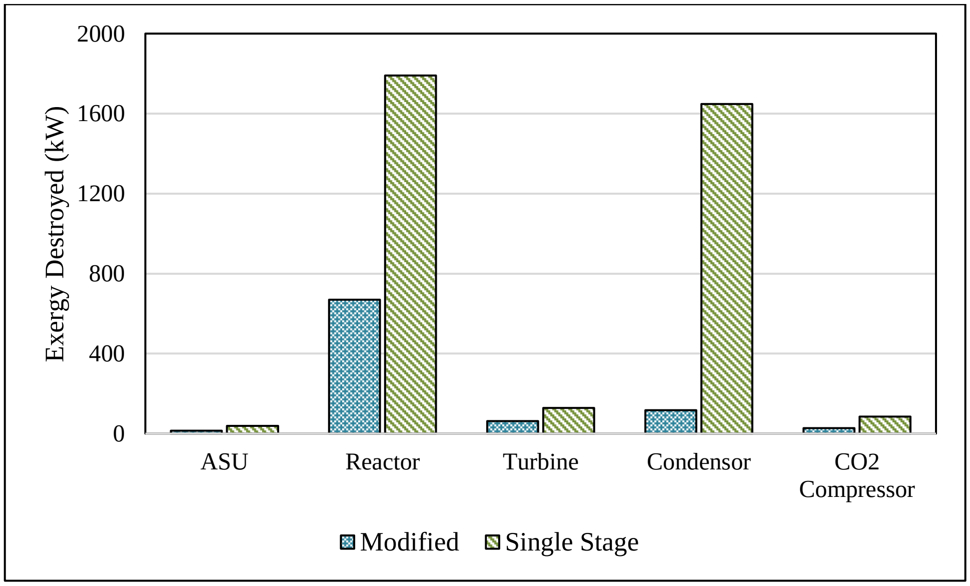

Figure 19. Exergy destruction per *MW* of useful power output in various components of the modified pre-mixed combustion cycle.

4.3.6 Effect of Hydrogen Addition in Premixed Oxy-combustion Cycle

From the above results, it is clear that the proposed premixed oxy-combustion cycle has high feasibility with proper heat recuperation. The first law and the second law efficiencies are very close to the base case conventional air combustion cycle. However, as discussed above, chemical reactions in carbon dioxide environment have been found to be slower than in nitrogen environment. Hydrogen has been proved to be a good fuel additive to improve the combustion efficiency in oxyfuel combustion. Hence, the effect of hydrogen addition on the thermodynamic efficiencies of the premixed cycle has been presented in this section.

Figure 20 presents the percentage reduction in exergy losses in various components with different blends of hydrogen in the fuel stream as compared to pure methane oxy-combustion cycle. It has been observed that with the hydrogen addition, the exergy destruction is reduced in all the components of the system. Exergy destruction in *ASU* is reduced by *7.5%* with *50%* hydrogen blending followed by the reactor with a *4.3%* reduction. Reduction in exergy loss in *ASU* is due to lower oxygen requirement for combustion with hydrogen blending. Effect of hydrogen blending on the first law and the second law efficiencies of the system is shown in *Figure 21*. Both the efficiencies have been found to increase with the hydrogen addition, however, the change is only marginal. The thermal efficiency of the system increased by *0.8%* with *50%* hydrogen blending, taking it marginally above the base case efficiency. The second law efficiency of the system was calculated to be *53.8%* with *50-50* hydrogen/methane blending, which is *1.1%* higher as compared to the base case.

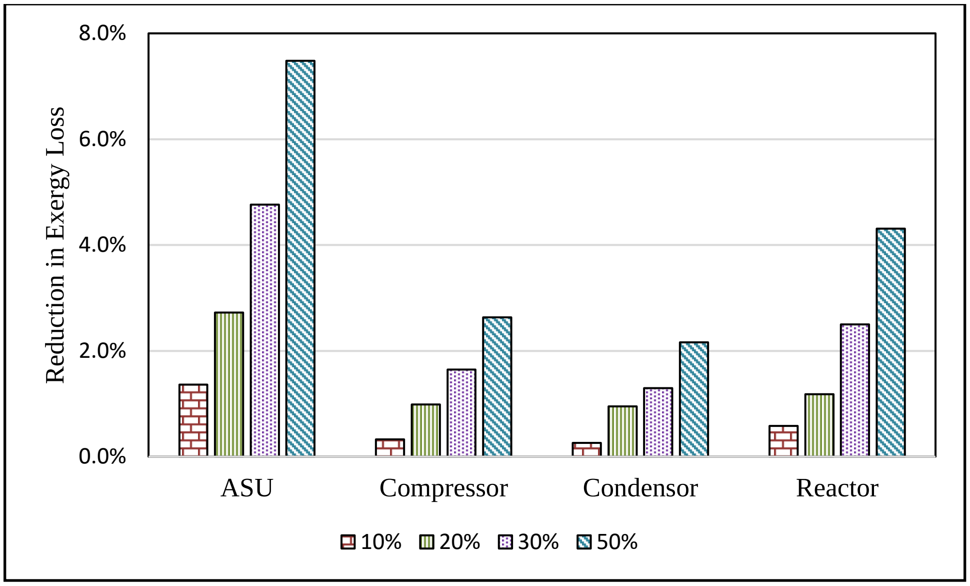

Figure 20. Percentage reduction in exergy destruction in various components with different hydrogen fractions in the fuel stream

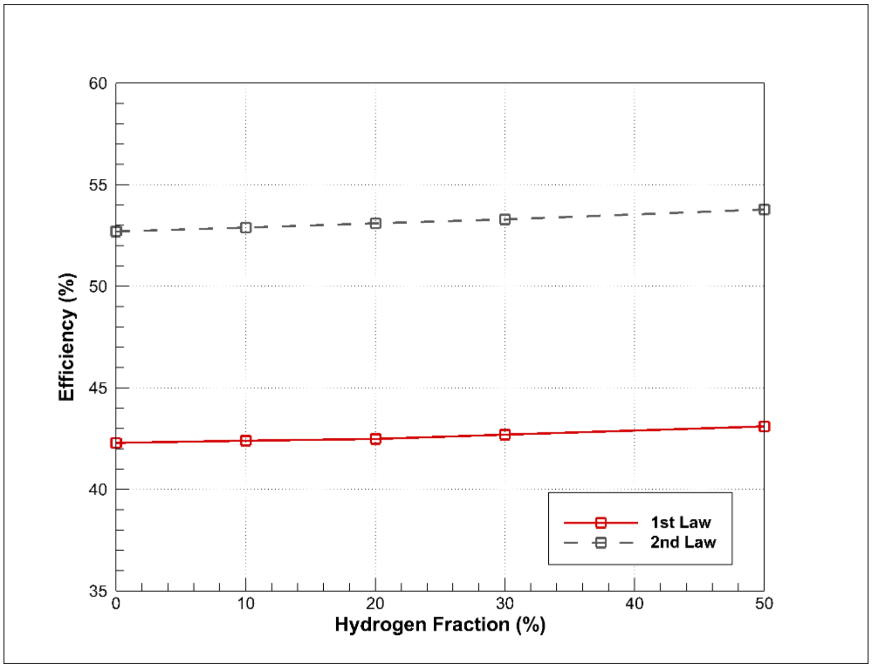

Figure 21. Effect of hydrogen addition on the first law and second law efficiencies of the premixed oxy-combustion cycle

4.4 Concluding Remarks

The present study demonstrated the feasibility of oxy-combustion cycles with various configurations to investigate the effect of carbon capture on the cycle efficiency. The proposed cycles are the pre-mixed oxy-combustion with a separate *ASU* based on *ITM* technology, and the non-premixed oxy-combustion cycle with *ITM* integrated reactor and a gasification unit. The performance of both the cycles has been compared to a basic air-combustion cycle to demonstrate the effect of additional energy cost for oxygen separation on the cycle performance. The thermodynamic analysis of different systems in terms of the first law and the second law efficiencies has been presented. The thermal efficiency of the assumed base case system was calculated to be *42.7%*. The highest exergy loss was found to be in the reactor with an overall second law efficiency of *48.7%*. The non-premixed oxy-combustion system, based on the integrated *ITM* reactor, has lower efficiencies than that of the assumed base case air-combustion cycle. The thermal efficiency of the cycle was found to be *37.8%* as compared to *42.7%* for the base case cycle. The second law efficiency was around *50%*, with the largest exergy destructions in the H_2O splitter and the combustion chamber, where highly irreversible reactions taking place. The proposed integrated *ITM* reactor system is capable of producing syngas via CO_2/H_2O splitting, which can be used as an auxiliary power source when renewable energy for gasification and splitting is not available. The premixed oxy-combustion system was evaluated based on the thermodynamic parameters and was compared to the base case. The cost of oxygen separation via *ASU* dominates as the parameter to affect the cycle efficiency of the proposed premixed oxy-combustion system. It has been found that a significant amount of energy is lost through the waste gases from the *ASU* and, hence, heat recuperation was employed to the unit along with the heat recovery from the flue gases. The modification was able to improve the first law (*42.3%*) and the second law (*52.8%*) efficiencies of the system significantly to be much closer to those of the base case air-combustion cycle. Effect of hydrogen blending on the efficiencies of the premixed system is also evaluated. It was found that the hydrogen addition increases the overall first and second law efficiencies of the system, however, the change is only marginal.

CHAPTER 5

EXPERIMENTAL INVESTIGATIONS OF HYDROGEN-ENRICHED FLAMES

5.1 Experimental Setup and Test Conditions

This study investigates fully premixed hydrogen-enriched methane oxy-combustion flames in a swirl-stabilized model gas-turbine combustor. The combustion takes place at the atmospheric pressure, where the flame is enclosed by a quartz tube opened to the atmosphere.

5.1.1 Test rig for the gas-turbine model combustor

Schematic diagram of the combustor rig is shown in Figure 22. The mixture of hydrogen and methane with different compositions enters the bottom of the rig through a central fuel tube. The end of the tube is closed with *12* radial staggered perforations in three successive planes ensuring cross flow mixing with the oxidizer stream. Oxygen and carbon dioxide enter the mixing plenum through two radial tubes at *35 mm* above the base. The mixing plenum is one meter in length with *L/D* ratio of *~20*, ensuring well premixing of all the gases. The gases are supplied through compressed gas cylinders and the flow rates are regulated using mass flow controllers by Bronkhorst-High-Tech with an uncertainty of *±0.5%* of full scale. The mass flow controllers are operated through a computer interface to deliver the flows such that a particular throat velocity of the mixture is achieved. The

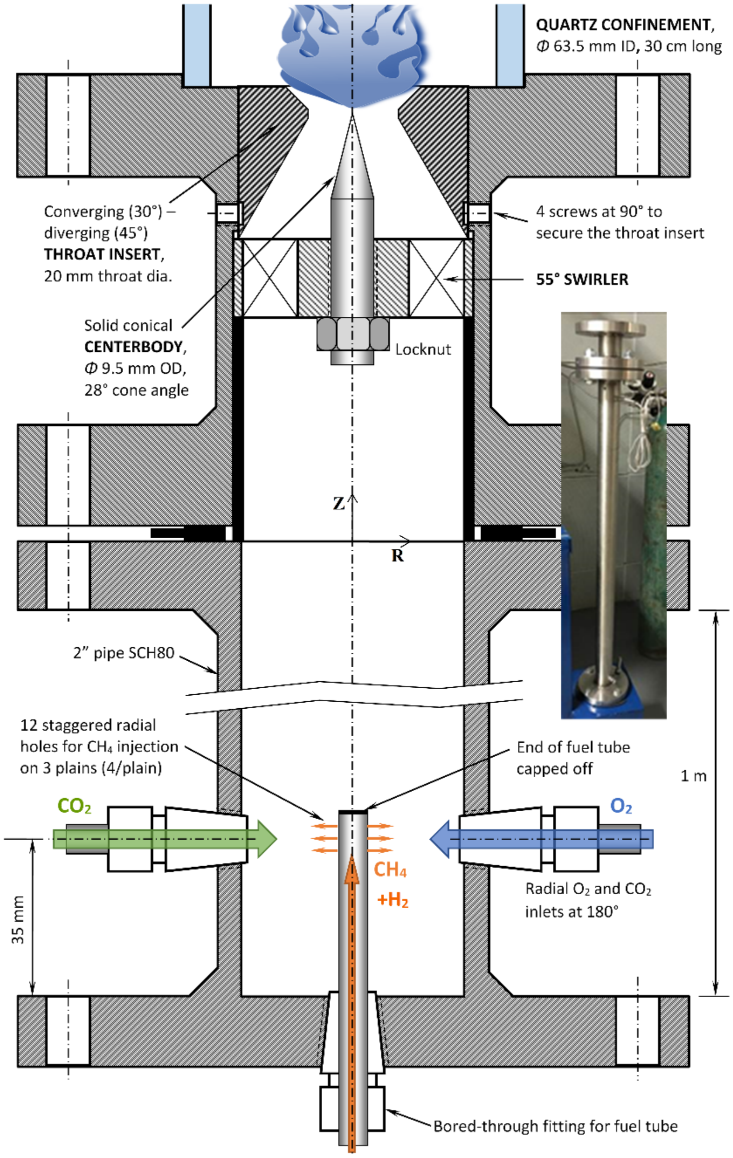

Figure 22. Schematic of the gas-turbine model combustor rig.

fuel delivery tube-line is pre-attached to an emergency shut-off valve to cut the fuel supply in any case flashback explosion.

At the downstream of the mixing chamber and just below the inlet section to the combustor, a *55^o* swirler is attached to provide the necessary vortex for the swirl stabilization of the flame. The swirl number is defined as the ratio of the axial flux of angular momentum to the axial flux of axial momentum and can be calculated using the following correlation [48]:

$$Sw = \frac{2}{3}\left[\frac{1-\left(D_h/D_o\right)^3}{1-\left(D_h/D_o\right)^2}\right]\tan\left(\alpha_{sw}\right) = 0.98$$

(51)

Where, D_h is the hub diameter of the swirler, D_0 is outer diameter of the swirler and α_{sw} is the swirler angle. The swirler is followed by a convergent-divergent nozzle which accelerates the gases through the throat with the diameter of *2 cm*. The 30^o convergent part ensures the gradual acceleration of the flow with minimal swirl reduction. The 45^o divergent part in the inlet section inhibits the sudden expansion of the gases into the combustion chamber. A solid conical projection is placed at the center of the throat which has been found to eliminate the vortex breakdown, blocking the potential path for flame flashback [108]. A high-definition camera is used to capture the images of the selected flames for flame shape processing. The camera is operated at night-vision mode with *ISO* sensitivity set to *1600*, shutter speed of *1/60 s* and *f-stop* setting at *f/5.6*.

5.1.2 Operating conditions

The combustion of hydrogen-enriched methane is carried out in a vertical premixed burner at the atmospheric pressure conditions enclosed by a quartz tube opened to the atmosphere. For all generated flames, the oxidizer stream constitutes a mixture of *30%* oxygen and *70%* carbon dioxide by volume. This composition has been found to have similar flame characteristics as that of conventional air combustion and hence, it has been fixed in this study. Dilution of the oxidizer stream with CO_2 ensures lower flame temperature, which otherwise is impractically high to be retrofitted in an existing power plant.

In this study, we performed three sets of experiments, each at fixed inlet bulk velocity of the mixture ($O_2/CO_2/CH_4/H_2$) at the throat section, typically *4.4 m/s*, *5.2 m/s* and *6.0 m/s*. The hydrogen fraction (*HF*) is varied from *0%* to *75%* against the equivalence ratios (ϕ) ranging from *0.3* to *1.0* to achieve a *2*-dimensional stability mapping. The stability map for the operability of the gas-turbine combustor, in terms of flashback and blowout limits, is recorded at each inlet velocity. The obtained stability map at fixed inlet velocity of *5.2 m/s*, function of *HF* and equivalence ratio at fixed *OF*, is compared with the obtained map at the same velocity but a function of *OF* and equivalence ratio for pure methane. The flame shapes near flashback limit, as well as near blow-out limit, are recorded over a range of hydrogen enrichment level and compared to explore the physics behind flame extinctions. Flame shapes are also recorded and compared at fixed adiabatic flame temperature, fixed inlet velocity, and fixed flow swirl to isolate their effects and investigate the effect of kinetic rates on flame shape. Also, flame shapes are recorded at the fixed adiabatic flame temperature and fixed inlet swirl while varying the inlet velocity is also investigated.

The non-stoichiometric combustion equation for the calculation of adiabatic flame temperature is defined as:

$$\begin{aligned} CH_4+\left(\frac{HF}{1-HF}\right)H_2+\frac{1}{2\phi}\left(\frac{4-3HF}{1-HF}\right)\left\{O_2+\frac{7}{3}CO_2\right\}\rightarrow\left[1+\frac{1}{6\phi}\left(\frac{28-21HF}{1-HF}\right)\right]CO_2 \\ +\left(\frac{2-HF}{1-HF}\right)H_2O+\left(\frac{1}{\phi}-1\right)O_2 \end{aligned} \tag{52}$$

Where HF is the volumetric hydrogen fraction in the fuel stream. The power density of the reactor is defined as rate of energy flow per unit volume per atmospheric pressure:

$$Power\ density = \frac{\dot{m}_{CH_4} \times CV_{CH_4} + \dot{m}_{H_2} \times CV_{H_2}}{Volume\ of\ quartz\ confinement \times combustor\ pressure} \quad (53)$$

Where CV is the standard calorific value and $\dot{m}$ represents the mass flow rates of the fuel.

Heat release factor is a non-dimensional parameter used to quantify the heat release in a combustion process and is given by:

$$\gamma = \left(\frac{T_{ad} - T_0}{T_{ad}} \right) \quad (54)$$

Where T_{ad} is the adiabatic flame temperature and T_0 is the unburnt temperature of the reactant gases.

Reynolds number is defined based on the bulk mixture velocity at the throat of the convergent-divergent nozzle and can be expressed as:

$$\mathrm{Re} = \frac{U_b D_h}{\nu_{mix}} \quad (55)$$

Where, U_b is the mixture bulk velocity, D_h is the hydraulic diameter of the throat and ν_{mix} is the kinematic viscosity of the reactant mixture.

5.1.3 Procedures of measurements

Three sets of experiments are conducted, each at fixed inlet velocity to determine the stability maps and variations of flame shape over a wide range of hydrogen enrichment level. As explained in the above section, the flow rates of all the reactant gases ($O_2/CO_2/CH_4/H_2$) were adjusted in a way to get the desired combined velocity for a given *HF* and equivalence ratio. Hence, a change in any parameter requires the re-adjustment of the flow rates of all the reactant gases simultaneously. The HF in the fuel stream was varied from *0%* to *75%* with the increment of *10%* from *0%* to *50%* and with *5%* increment from *50%* to *75%*. The stability mapping of the flames was scanned for the equivalence ratio ranging from *0.3* to *1.0* in a step of *0.05*. The procedures adopted for the experimental measurements are as follows:

1) Determining a safe ignition point of the burner which is far from the blowout region and flashback point.
2) Adjusting the flow rates of the gases gradually to avoid any sudden jump in the flow meters. The flow rates were adjusted for a particular starting set point at a certain HF which is presumed to be stable.
3) After reaching the stable point for a particular *HF*, the equivalence ratio was increased gradually in steps until the flashback was observed.
4) As the equivalence ratio increases, the flame gets shorter and more violent in nature with the increased noise level. At the flashback point, the noise reaches the maximum and the flame reaches down to the throat causing a mild explosion. The fuel supply was immediately cut-off at this condition using the emergency valve to

stop flame propagation upstream into the plenum. The value of ϕ at which flashback was observed is noted against the selected *HF*.

5) The burner was reignited at the stable point achieved earlier and ϕ was reduced gradually for the same hydrogen fraction until the blowout was observed. At the blowout limit, the flame gets very lean and extinguishes. The value of ϕ is recorded against the particular HF where blowout limit is observed.
6) The procedures from step (*2*) up to step (*5*) are repeated for all the hydrogen fractions until we achieved the two-dimensional stability map for a particular throat velocity.
7) The whole procedure was repeated to quantify the stability mapping for the other two throat velocities to achieve the mappings for the three sets at *4.4 m/s*, *5.2 m/s* and *6.0 m/s.*

5.2 Results and discussions

5.2.1 Stability Mapping

The stability mapping is quantified by identifying the flashback and blow-out limits of the flames at three sets of combined velocities of the reactant gases at the throat. Stability map at inlet bulk velocity of *5.2 m/s* is first presented on the contours of adiabatic flame temperature (*AFT*), power density (*PD*), inlet Reynolds number (*Re*), and mixture mass flow rate $\dot{m}_{mix}$. The obtained stability map at fixed inlet velocity of *5.2 m/s*, function of *HF* and equivalence ratio at fixed *OF*, is compared with the obtained map at the same velocity, but a function of *OF* and equivalence ratio for pure methane. This is followed by the analysis of the effect of inlet flow velocity on flashback and stability limits of the generated flame.

5.2.1.1 Stability mapping at 5.2 m/s

Figure 23 presents the blow-out and flashback limits with varying the hydrogen fraction and equivalence ratios at oxygen fraction (*OF*) of *30%* and throat velocity of *5.2 m/s* against the contours of adiabatic flame temperature. It has been observed that the addition of hydrogen shifted both the blowout and flashback limits towards the leaner side. The blowout limit increases from the equivalence ratio of *0.75* with pure methane combustion to *0.3* with *75%* HF. The blowout limit follows an almost linear trend with increasing *HF* which can be attributed to increased chemical kinetics with the addition of hydrogen resulting in more stable flames in the leaner region. However, due to vigorous reaction with the percentage increase of hydrogen towards the richer region, the flashback occurs sooner than the methane-rich flames. The flashback limit reduces from the equivalence ratio of *1.0* at *50% HF* to *0.8* at *75% HF*. It is obvious that the adiabatic flame temperature has little effect of hydrogen addition and hence, the flame limits show no apparent correlation with it. Similarly, the stability mapping does not exhibit a relation with the power density (MW/m^3/bar) of the combustor as depicted from Figure 24. The flashback and blowout limits are mainly a function of Damkohler number. Provided that the stability mapping was carried out at the constant throat velocity of *5.2 m/s*, the stability limits are largely governed by the reaction time scale or the flame speed. It is known that the hydrogen fraction has a tremendous effect on the reaction kinetics although it hardly affects the flame temperature or power density.

The hydrogen fraction has an inverse relation with both the Reynolds number and reactant mixture mass flow rates. It is expected that a decrease in Reynolds number would bring both the flashback and blowout limits to the richer side by increasing the turbulence level in the flow. However, it can be seen from Figure 25 and Figure 26 that the stability limits are following the Reynolds number and mass flow rates, although the relation is not direct. The phenomenon can be understood by the fact that the addition of hydrogen does not only affect the flow pattern but also the chemical kinetics inside the combustor. In this study, two conflicting parameters are considered, one is the hydrogen enrichment which enhances the chemical kinetic rates and the second is the oxy-combustion mode in the presence of CO_2 which slows the chemical kinetic rates. Figure 27 explores the effects of *HF* and *OF* on shifting the stability map limits through comparing the stability limits of methane oxy-combustion (*HF=0.0*) with those of hydrogen-enriched methane oxy-combustion (*OF=30%*) at the same inlet velocity of *5.2 m/s*. It is apparent from the figure that both the

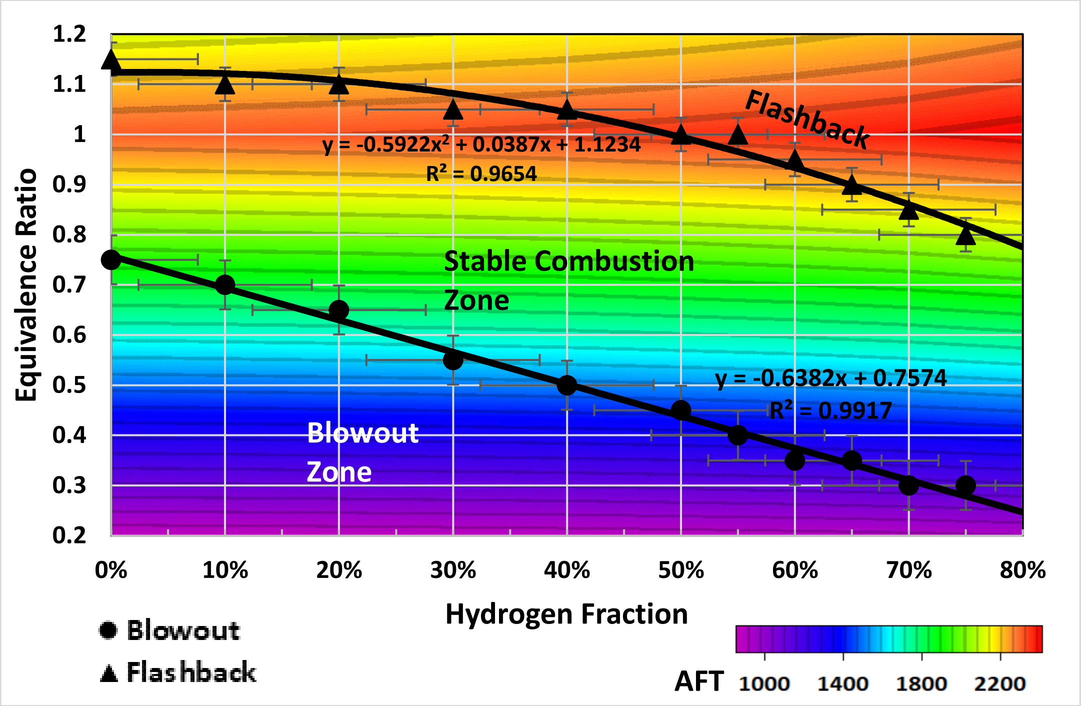

Figure 23. Flame stability mapping against the contours of adiabatic flame temperature (*AFT*) at the throat velocity of 5.2 m/s.

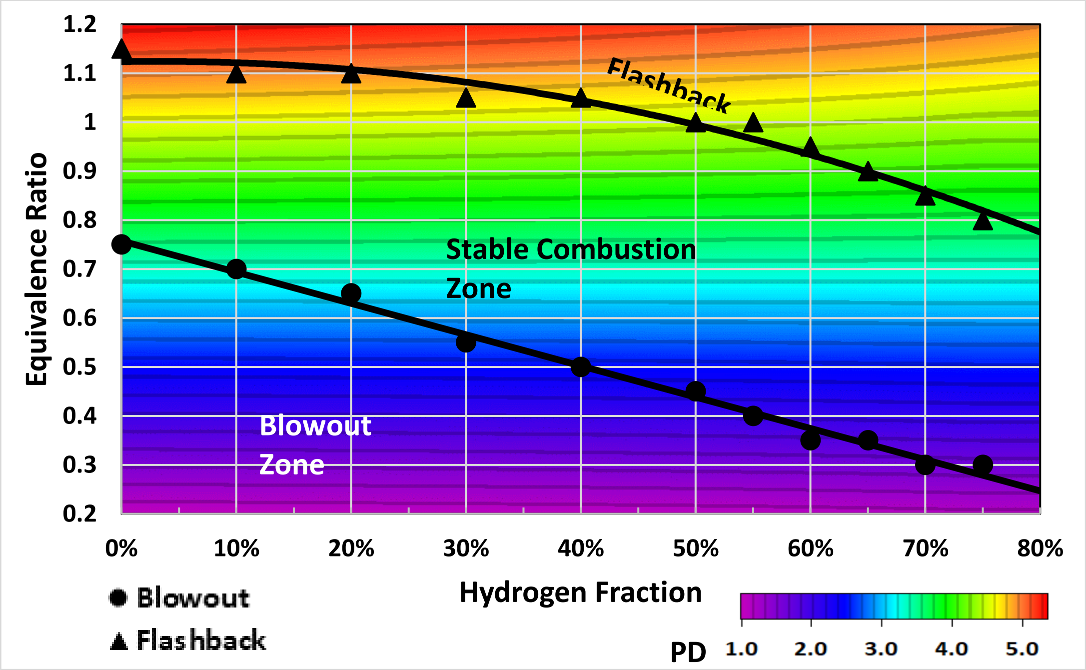

Figure 24. Flame stability mapping against the contours of power density (*PD*) at the throat velocity of 5.2 m/s.

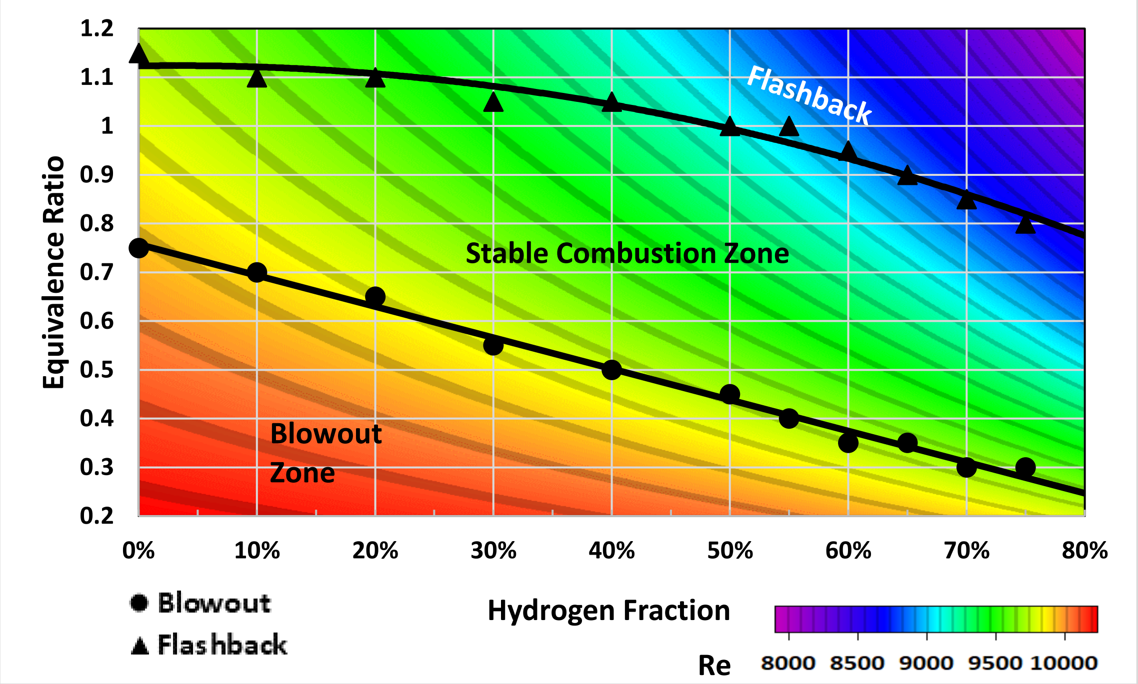

Figure 25. Flame stability mapping against the contours of Reynolds number (*Re*) at the throat velocity of 5.2 m/s.

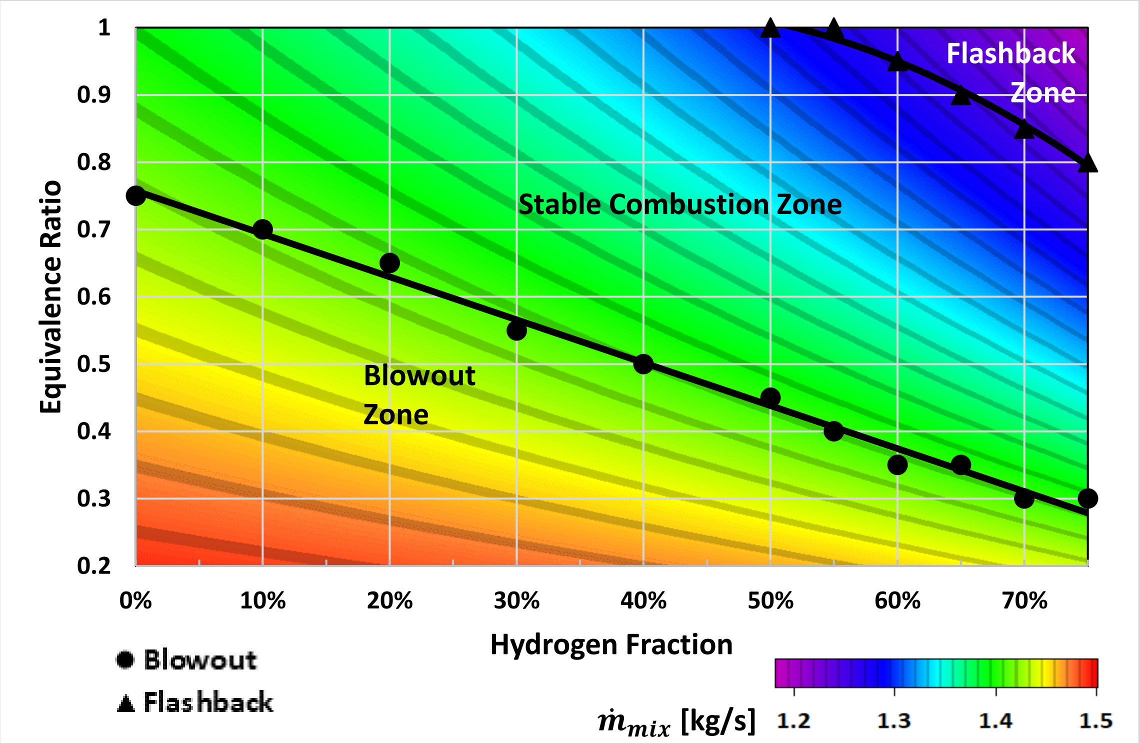

Figure 26. Flame stability mapping against the contours of the reactant mixture mass flow rate ($\dot{m}_{mix}$) at the throat velocity of 5.2 m/s.

cases, hydrogen enrichment at fixed *OF* and oxygen enrichment at fixed *HF*, have a similar effect on shifting the blow-out limit to the very lean operation zone. This may be attributed to the increased reaction kinetic rates for both cases which enhances the burner capability of holding the flame at very lean burning conditions. A similar conclusion on the effect of CO_2-diluted mixture on limiting flame stability is reported by Amato et al. [109]. The flashback limits are shifted from the near stoichiometric combustion zone to the very lean combustion zone while increasing the *OF* from *30%* to *70%* for pure methane oxy-combustion. However, increasing *HF* from *30%* to *70%* at fixed *OF* of *30%* shifts the flashback limit toward the lean condition but remains near the stoichiometric conditions, i.e. increasing *HF* results in slight changes in the flashback limits as compared to the significant changes in the flashback limits when increasing the *OF*, as shown from the slope of the flashback lines for both cases in Figure 27. On the other hand, for the same *OF* of *30%*, hydrogen enrichment of *30%* can significantly widen the blow-out limit in terms of equivalence ratio from 0.8 down to 0.55, and the flashback limit is slightly shifted from equivalence ratio of *1.2* down to 1.1. Increasing *HF* above *50%* does not result in significant changes on static stability limits, blow-out, and flashback, at fixed inlet velocity. This may be attributed to the reduction in the total inlet fuel mass flow rate when substituting methane with hydrogen at fixed inlet flow velocity. Hydrogen enrichment is effective in the zone from *HF=20%* up to *HF=50%,* and oxygen enrichment is also effective in a similar zone from *OF=20%* up to *50%,* with wider stability boundaries for hydrogen enrichment as compared to oxygen enrichment.

The stable flame region lies below the flashback curve and above the blowout curve as presented in *Figure 28*. It can be seen that the operating window of the heat release factor

(γ) increases significantly with the hydrogen addition to the fuel stream. *LBO* limit decreases linearly with the hydrogen addition, thus ensuring stable flames at lower flame temperatures. Moreover, the flashbacks were observed at higher γ with the increasing hydrogen fractions, attaining a maximum value at *55% HF*, and then decreasing gradually with any further increase. Thus, the flames are stable over a wide flame temperature operation at around *50-55%* hydrogen enrichment of methane. Pure methane oxy-flame was found to be stable at the equivalence ratio of *1.0*, however, any attempt to increase the hydrogen fraction beyond *55%* was failed and the flame was extinguished as a result of flashback. Increase in hydrogen fraction in the fuel blend increases the laminar flame speed and the flame tries to propagate upstream of the reactant gases resulting in an earlier flashback when compared to pure methane flame.

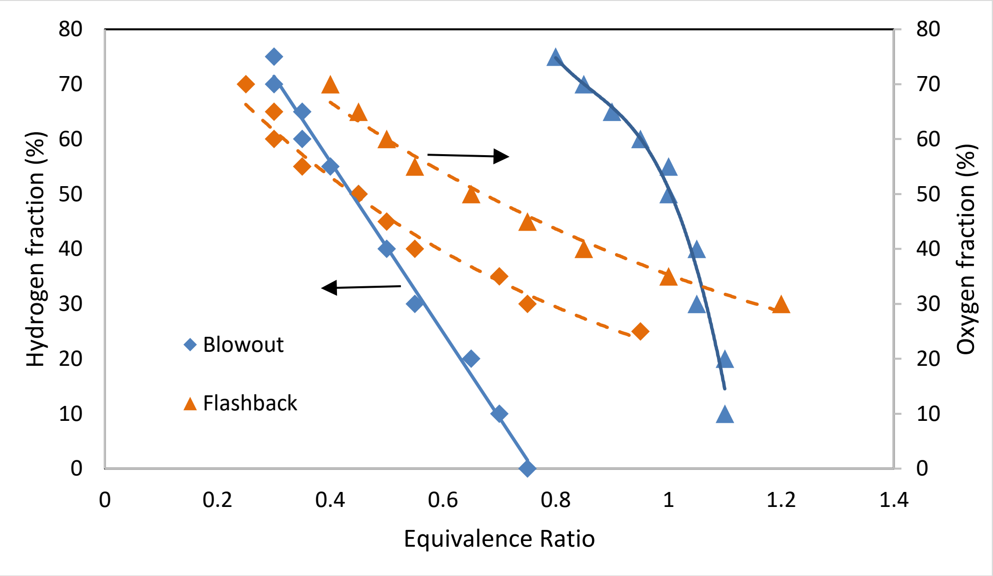

Figure 27. Comparison of flame stability limits of methane oxy-combustion (HF=0.0), presented by dotted lines, with those of hydrogen-enriched methane oxy-combustion (OF=30%), presented by solid lines, at the same inlet velocity of 5.2 m/s.

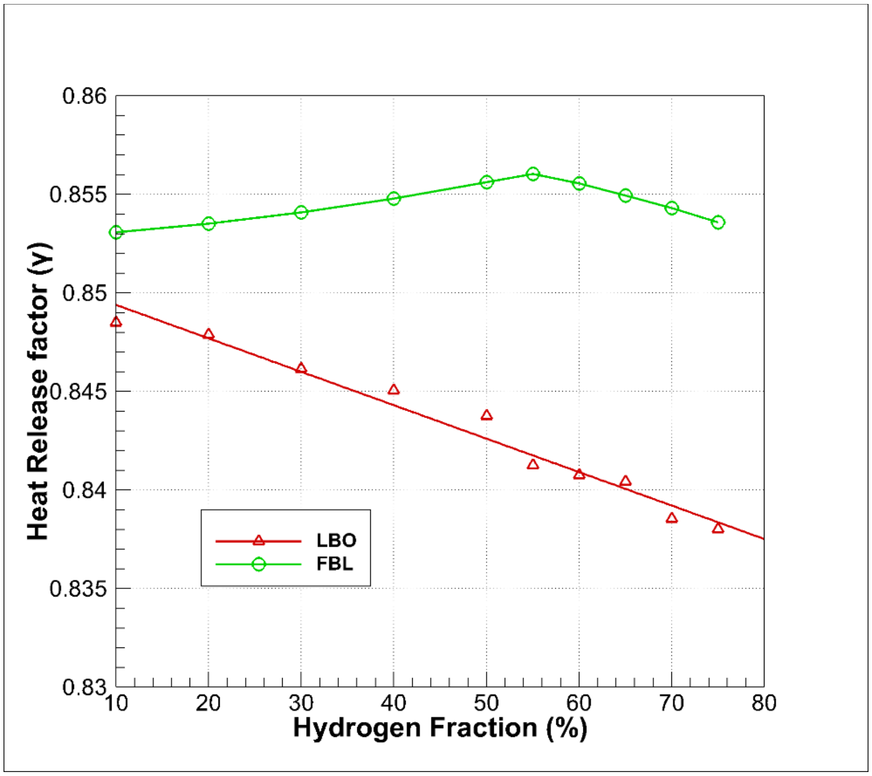

Figure 28. Measured flame stability mapping as a function of heat release factor (γ) and hydrogen fraction.

5.2.1.2 Effect of inlet bulk velocity

In this section, we try to explore the effect of changing inlet bulk velocity (*4.4 m/s, 5.2 m/s and 6 m/s*) on shifting the stability limits, flashback and blow-out, as a function of *HF* and equivalence ratio.

Figure 29 and Figure 30 and presents the flame flashback and blowout limits at various throat velocities. At a particular fuel composition, increase in throat velocity tightens the flashback limit and widen the blowout limit. Actually, flame propagation does not only depend on the fuel type but also on the flow regime. It has been established that the ratio of turbulent to laminar flame speed is a function of flame fronts in the two regimes as [110]:

$$S_T / S_L = A_T / A_L \tag{56}$$

Where, S_T and S_L are the turbulent and laminar flame speeds, whereas A_T and A_L are the turbulent and laminar flame front area, respectively. The turbulent flame front structure gets distorted but intact and hence, the increase in flame front area is a function of turbulent intensity. It has been observed that the turbulent flame speed varies linearly with the turbulent fluctuation magnitude as [87,111]:

$$S_T = S_L + K \cdot u' \tag{57}$$

where, K is an empirical constant whereas u' is the root mean square turbulent fluctuation magnitude. The inference can be taken from the above discussion to explain the observations on the effect of inlet velocity on shifting the stability limits. Increasing throat velocity affects the swirl number causing a highly turbulent flow, which evidently increases the flame speed. An increased flame speed would result in early flashback and elongated blowout limits. For *60 % HF*, the flashback occurs as early as at an equivalence ratio of *0.85* for inlet velocity of 6.0 m/s compared to an equivalence ratio of *1.0* for inlet velocity of *4.4 m/s*. However, the blowout limits for the throat velocities of *5.2 m/s* and *6.0 m/s* seems to coincide, whereas, at *4.4 m/s*, blowout occurs at richer flames. It is suggested that this anomaly comes from the fact that the blowout is observed at much higher Reynolds number as compared to flashback, indicating that the turbulence is reaching the asymptotic value at the throat velocity of *5.2 m/s* at lower equivalence ratios. Thus, the effect of turbulence is no longer a vital player in affecting the flame speed. Temperature profiles are recorded in this set of experiments to give an indication about the progress and intensity of reactions within the combustor and to serve as a basis in the literature for validation and improvement of the numerical models. The effect of hydrogen enrichment level on the distributions of temperature within the combustor is investigated. The temperatures are recorded as close as possible to the flame core due to the limitations of the thermocouple range of operation and the interfere of the thermocouple probe with the generated turbulent reacting flow field. Figure 31 presents the axial temperature profiles at stoichiometric combustion conditions and inlet velocity of *5.2 m/*s for a range of hydrogen enrichment level, from *HF=0%* up to *HF=30%*. Similarly, and under the same operating conditions, radial temperature profiles at a distance of *Z/D=0.92* from the base of the quartz tube, combustion chamber inlet, are presented in Figure 32. It is obvious and expected that hydrogen enrichment should enhance the rates of reactions and improve the temperature, and the temperature should reduce toward the combustor exit in the axial direction. However, the results do not show a significant effect on the combustion temperature at the hydrogen enrichment level of *10%*. This may be attributed to the low inlet hydrogen mass flow rate at this level of enrichment to balance CH_4 in order to keep the same inlet velocity of *5.2 m/s*. A similar conclusion is reported for hydrogen enrichment level below *10%* in our previous work on the non-premixed combustion mode [112].

As per Figure 32, temperature levels at the center of the combustor is higher within the axial main combusting stream and flame core and decreases in the radial direction where flow recirculations and heat loss through the combustor wall are intense. At lower hydrogen fractions, the slope is almost linear while as the hydrogen fraction increases, the temperature gradient increases and the flame takes the shape of hill and valley. This can be explained by increased chemical kinetics with increasing hydrogen fraction resulting in more confined flames.

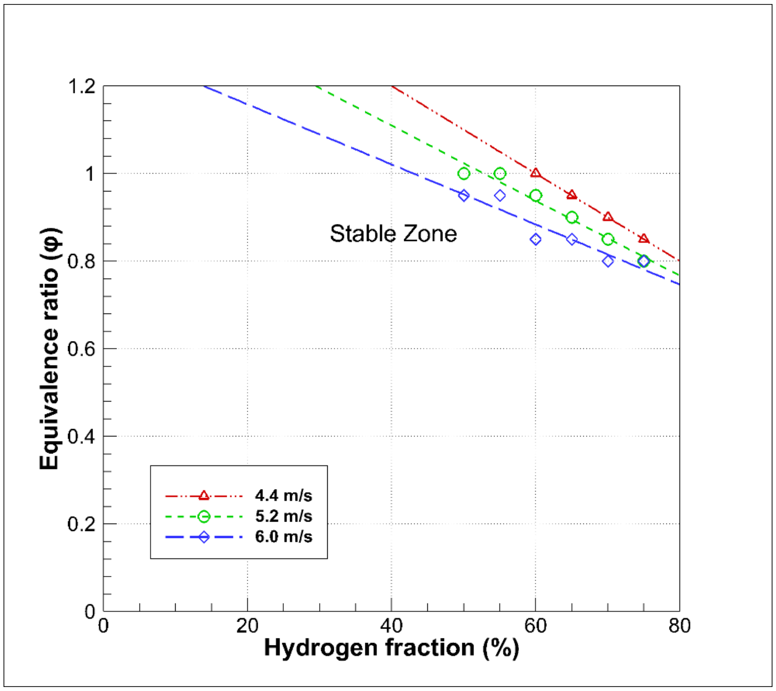

Figure 29. Flashback limits at the throat velocities of 4.4 m/s, 5.2 m/s & 6.0 m/s.

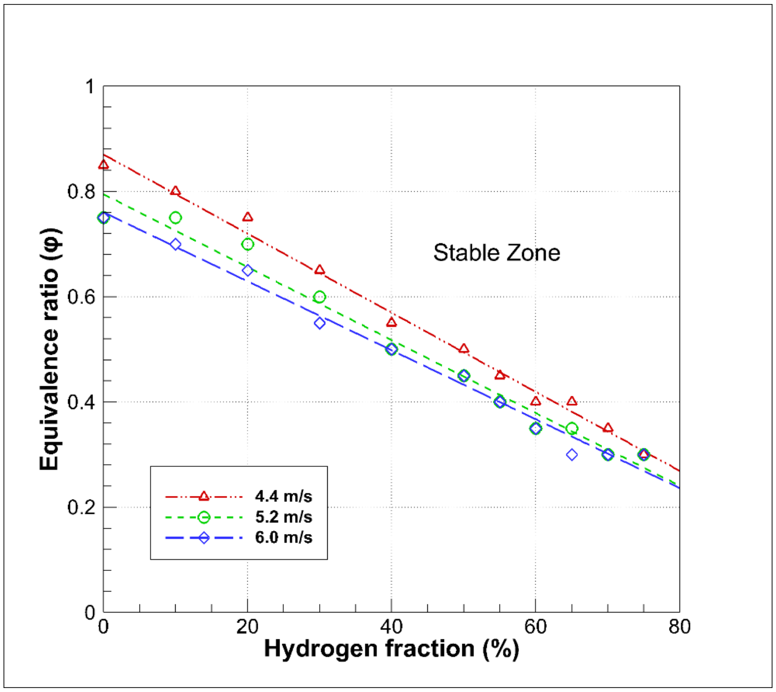

Figure 30. Blowout limits at the throat velocities of 4.4 m/s, 5.2 m/s & 6.0 m/s.

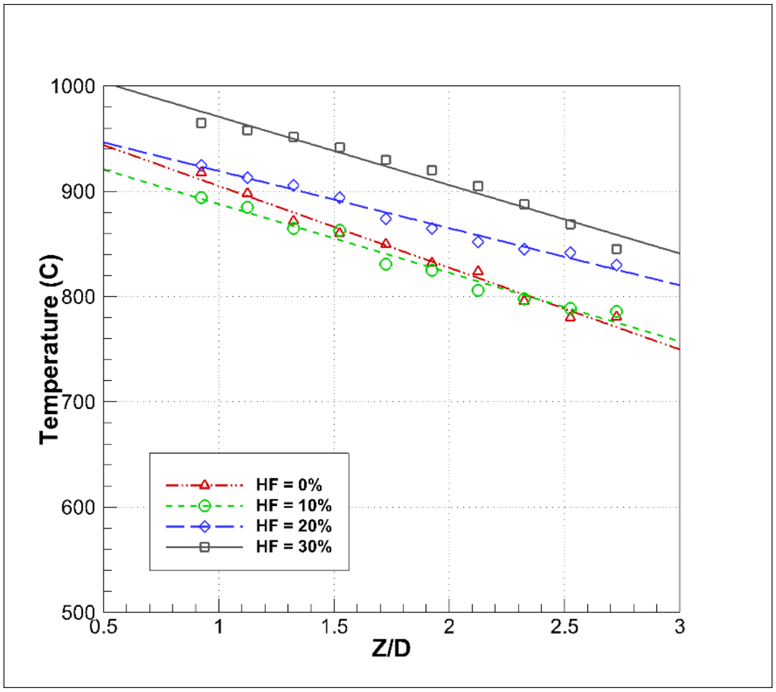

Figure 31. Axial temperature profiles at stoichiometric combustion conditions and inlet velocity of 5.2 m/s for a range of hydrogen enrichment level.

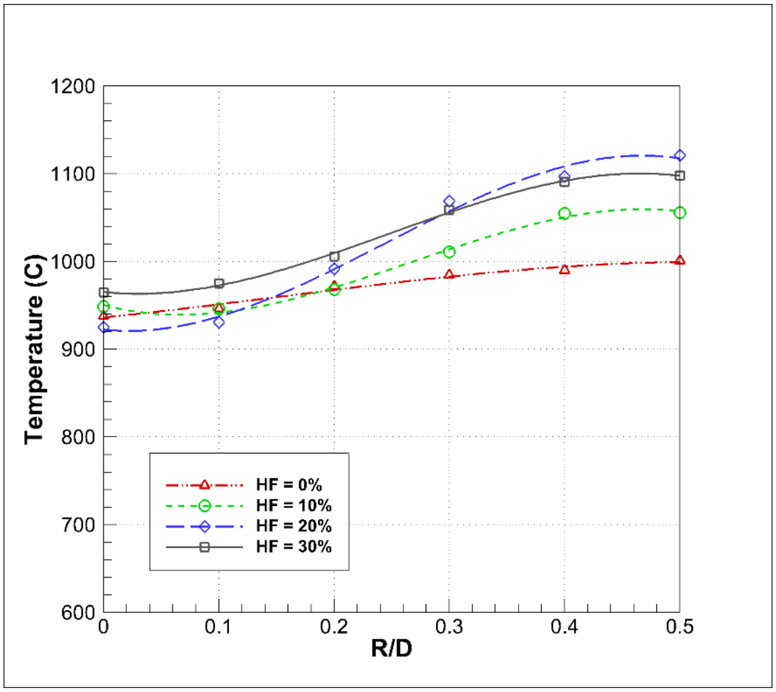

Figure 32. Radial temperature profiles at stoichiometric combustion conditions and inlet velocity of 5.2 m/s for a range of hydrogen enrichment level, and at Z/D=0.92 from the inlet of the combustion chamber.

5.2.2 Flame shape analysis

For a deeper understanding of the flame characteristics, visualization of flame shapes is presented in this section. Effect of hydrogen addition at the equivalence ratio of *1.0* for all the investigated throat velocities is displayed in Figure 33. The effect of hydrogen fraction on *AFT* is marginal and a rise of around *200 K* is observed from *0%* to *75% HF* as can be seen from Figure 23. The effect of *AFT* is evident through waxing flame brightness as we go from the left to the right. Moreover, hydrogen addition has a significant effect on the flame shape. With pure methane, the flames can be seen to spread over the reactor to take the shape of the confinement. However, increasing hydrogen percentage is characterized by more violent and compact flames, implicating higher chemical kinetics and faster flame speeds. With increasing hydrogen fractions, the audible noise of the combustion dynamics increases until the flashback is observed. For the throat velocity of *4.4 m/s* the flashback occurs after *50% HF,* while for *5.2 m/*s and *6.0 m/s* the flashback was observed after *40% HF*. This is due to increased turbulent flame speed, which is also characterized by higher audible noise, as explained in the earlier section. Other than that, no significant effect of throat velocity was observed on the flame shapes.

Figure 34 shows the effect of equivalence ratio (ϕ) on the flame structure at *50% HF*. Three prominent flame shapes can be observed viz. cup shape at lower ϕ, v-shape at intermediate ϕ and vase shape at higher ϕ. The lower equivalence ratios are characterized by lower *AFT* and lower flame speed. The flames have lower brightness and indistinct shape near blowout region. With increasing ϕ, the flames go through a transition phase having *V*-shaped flames and then vase shaped high-noise flames with shorter flame height. The throat velocity does not seem to have much impact on the flame structure at higher values of ϕ; however, for $\phi < 0.8$, the effect is more prominent. The transition from cup shape to vase shape occurs between $\phi = 0.75 - 0.80$ at the throat velocity of *4.4 m/s*; however, at higher velocities, the transition is observed between $\phi = 0.65 - 0.70$ and $\phi = 0.60 - 0.65$ for the throat velocities of *5.2 m/s* and *6.0 m/s*, respectively. Moreover, at lower equivalence ratios, the flame brightness is also found to be increasing with increasing throat velocity, albeit characterized by same *AFT* which is a function of ϕ and *HF* only and does not depend on the flow rates. The observations suggest that the effect of throat velocity is more prominent at lower ϕ, implicating that the turbulent flame speed comes into a major role at lower equivalence ratios.

It is observed from the presented flame shapes in Figure 34 that there is an equivalence ratio at which a transition of flame stabilization from the inner shear layer (*ISL*) to the outer recirculation zone (*ORZ*) occurs. The value of this equivalence ratio is different from operating velocity to another. This important transition of the flame macrostructure is observed to be associated with the onset of dynamic thermo-acoustic instabilities. This transition occurred at equivalence ratios of *0.7*, *0.63* and *0.6* for the inlet velocities of *4.4 m/s*, *5.2 m/s* and *6.0 m/s*, respectively. A similar transition in the flame shape was also observed by Taamallah et al. [113] for both air and oxy-combustion modes. They reported that the flame transition is governed by the extinction strain rate and may occur at different laminar flame speed and adiabatic flame temperature. They defined a non-dimensional number characterizing the flow in the *ORZ*, that is the Strouhal number. This number is independent of the flow Reynolds number and is mainly a function of the inlet flow velocity. They showed that the inlet flow velocity is a more relevant parameter than the inlet flow Reynolds number in order to maintain similar flow conditions in the *ORZ*. These findings are confirmed in the present study showing the significant effect of inlet bulk velocity on flame stabilization behavior. However, we observed here that this effect is significant when the inlet velocity is raised from *4.4 m/s* up to *5.2 m/s*, and insignificant when the inlet bulk velocity is raised from *5.2 m/s* up to *6 m/s.* The value of the transition equivalence ratio is reduced while increasing the inlet bulk velocity. This may be attributed to the increased level of the azimuthal *ORZ* spinning frequency at higher velocities.

To explore whether or not the adiabatic flame temperature has an effect on the transition of flame shape and, accordingly, on the operability boundaries of the flame, flame shapes are captured at fixed *AFT* of *2000 K* and variable hydrogen fraction and compared as presented in Figure 35. The results showed that the flame shapes do not depend on the *AFT*; however, the hydrogen fraction affects the flame shapes significantly. This implies that the adiabatic flame temperature does not govern the flame stability. The same conclusion was reported by Amato et al. [18]. Addition of hydrogen shortens the flame height due to increased chemical kinetics. Flame shapes near the blowout and flashback limits are presented in Figure 36. Both the limits are observed at lower equivalence ratios with increasing hydrogen fraction. Hence, the flame brightness decreases as we go towards higher hydrogen fraction. Near the blowout region, with increasing hydrogen fraction, flames appear to take the shape of the quartz confinement with the reduction in the flame height. However, flame shapes near the flashback region are observed to be invariant with the increasing hydrogen fraction, except that the brightness decreases.

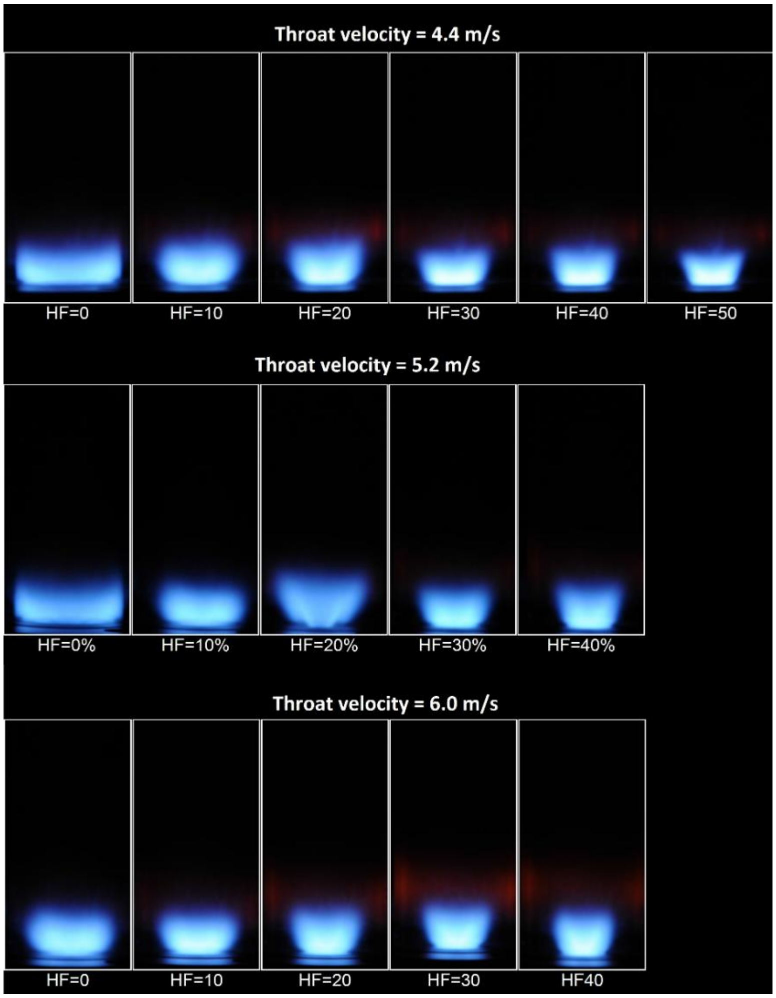

Figure 33. Flame images at an equivalence ratio of 1.0 over a range of hydrogen enrichment for different throat velocities.

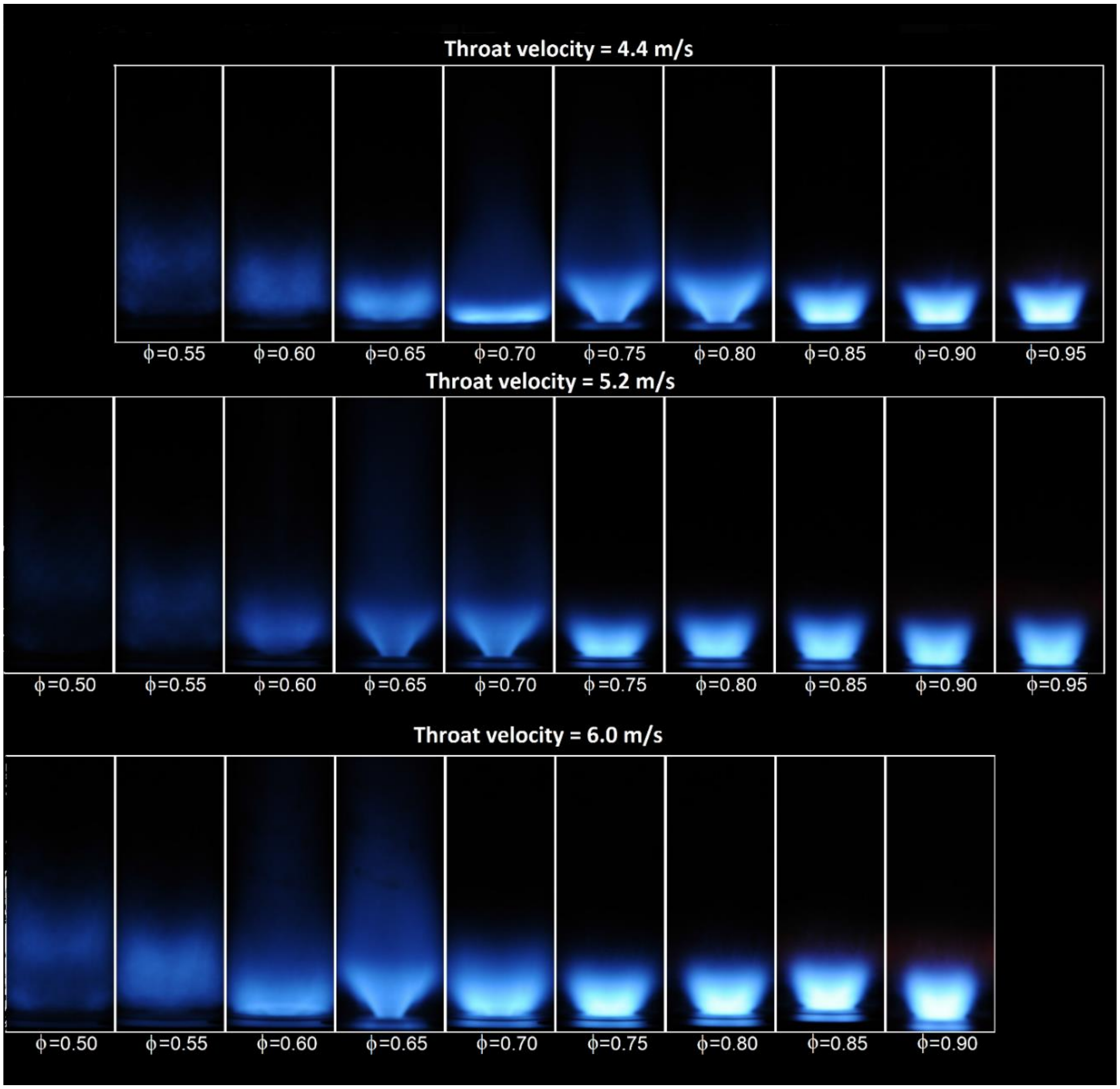

Figure 34. Flame images at the hydrogen fraction of 50% over a range of equivalence ratio for different throat velocities.

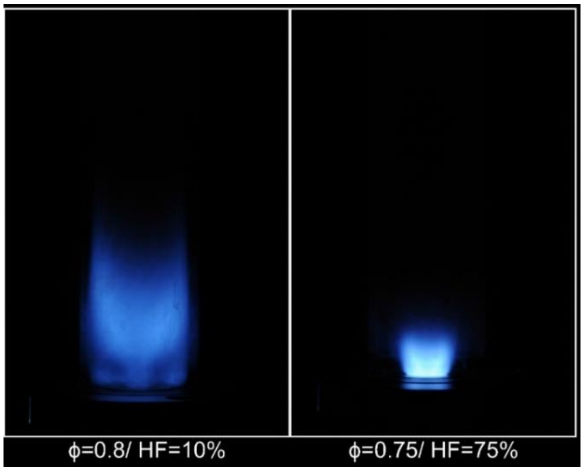

Figure 35. Flame shapes captured at fixed AFT of 2000 K for inlet bulk velocity of 5.2 m/s.

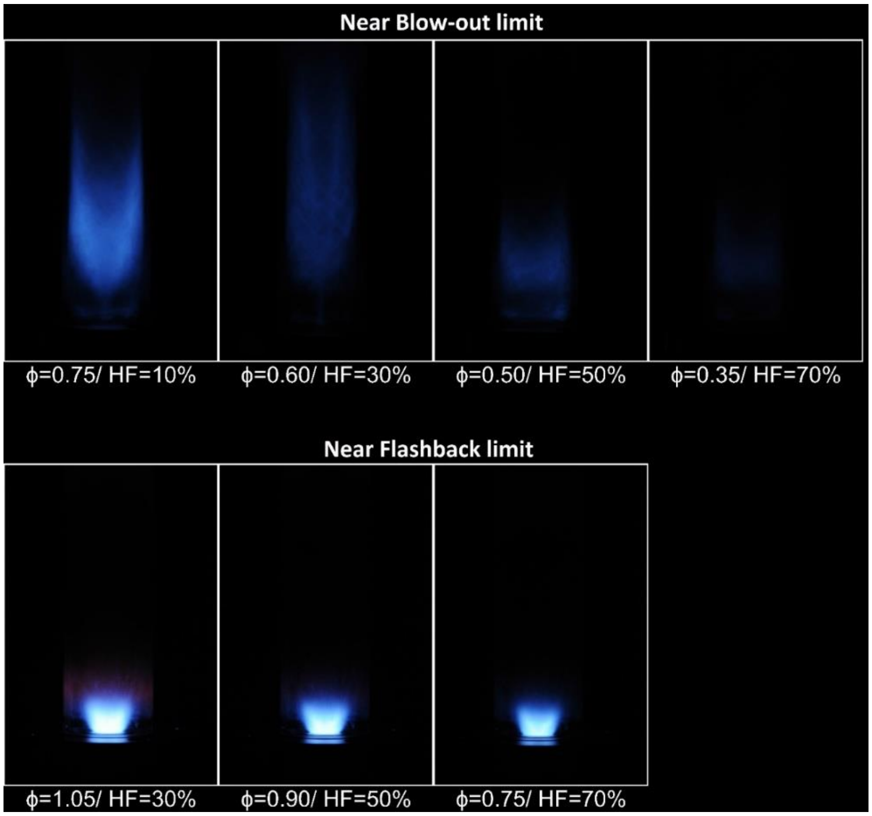

Figure 36. Flame shapes captured near blowout and flashback limits for inlet bulk velocity of 5.2 m/s.

5.3 Concluding Remarks

Experimental investigations on the characteristics of hydrogen-enriched flames in a swirl-stabilized premixed combustor have been carried out through stability mapping and flame visualization. Mass flow rates of the reacting gases have been adjusted to obtain three sets of total throat velocities viz. 4.4 m/s, 5.2 m/s and 6.0 m/s. A two-dimensional stability mapping was obtained by varying ϕ and *HF* over ranges of *0.3* to *1.0* and *0%* to *75%*, respectively. Selected flames at $\phi = 1.0$ with varying HFs and at $HF = 50\%$ with varying equivalence ratio have been imaged using a high definition camera. Results indicated that both the flashback and blowout limits tend to move towards the leaner side with increasing hydrogen fraction in the fuel stream indicating increased flame speed. Although, the stability limits are observed to follow the Reynolds number based on reactant gases velocity at the throat and the throat diameter. The findings can be comprehended from the fact that increasing hydrogen fraction in the fuel stream does not only reduces the Reynolds number but also enhances the kinetics of combustion. Reduction in Reynolds number is characterized by lower turbulence and hence, slower flame speed; however, increased kinetics tends to increase the flame speed. Moreover, an interesting correlation between the flammability limits and the throat velocities were noticed. While both the flashback and blowout limits were observed to shift towards the leaner side with increasing throat velocities, blowout limits tend to reach an asymptote at higher velocities. Increased turbulence level at higher velocities augments the flame front area resulting in higher flame speeds, which conforms with the findings. However, blowout limits are characterized by higher Reynolds numbers and it seems that the turbulence effect reaches an asymptotic value for throat velocities higher than *5.2 m/s*. Further, flame shapes were found to be affected by hydrogen fraction as well as equivalence ratios. Higher *HF* burning is characterized by compact and noisy flames due to increased flame speed. Equivalence ratio has a significant impact on *AFT* and flame shape. The effect of throat velocities on the flame shape was found to be prominent for $\phi < 0.80$, suggesting the flame speed to be a weaker function of turbulent intensity near stoichiometric combustion.

CHAPTER 6

NUMERICAL INVESTIGATIONS OF HYDROGEN-ENRICHED FLAMES

The present study aims at the numerical investigations on the operability limits and flame characteristics of hydrogen-enriched methane combustion in O_2/CO_2 oxidizer in a model gas turbine combustor. The study contributes to the understanding of static stability and flame behavior over wide ranges of hydrogen blends in the fuel stream, equivalence ratio, and throat inlet velocity in a premixed swirl-stabilized model gas turbine combustor.

6.1 Mathematical Model Setup

6.1.1 Conservation Equations

In the present mathematical model, the conservation equations for mass, momentum, energy, and transport equation for scalar variables were solved numerically in the full three-dimensional (*3-D*) domain of the combustor using large eddy simulation (*LES*) model. The three-dimensional and elliptic equations were solved simultaneously to predict the flow regime, heat transfer, and emission characteristics of the hydrogen-enriched oxy- methane flames in the model gas turbine reactor. The governing equations for the conservation of mass, momentum, energy, and species transport can be found from the work by Chen and Ghoniem [19] based on the general conservation equation:

$$\frac{\partial}{\partial x_j}\left(\overline{\rho}\overline{U}_j\Phi+\overline{\rho}\overline{u_j\phi}\right)=\frac{\partial}{\partial x_j}\left[\Gamma_\phi\frac{\partial\Phi}{\partial x_j}\right]+\rho\overline{S}_\Phi \tag{58}$$

Where, Φ and ϕ are the Reynolds averaged and fluctuating components of the dependent variable, u_j is the velocity component in j direction, Γ_ϕ is the diffusion coefficient and S_Φ is the source term.

6.1.2 Radiation Model

The radiative heat transfer equation was solved using the discrete ordinate (*DO*) model with one radiative iteration per five energy iteration. *DO* model is valid for a wide range of optical thickness and is suggested for oxy-fuel combustion modeling [114]. The absorption coefficient of the gaseous mixture was calculated using weighted sum of gray gas model (*WSGGM*) which has been verified over a wide range of operating conditions [115,116].

6.1.3 Turbulence Model

The turbulence in the flow can be categorized into large eddies, typically of the scale of the characteristic length of the mean flow, and small eddies, which are responsible for the dissipation of turbulence kinetic energy. Large eddy simulation (*LES*) model was employed to solve the turbulence by filtering out the small eddies. Low-pass filtering operation for a quantity φ can be obtained using equation [104]:

$$\overline{\varphi}(x,t)=\int G(r,x)\varphi(x-r,t)dr \tag{59}$$

Where the integration is done over the entire domain and G is the filter function that determines the scale of the resolved eddies. Using filtering function, continuity and Navier-Stokes equations yield the following forms:

$$\frac{\partial \rho}{\partial t}+\frac{\partial}{\partial x_i}\left(\rho \bar{u}_i\right)=0 \tag{60}$$

$$\frac{\partial}{\partial t}\left(\rho \bar{u}_i\right)+\frac{\partial}{\partial x_j}\left(\rho \bar{u}_i \bar{u}_j\right)=\frac{\partial}{\partial x_j}\left(\mu \frac{\partial \sigma_{ij}}{\partial x_j}\right)-\frac{\partial \bar{p}}{\partial x_i}-\frac{\partial \tau_{ij}}{\partial x_j} \tag{61}$$

Where, σ_{ij} is the stress tensor due to molecular viscosity, and is given by:

$$\sigma_{ij} \equiv\left[\mu\left(\frac{\partial \bar{u}_i}{\partial x_j}+\frac{\partial \bar{u}_j}{\partial x_i}\right)\right]-\frac{2}{3} \mu \frac{\partial \bar{u}_l}{\partial x_l} \delta_{ij}, \tag{62}$$

and τ_{ij} is the subgrid-scale stress given by:

$$\tau_{ij} \equiv \rho \overline{u_i u_j}-\rho \bar{u}_i \bar{u}_j \tag{63}$$

The sub-grid-scale stresses resulting from the filtering operation has to be modeled. Isotropic part of the subgrid-scale stress is merged with the filtered static pressure term and the deviator part is modeled using turbulent viscosity as:

$$\tau_{ij}=-2 \mu_t \bar{S}_{ij} \tag{64}$$

Where μ_t is the turbulent viscosity and $\overline{S}_{ij}$ is the rate of strain tensor. The turbulent viscosity was solved using Wall-Adapting Local Eddy-viscosity (*WALE*) model given by [105]:

$$\mu_t = \rho L_s^2 \frac{\left(S_{ij}^d S_{ij}^d\right)^{3/2}}{\left(\overline{S}_{ij}\overline{S}_{ij}\right)^{5/2} + \left(S_{ij}^d S_{ij}^d\right)^{5/4}} \qquad (65)$$

Where, L_s (the mixing length for sub-grid-scale) and S_{ij}^d are given by:

$$L_s = \min\left(\kappa d, C_w V^{1/3}\right)$$

$$S_{ij}^d = \frac{1}{2}\left(\overline{g}_{ij}^2 \overline{g}_{ji}^2\right) - \frac{1}{3}\delta_{ij}\overline{g}_{kk}^2, \quad \overline{g}_{ij} = \frac{\partial \overline{u}_i}{\partial x_j}$$

Where, κ is the von Karman constant, d is the distance to the closest wall, C_w is the WALE constant, and V is the volume of the computational cell.

6.1.4 Reaction Kinetics Model

The oxy-combustion of hydrogen-enriched methane was solved using the partially premixed combustion model that is modified to address the fully premixed combustion case. The transport equations of the mean reaction progress variable $\bar{c}$, the mean mixture fraction $\overline{f}$, and the mixture fraction variance $\overline{f'^2}$ were solved to obtain the other scalar variables. The mixture fraction (f) is defined as [117]:

$$f = \frac{sY_{fu} - Y_{ox} + Y_{ox,0}}{sY_{fu,1} + Y_{ox,0}} \tag{66}$$

Where, s is the oxygen to fuel ratio and Y is the mass fraction. Y_{ox} and Y_{fu} represents the mass fractions of oxidizer and fuel, respectively, while, the subscripts 0 and 1 refer to the inlet streams of oxidizer and fuel, respectively. The density weighted average scalars such suitable species in the gaseous mixture such that it assumes a value of zero in the unburnt mixture and a value of 1.0 in the burnt gas mixture.

The temperature and species fractions can be calculated from the probability density function [$p(f)$] of mixture fraction (f) and mean progress variable ($\bar{c}$) from the following equation:

$$\bar{\phi} = \bar{c}\int_0^1 \phi_b(f)\,p(f)df + (1-\bar{c})\int_0^1 \phi_u(f)\,p(f)df \tag{67}$$

Where, u and b represent the burnt and unburnt mixtures, respectively.

The premixed combustion can be considered to be governed by a thin reactive sheet, which propagates from the burnt products towards the unburnt gases. Progress variable (c) is defined on the basis of the mass fractions of the species as:

$$c = \left(\frac{\sum_{i=1}^{n} Y_i}{\sum_{i=1}^{n} Y_{i,ad}} \right) \tag{68}$$

where, Y_i represents the mass fraction of product species *i*, and the sub-script *ad* represents the species after complete combustion. Hence, the value of $c = 0$ and $c = 1$ mean the unburnt and burnt mixture, respectively. Laminar flame speeds for different compositions of H_2/CH_4 mixture were taken from the literature [81] and a user defined function (*UDF*) was incorporated to calculate the flame speed at various mixture fractions.

The propagation speed of the flame can be modeled by solving the transport equation for the mean reaction progress variable ($\bar{c}$) as [118]:

$$\frac{\partial}{\partial t}(\rho c)+\nabla\cdot\left(\rho\vec{v}c\right)=\nabla\cdot\left(\frac{\mu_t}{Sc_t}\nabla c\right)+\rho Sc \qquad (69)$$

Where Sc_t is the turbulent Schmidt number and Sc is the reaction progress source term aslo known as product formation rate. The reaction source term (Sc) was modeled using Zimont's turbulent flame closure (*TFC*) given as:

$$\rho Sc=\rho_u S_T\left|\nabla c\right| \qquad (70)$$

Where ρ_u is the density of the unburnt mixture and S_T is the turbulent flame speed.

6.2 Reactor Design and Boundary Conditions

An axisymmetric quadrant of the reactor geometry was modeled as presented in *Figure 37*. The criterion for the optimum mesh refinement was evaluated based on the integral length scale (l_0), where the filter width (Δ) should satisfy the condition [119]:

$$\Delta\le\beta l_0 \qquad (71)$$

Where, the integral length scale (l_0) was approximated using turbulent kinetic energy (k) and turbulent dissipation rate (ε) as:

$$l_0=\frac{k^{3/2}}{\varepsilon} \qquad (72)$$

The value of $\beta\le0.2$ was selected to resolve more than *80%* of the turbulent kinetic energy. The mesh refinement was conducted a priori using RANS model. After the mesh refinement check, a mesh of around *40,000* finite volume cells, having finer meshing in the near burner region and coarser meshing in the near outlet zone of the combustor, was selected to perform the present numerical study. Temporal resolution was determined using CFL (Courant-Friedrichs-Lewy) criterion, to ensure the numerical stability of the model, using the following correlation:

$$\frac{u\Delta t}{\Delta x} \leq C_{\max} \tag{73}$$

Where, $C_{\max} = 1$, $u = 15\,m/s$ and $\Delta x = 0.19\,mm$. The time step for the calculation is calculated to be *12µs*. A conservative value of *5µs* was chosen to account for the flow acceleration and chemical time scale.

To analyse the effect of nozzle geometry on the swirl of the flow, a cold flow analysis was conducted. Figure 38 shows the velocity vector along the nozzle of the reactor inlet. It can be seen that the tangential component of the velocity gets weaker as the flow proceeds towards the throat. The effect is even clearer through Figure 39, which depicts the velocity ratio (tangential velocity/axial velocity) at the inlet and throat of the nozzle. However, the current study ignores this effect and the reactor quadrant was created without the convergent part of the nozzle.

A particular composition of the fuel and the oxidizer mixture stream was injected through the inlet of the combustor with a constant throat velocity. Axial and tangential components of the flow were set to induce a swirl flow with the swirl number of *0.98*. To take account of the transient behavior of the high turbulent flow, fluctuating velocity was solved using vortex method algorithm. Mean mixture fraction of the inlet stream was calculated according to the composition and equivalence ratio of the inlet stream and was set under the inlet stream of the partially premixed model. The combustor wall was assigned mixed thermal boundary condition with a convective heat transfer coefficient of $20\ W/m^2K$ [120], and free stream temperature and external radiation temperature of *300 K* each. The wall thickness (*6 mm*) was set to semi-transparent boundary type. Non-grey band model with *4* wavelength bands was used to calculate the radiation heat transfer through the quartz tube. Both the symmetry faces of the quadrant were assigned periodic boundary conditions to take care of the tangential components of the swirling flow in the numerical calculations.

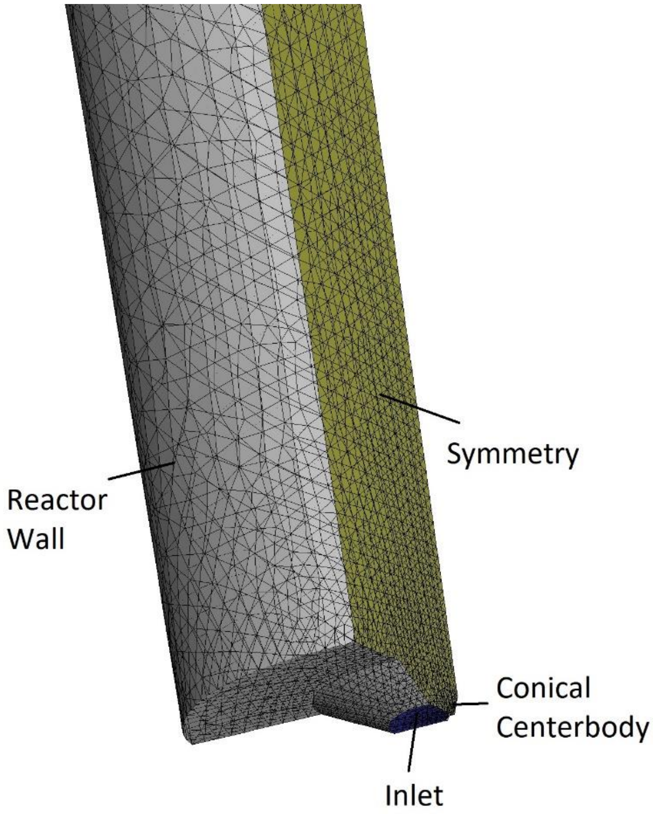

Figure 37. Schematic of the combustor quadrant mesh used for the numerical simulations.

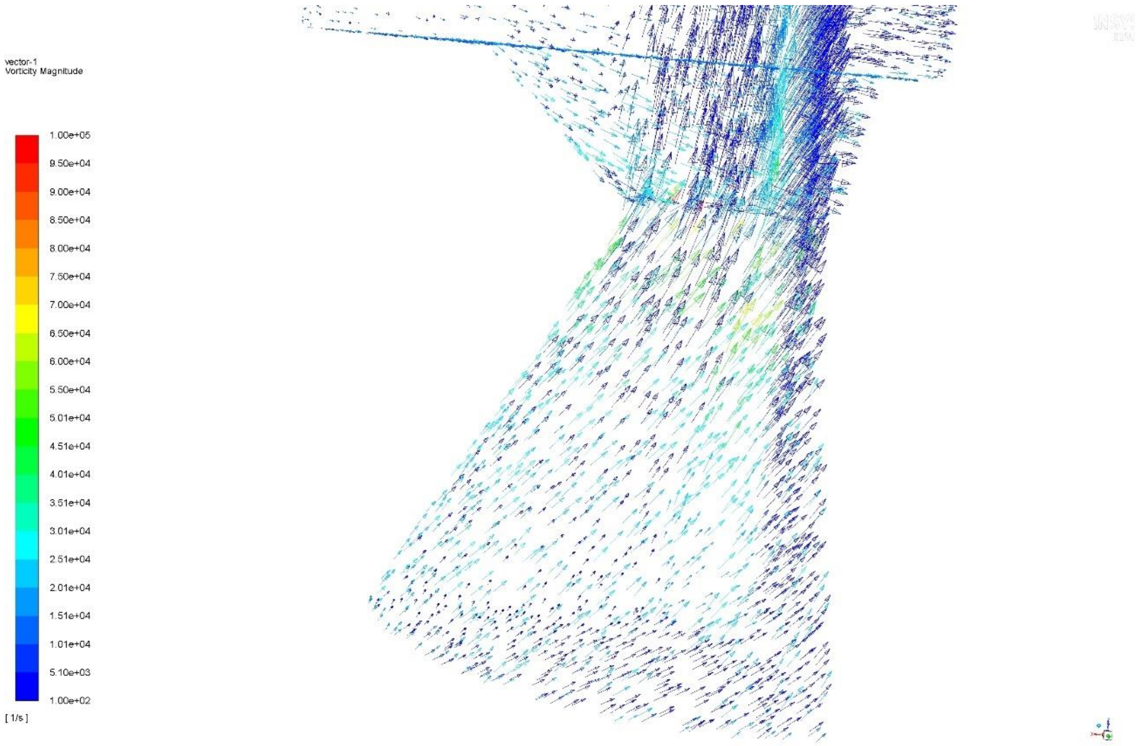

Figure 38. Velocity vector in the convergent-divergent nozzle of the reactor.

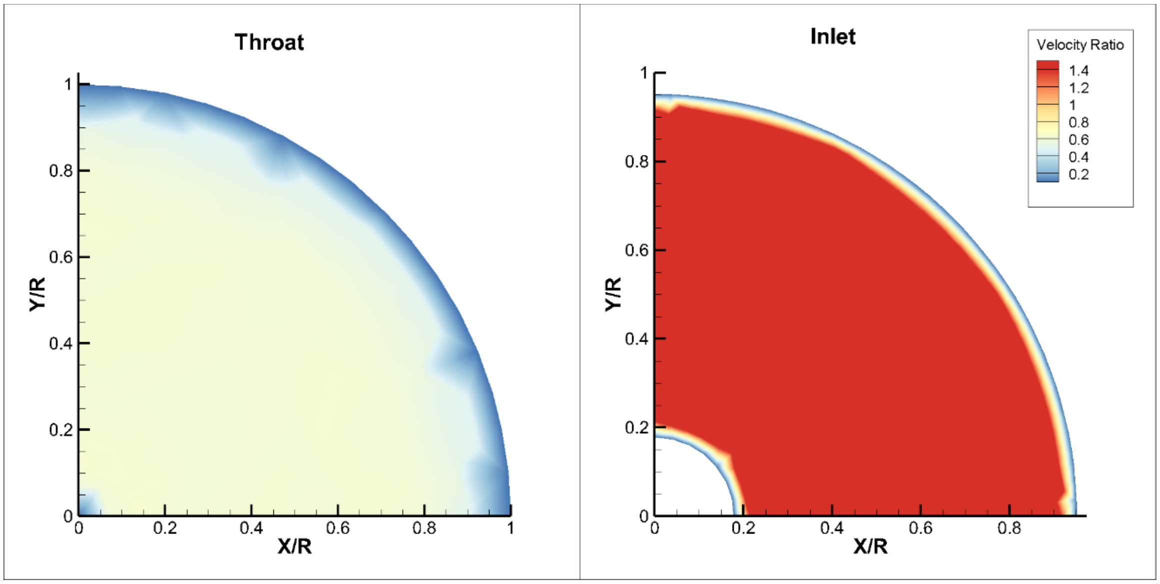

Figure 39. Velocity ratio (tangential/axial) at the throat and inlet of the convergent-divergent nozzle.

To study the effect of flame stretching, critical rate of strain (g_{cr}) is calculated using the equation [118]:

$$g_{cr} = \frac{BS_L}{\alpha} \tag{74}$$

Where, B is a constant, S_L is the laminar flame speed and α is the unburnt thermal diffusivity of the reactant mixture. Critical rate of strain (g_{cr}) is the value of shear strain rate which will quench the flame.

Flame thickness (δ) has been estimated using the following correlation [104]:

$$\delta = \frac{\lambda_u}{\rho_u c_p S_L} \tag{75}$$

Where, λ_u and ρ_u are the unburnt thermal conductivity and density, respectively.

A non-dimensional ratio of reaction rate to diffusion rate, known as Damkohler number (Da), is given as [104]:

$$Da = \frac{\left(l_t / u' \right)}{\left(\delta / S_L \right)} \tag{76}$$

Where, l_t is the integral length scale and u' is the RMS of velocity fluctuation.

Karlovitz number (Ka) is defined for the smallest eddies and represents the ratio of the chemical time scale to the Kolmogorov time (for the smallest eddies) given as [104]:

$$Ka = \frac{\sqrt{\varepsilon / \nu}}{S_L / \delta} \tag{77}$$

Where, ε is the turbulent dissipation rate and ν is the kinematic viscosity.

The source term (*Sc*) in the transport equation of the progress variable is defined as the product formation rate (*PFR*) which represents the magnitude of the reaction rate.

6.3 Results and Discussions

The numerical model developed, considers only the combustor part and does not model the mixing chamber of the rig (Figure 22), where the oxidizer and fuel mixes. However, to ensure proper mixing of the reacting gases, a separate cold flow analysis of the mixing chamber was conducted. Figure 40 presents the radial profile of the mass fraction of CH_4 at various heights from the bottom of the rig. It can be seen that the mass fraction distribution of CH_4 along the radial direction gets uniform at the height of $Z/D=10$ from the rig bottom. The fact that the mixing plenum length is around $Z/D=20$, it is ensured that the reacting gases entering the combustion domain are well premixed.

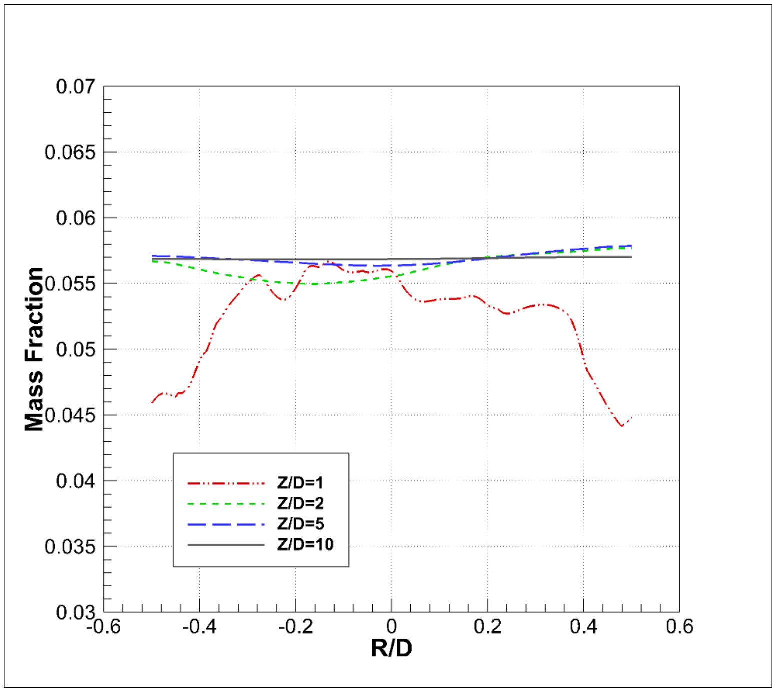

Figure 40. Mass fraction of CH_4 at various heights from the bottom of the mixing plenum.

6.3.1 Effect of Hydrogen Enrichment

The behavior of hydrogen-enriched premixed flames was studied over a range of fuel blends in the model gas turbine combustor. The flame stability was mapped based on the experimental measurements by identifying the flame lean blowout *(LBO)* limits and flashback limits over ranges of hydrogen fraction and equivalence ratio at a fixed throat inlet velocity of *5.2 m/s* to provide a constant volumetric flow rate of the reactant mixture.

Figure 41 presents a comparison of the experimentally recorded and numerically calculated values of temperature along the central axis of the reactor at an equivalence ratio of *1.0* over a range of *HF*. To take into account for the radiative and conductive heat losses through the thermocouple during temperature measurement, temperature correction was applied. Corrected temperature of the burnt gases can be determined by balancing the heat transfer using following equation:

$$T_c = T_m + \frac{\varepsilon_j \sigma}{h}\left(T_m^4 - T_s^4\right) + \frac{k_w A_w \left(T_m - T_s\right)}{h A_j l} \qquad (78)$$

Where, T_c is the corrected temperature, T_m is the measured temperature, T_s is the surrounding temperature, ε_j is the emissivity of the junction, k_w is the thermal conductivity of the thermocouple wire, A_w is the cross-section area of the junction, A_j is the surface area of the junction, l is the length of the thermocouple wire and h is the convective heat transfer coefficient estimated by:

$$Nu = \frac{h d_j}{k_g} = \left(0.44 \pm 0.06\right) \mathrm{Re}_j^{0.5} \qquad (79)$$

Where, d_j is the junction diameter and k_g is the thermal conductivity of the gaseous mixture. Junction emissivity can be calculated using following correlation [120]:

$$\varepsilon_j = 9 \times 10^{-4} T + 0.3324 \qquad (80)$$

The difference between the numerical and experimental temperature values near the burner region was observed to be as high as 400 ^{o}C. This can be attributed to the experimental error due to the positioning of the probe in high temperature gradient region. Moreover, thermocouples have limitations at high temperature measurements and implementation of laser diagnostic technology would be beneficial for better accuracy. The temperature levels were found to increase slightly with increasing hydrogen fraction in the fuel blend. This may be attributed to (a) the increased fuel diffusion and reactivity and (b) the slightly higher adiabatic flame temperature with the increased HF. The axial temperature levels decrease gradually downstream of the burner after a height of around Z/D=1.0, i.e. downstream of the flame core. Due to the limited operating range of the thermocouple, we were not able to measure the temperature within the flame core, i.e. in the zone of Z/D<1.0. However, the values of temperature within the flame core were calculated numerically as shown in *Figure 41*. Although the flames are stabilized at both the inner and outer shear layers, the temperature profile reveals nearly constant temperature level within $0.2<Z/D<1.0$. This can be attributed to the creation of an inner recirculation zone *(IRZ),* which transfers the convective heat to the region. The radial temperature profiles, at the height of $Z/D=0.92$ from the burner, are presented in *Figure 42*. The differences in flame temperature were only marginal for the different hydrogen fractions. For all *HFs,* the temperature increases radially from the center of the combustor, where the *IRZ* is located, towards the zone near the combustor wall where the *ORZ* is located, passing across the main flame core. The temperature decreases near the combustor wall due to the effect of the *ORZ* and heat loss through the wall.

When comparing the measured and calculated temperature values as presented in *Figure 41* and *Figure 42*, one can see that the numerical model slightly overpredicts the temperature within the combustor. This may be attributed to the cooling effect of the burner port, which quenches the reaction in the very near zone to the burner port causing a slight reduction of the combustion temperature [121]. This quenching effect of the burner wall was not addressed in the computational model causing such slight differences between the experimentally recorded and the numerically predicted temperature values. The quenching effect of the burner wall is clearly identifiable in the experimental flame images (*Figure 43*) by a dark zone beside the burner wall and below the flame base. In this Figure, the experimentally captured flame images are compared with the numerically calculated flame shape presented by the center-plane contours of the OH radicals within the flame core. No reactions occur within the *ORZ* and the narrow zone beside the burner wall due to the wall cooling effect, which causes local quenching. At lower hydrogen fraction (*HF=10%*), the flame is spread out taking the shape of the confinement as presented in *Figure 43*. However, the flames with higher hydrogen fractions are characterized by more violent and compact shape indicating better reactivity of the fuel mixture.

Profiles of axial velocity components along the central axis of the combustor for different hydrogen fractions are plotted in Figure 45. The regions of negative axial velocities are apparent in the figure depicting the recirculation regions in the combustor. Figure 46 and Figure 47 shows the contours of axial and tangential velocity components at various heights from the inlet of the combustor for the hydrogen fraction of 50%. Both the axial and tangential velocities diminish with the reactor height, however, the swirl can be observed until the exit of the reactor.

The center-plane contours of velocity flow-field are plotted over the temperature contours in *Figure 44* for different hydrogen fractions. The flow is characterized by the creation of both *IRZ* and *ORZ*. At lower *HFs*, below *20%*, the *IRZ* is characterized with one main large eddy spinning in the counter-clockwise direction. Increasing *HF* to *30%* resulted in breakdown of the *IRZ* into two eddies: the larger primary eddy (*PE*) moved a little downstream, and a smaller secondary eddy (*SE*) was created upstream and spins in an opposite direction to the *PE*. Increasing *HF* to *50%* resulted in further breakdown of the

IRZ, with two *SE* spinning opposite to each other, in addition to the *PE*. The size and number of *SEs* are mainly controlled by the hydrogen fraction. This indicates better turbulence-reactions interaction within the flame with hydrogen enrichment at fixed equivalence ratio. Actually, at higher *HF* operation, the flame becomes more compact and well anchored to the burner inlet (see *Figure 43*) due to the increased burning velocity. Moreover, the experimental observations at higher hydrogen fractions are characterized by high audible sound, conforming with the numerical results predicting an increase in the vorticity causing more intense and violent flames. The creation of an *ORZ* is also observed at the bottom end of the combustor beside the combustor wall. The size of the *IRZ* gets bigger and occupy a larger zone at higher *HFs*; however, the size of the *ORZ* does not affect significantly by the *HF*. This may be attributed to the high aspect ratio between the diameter of the combustor and the burner throat diameter.

The contours of vorticity magnitude and static temperature are presented in *Figure 48*. As shown in the figure, the flame is stabilized where reactions take place between the inner and outer shear layers. The length of the inner shear layer increases with hydrogen addition due to enhanced vorticity levels near the central axis. The temperature within the flame core approaches *2000 °C*, then reaches moderate values at the combustor exit that are suitable for turbine blade operation; see *Figure 41* as well. The obtained temperature distributions indicate better combustion and emission characteristics of such kind of premixed oxy-methane flames with hydrogen enrichment. *Figure 49* presents the variations of the predicted and the critical rate of strain with the hydrogen fraction. The rate of strain presented in the figure is the average value calculated on the iso-surfaces of $c=0.1$ and $c=0.9$. The critical rate of stain increases significantly from $\sim 4300\ s^{-1}$ for pure methane combustion to ~*9700* s^{-1} at *50% HF*. However, the rate of strain increases only slightly with hydrogen addition, indicating a wider stability range against *LBO*, as is evident from the experimental findings discussed earlier. Thus, hydrogen blending stabilizes the flames for higher strain rates before they quench and extinguish.

Figure 50 shows temperature contours plotted on the x-z plane at different time steps and Figure 51 presents the temperature contour plotted on the iso-surface of progress variable = 0.9 at different time steps. The iso-surface of progress variable = 0.9 represents that 90% of the reactants has converted into the products. Small time intervals are presented here due to the limitation of calculation time for these computationally intensive simulations. The figures show the transient nature of the turbulent flame, however, there is not significant variation in the flame shape. This is the characteristics of low Karlovitz number flames where flame shapes are affected only marginally due to the turbulence.

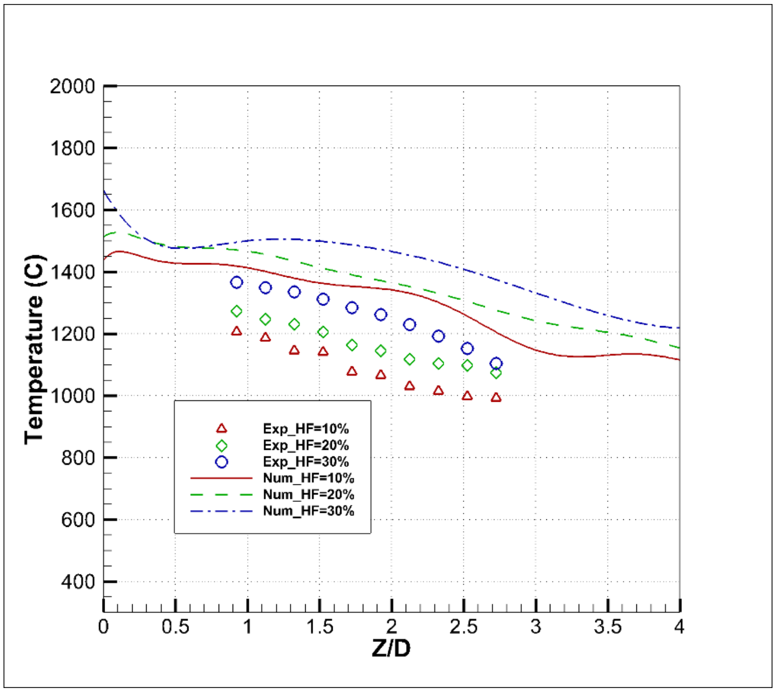

Figure 41. Experimental versus numerical temperature profile along the axis of the combustor.

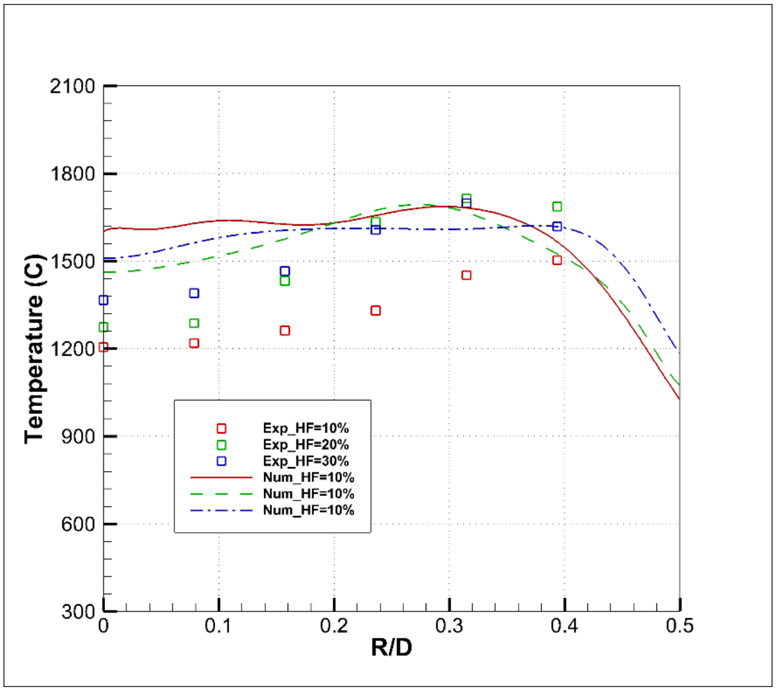

Figure 42. Experimental versus numerical temperature profile along the radial direction at the height of Z/D=0.92.

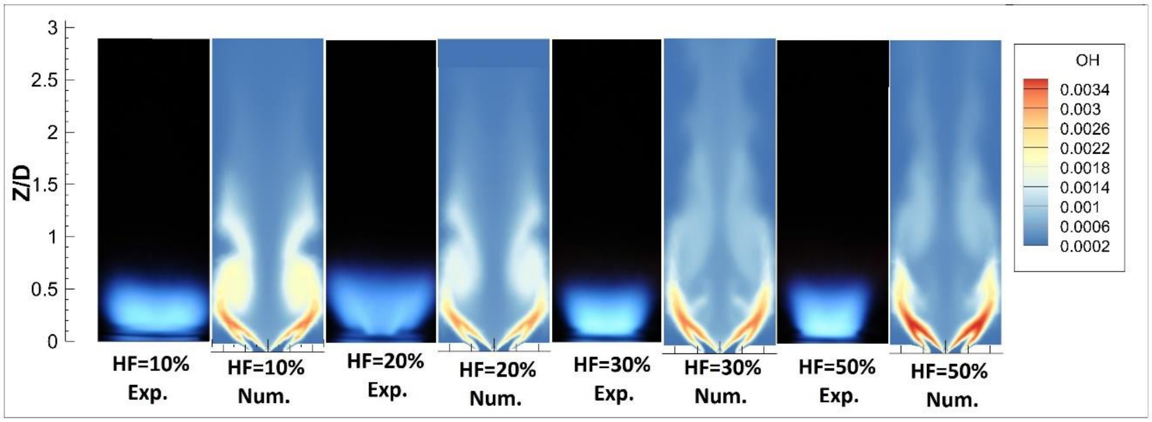

Figure 43. Comparison between experimental (photos taken by a high-speed camera) and numerical (based on OH contour plots) flame shapes at different hydrogen fractions.

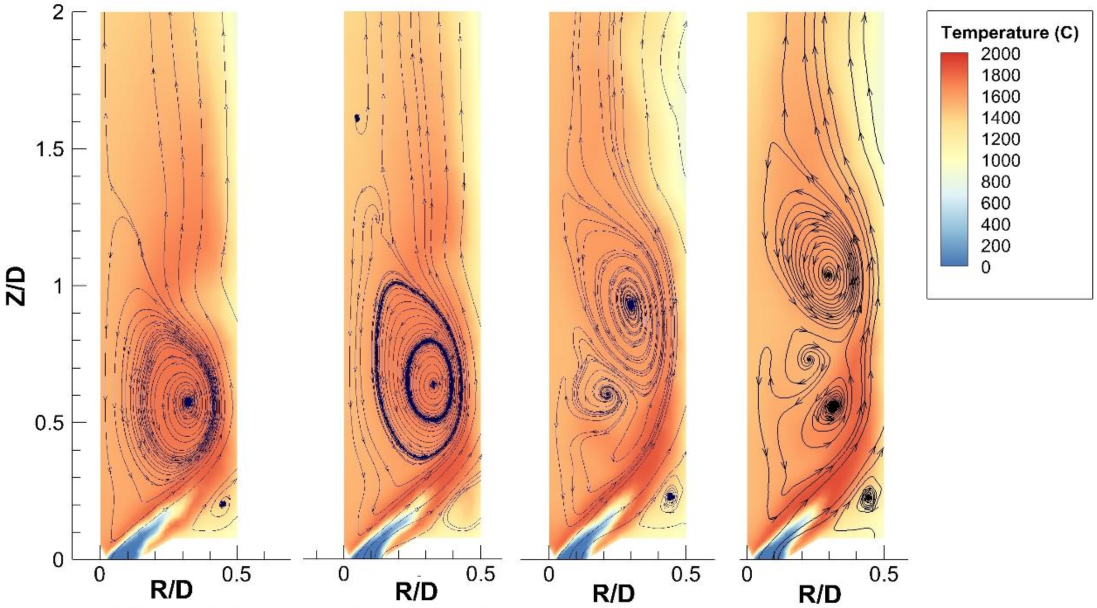

HF = 10% HF = 20% HF = 30% HF = 50%

Figure 44. Velocity flow-field mapped over temperature contour at different hydrogen fractions.

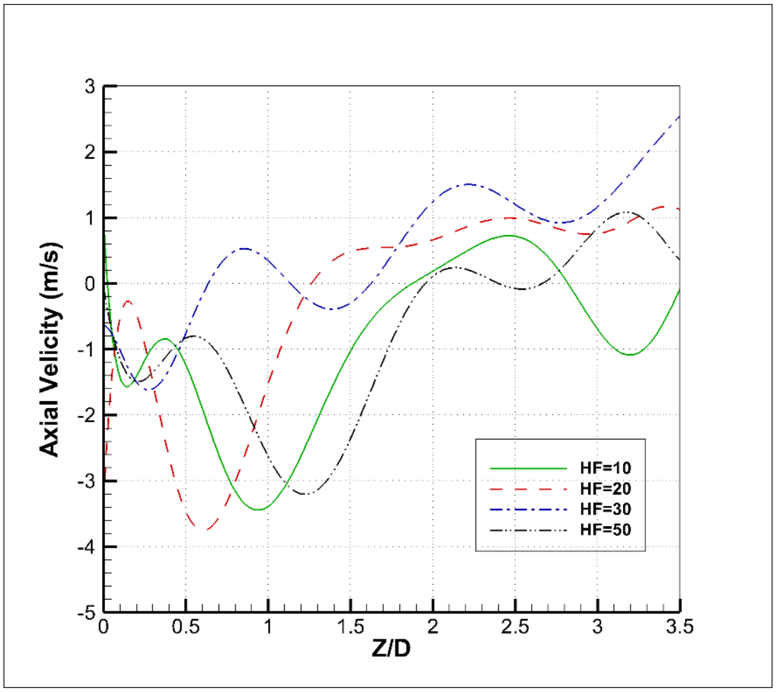

Figure 45. Axial velocity profile along the central axis of the combustor.

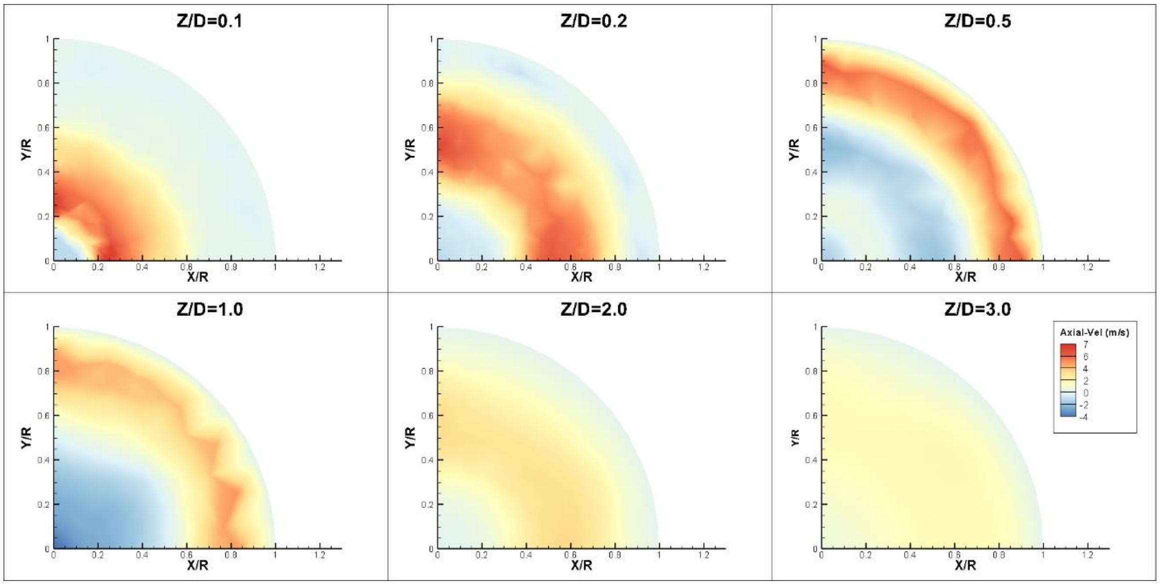

Figure 46. Axial velocity component contours at various heights of the combustor for *HF=50%*.

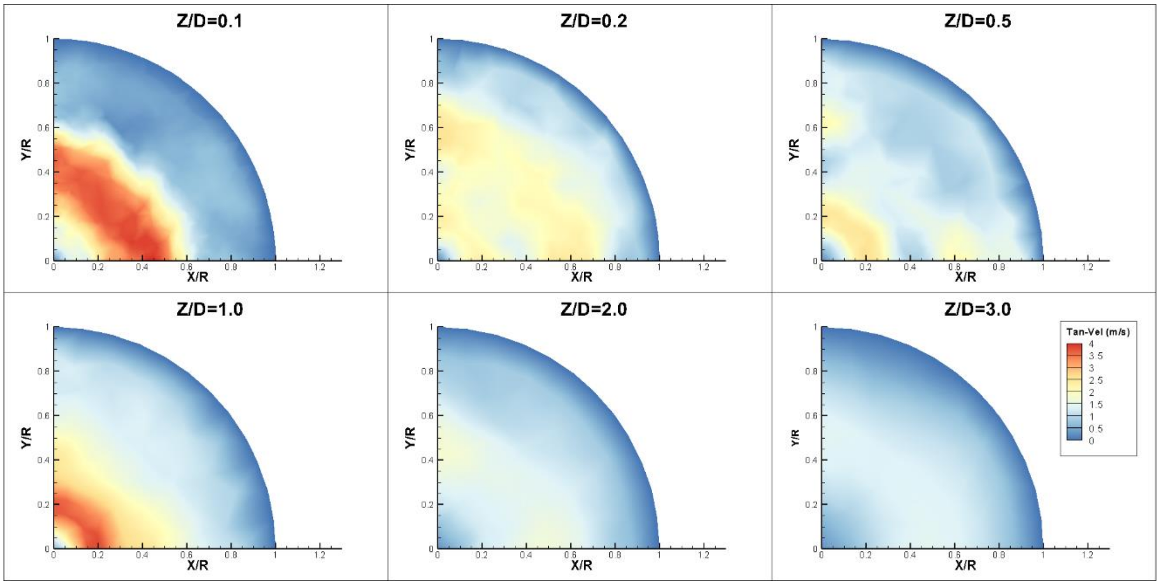

Figure 47. Tangential velocity component contours at various heights of the combustor for *HF=50%*.

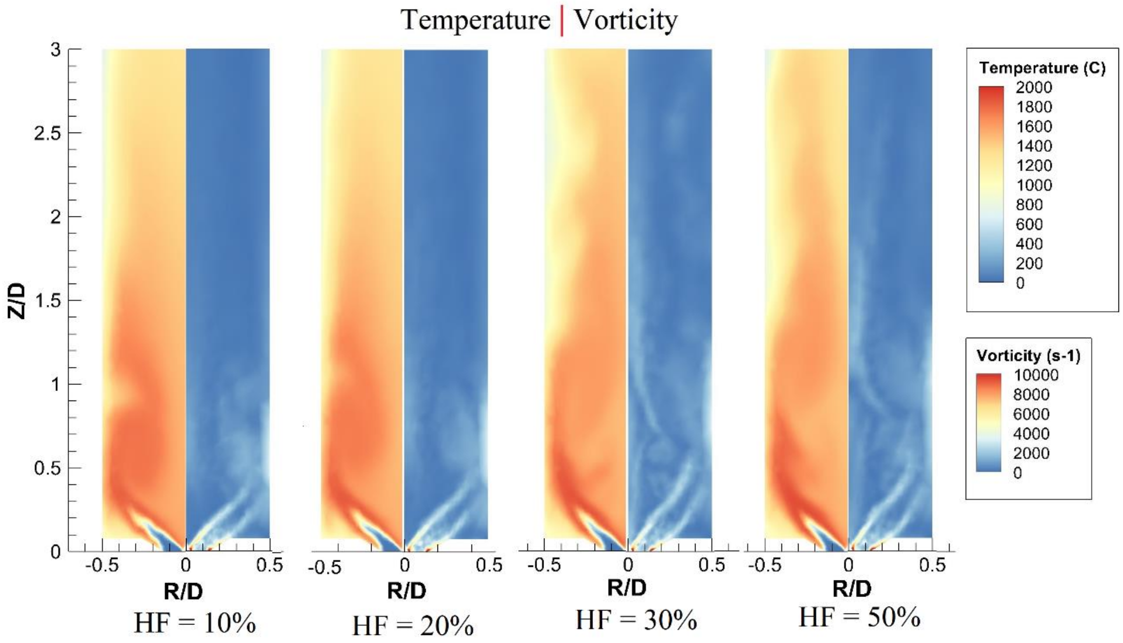

Figure 48. Contours of temperature (left) and vorticity (right) for various hydrogen fractions.

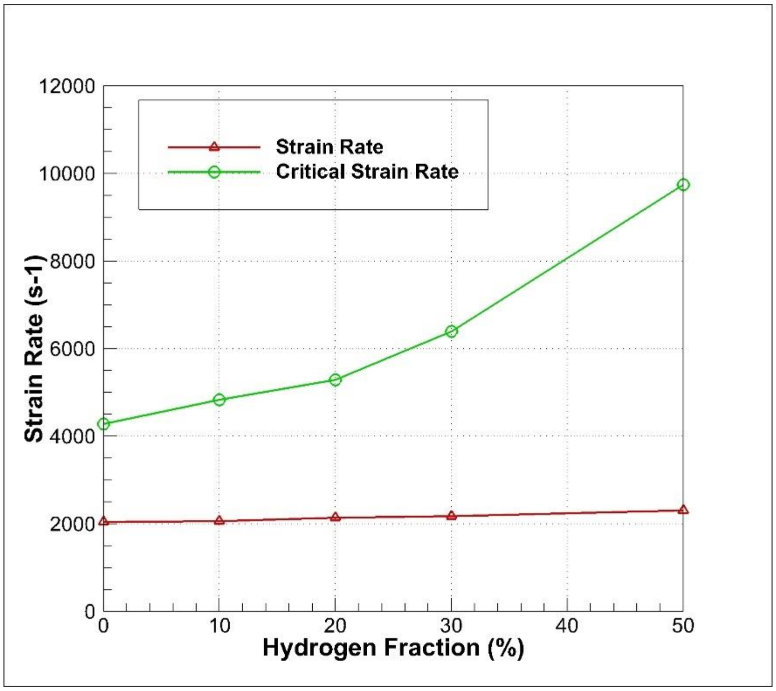

Figure 49. Variation of critical rate of strain and predicted strain rate at various hydrogen fraction.

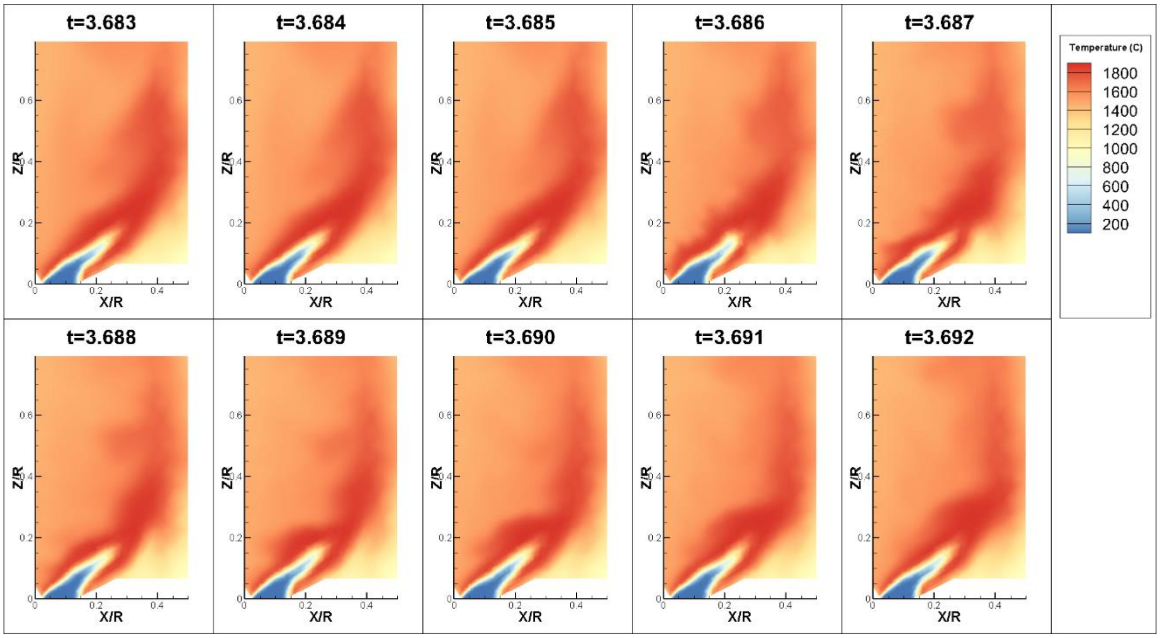

Figure 50. Temperature contour at different time steps (*3.683-3.692 secs*) for *HF=50%*.

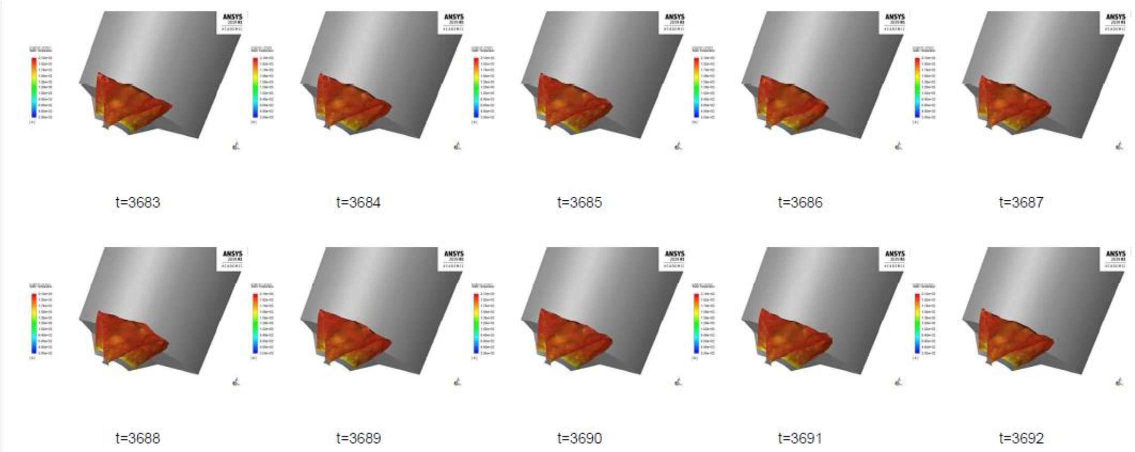

Figure 51. Temperature plotted at iso-surface of progress variable = 0.9 at different time steps (*3.683-3.692 secs*) for *HF=50%*.

Figure 52 shows the contours of the product formation rate and progress variable near the burner region for different hydrogen fractions. It is observed that the reaction zone exists between the inner and the outer shear layers, and the flame is stabilized in both layers. At higher hydrogen fractions, the rate of product formation increases in the thinner inner shear layer, indicating more intense and compact flames. At lower hydrogen fractions, the *PFR* decreases in the inner shear layer, and the flame thus tends to stabilize towards the corner of the combustor. Although the numerical model is incapable of capturing the switch from *ORZ* to *IRZ* stabilization, the switch is inferred from the trend of *PFR*. Recall that corner stabilization was observed experimentally at *10% HF*, as depicted in *Figure 43*. This indicates that the role of *ORZ* in flame stabilization is significant at lower *HFs* and diminishes at higher *HFs.* The model also predicts the shorter and more compact flames at higher hydrogen fractions as is evident from the contours of progress variable which shows the transition from the unburnt mixture to completely burnt products, as presented in *Figure 52*.

For a deeper insight into the flame to see how the reactions are proceeding, the mole fractions of H_2, CH_4, *OH* and *CO* are shown in *Figure 53* for *10%* and *50%* hydrogen fractions. The contours of fuel concentration show longer tails for both H_2 and CH_4 at *10% HF* than at *50% HF*, indicating faster reactions and shorter flame lengths with hydrogen addition. This conclusion is also confirmed by the enhanced *OH* radical formation at higher *50% HF* as presented in the figure. It has been observed that the oxidation of *CO* is retarded with hydrogen addition, which is attributed to the fact that at higher hydrogen concentrations, carbon has to compete with hydrogen for oxygen, resulting in retarded *CO* oxidation. The *CO* emission is increased from *46 ppm* with pure methane combustion to *378 ppm* with *50% HF* as depicted in *Figure 54.*

The effect of hydrogen enrichment on flame thickness (δ) is presented in *Figure 55*. The calculated flame thickness is *47.6 µm* for pure methane, as compared to *35 µm* at *50% HF*. The flame thickness decreases almost linearly with hydrogen fraction as shown in the figure. The Damkohler number (*Da*) and the Karlovitz number (*Ka*) are plotted in *Figure 56* at the different hydrogen fractions. The Damkohler number increases from *1080* for pure methane to *1670* at *50% HF,* indicating significantly faster reactions with hydrogen addition. $Da>>1$ indicates the reaction is much faster and is not affected by the turbulence. Karlovitz number was found to decrease from *0.42* for pure methane to *0.24* at *50% HF*, however, the correlation is not linear. Lower *Ka* value suggests that the chemical time scale is much less than the Kolmogorov time scale, and hence, the flame thickness for CH_4/H_2 oxy-flames are smaller than the smallest turbulent scale. In such flames, the flame front is thin, and the turbulence is not able to alter the inner structure of the flame, but it gets wrinkled due to the turbulence motion. Thus, the reactions are governed by the laminar burning rate.

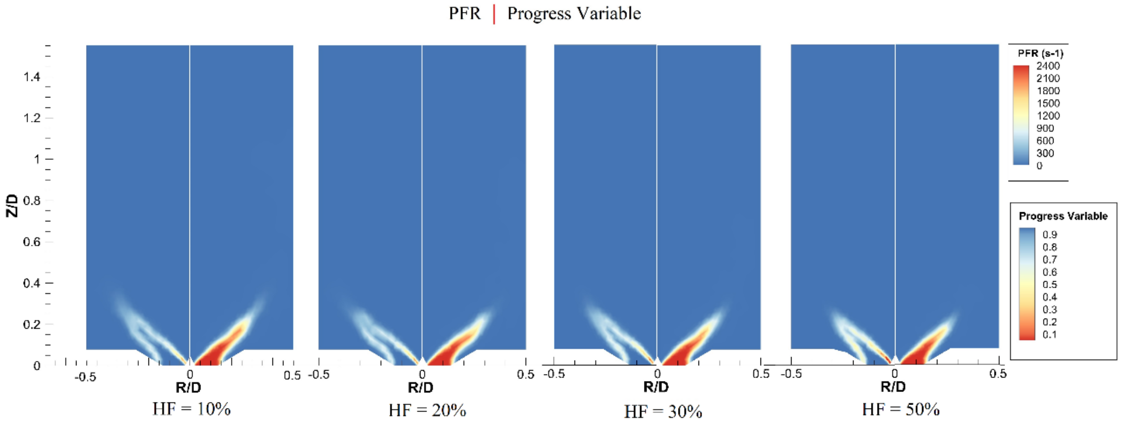

Figure 52. Contours of product formation rate and progress variable at various hydrogen fractions.

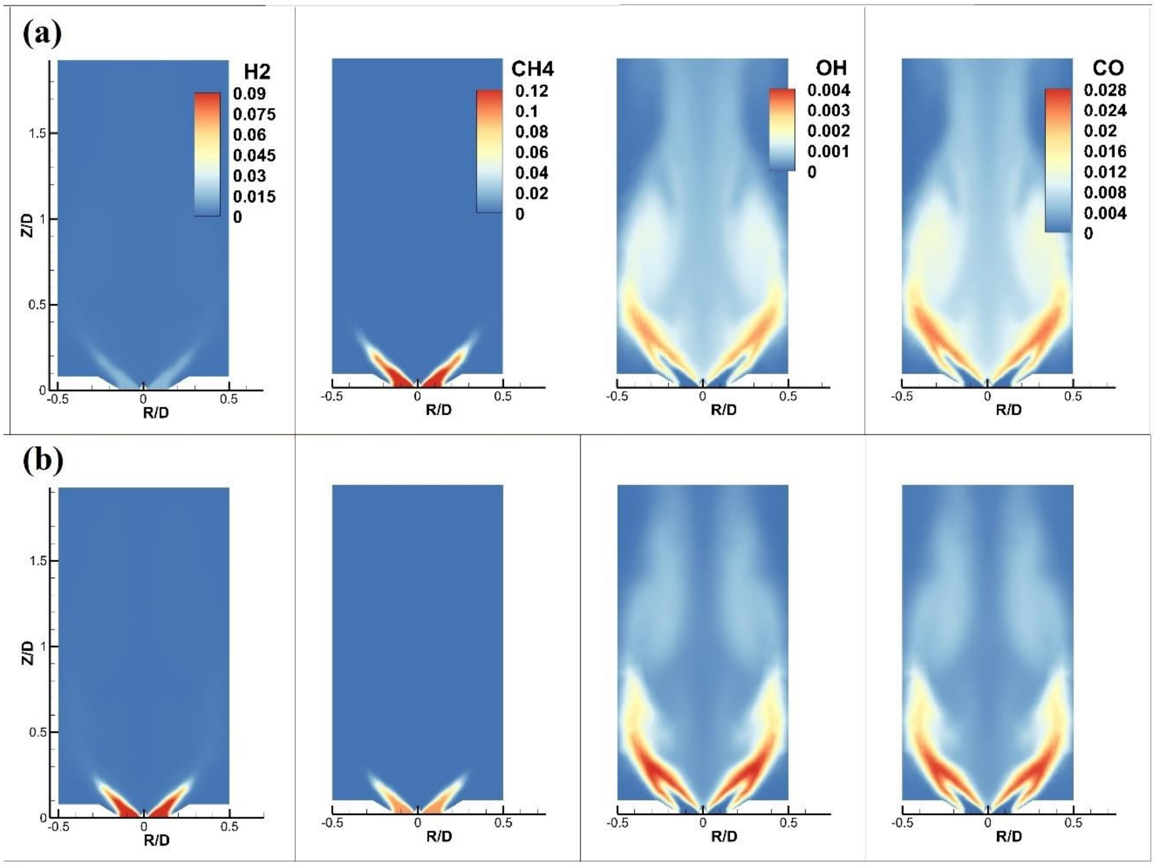

Figure 53. Mole fraction distributions of CH_4, H_2, CO, and OH within the combustor at hydrogen fraction of (a) 10% and (b) 50%.

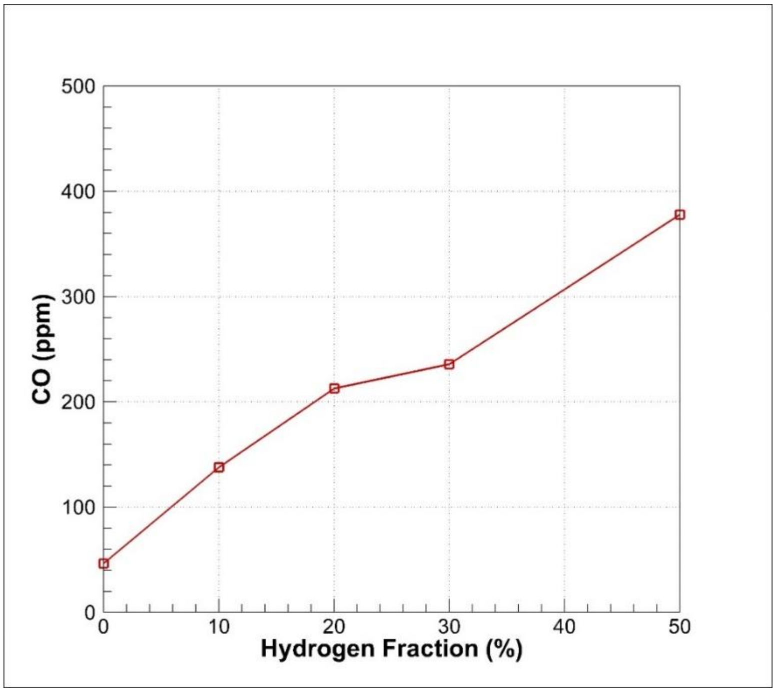

Figure 54. CO emission at the combustor exhaust for various hydrogen fractions.

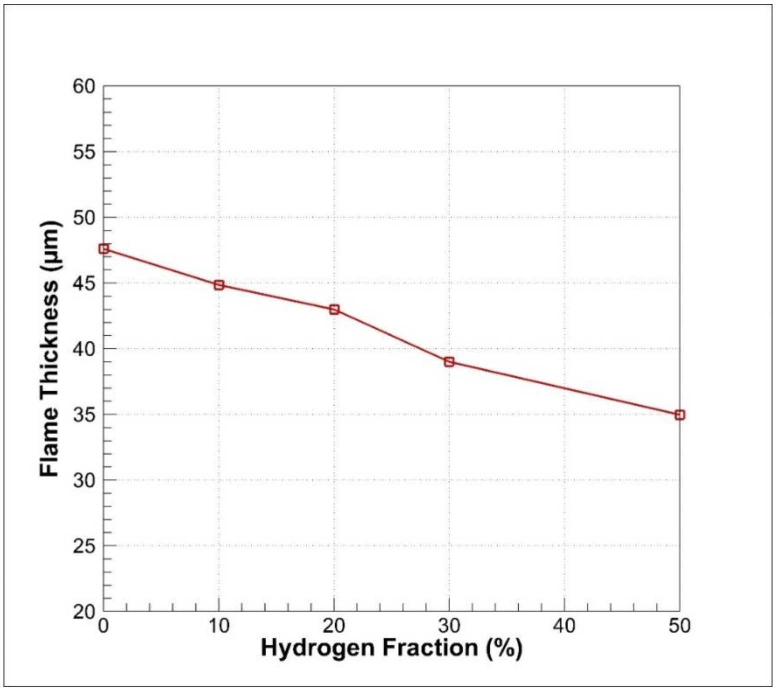

Figure 55. Effect of hydrogen fractions on the flame thickness.

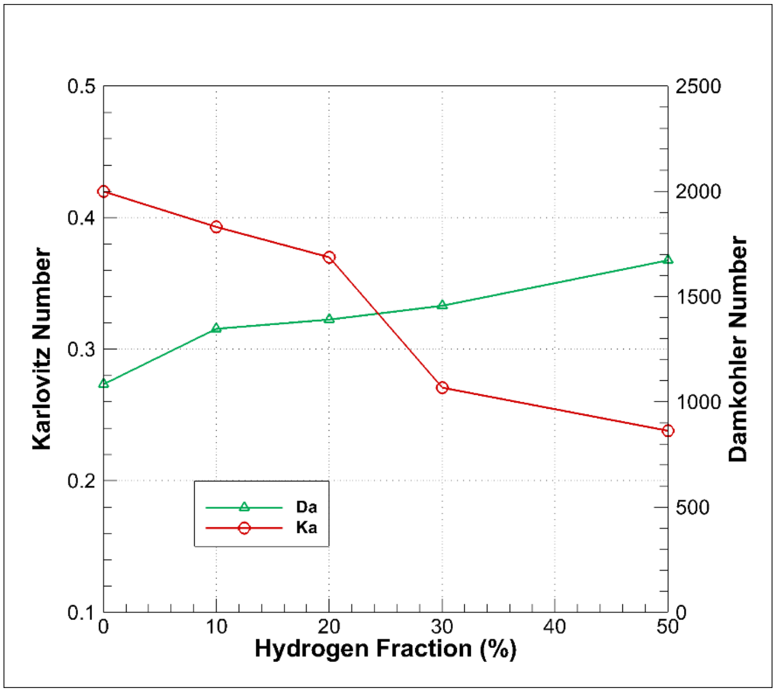

Figure 56. Karlovitz number and Damkohler number variation with hydrogen fraction.

6.3.2 Effect of the Equivalence Ratio

In this section, the effect of equivalence ratios on the flame characteristics and macrostructure has been studied. The hydrogen fraction in the fuel blends was fixed at *50%* and the oxidizer composition was set to *30%* O_2 and *70%* CO_2. Three cases with different equivalence ratios: (i) Stoichiometric (near flashback limit), (ii) $\varphi=0.75$ (intermediate stable combustion) and (iii) $\varphi=0.5$ (near blowout limit) have been considered. Figure 57 shows the comparison of experimental flame images using a high-speed camera with the numerical contours of *OH* mole fractions on the vertical plane passing through the center of the combustor. The numerical model is successful in predicting the flame structure as shown in the figure. At the $\varphi=1$, the flame is compact and intense with bright and violent flame characterized by high *OH* concentration as compared to lower equivalence ratios. The flame has typical *V*-shape stabilized at both the inner shear layer and the outer shear layer as can be seen from Figure 58. As the equivalence ratio is reduced, the flame tends to stabilize at the inner shear layer and a transition is observed at *φ=0.75*. At *φ=0.5*, the flame is stabilized at the inner shear layer, and the flame takes the shape of the confinement, characteristic of the corner stabilized flames. The numerical results show lower *OH* concentrations due to lower temperature and reaction rates. At the lower equivalence ratio, a single large eddy is observed in the *IRZ* without any outer recirculation. As the equivalence ratio is increased (*φ=0.75*), a small outer recirculation starts developing and the flame starts to stabilize at the *OSL* too. Moreover, the center of the large eddy in the *IRZ* shifts downstream away from the burner and a secondary smaller eddy appears rotating in the clockwise direction. With further increase in the equivalence ratio (*φ=1.0),* the larger eddy shifts further downstream of the burner, and two smaller eddies developed in the *IRZ*, rotating in clockwise and counter-clockwise directions, respectively. A well-defined *ORZ* is also observed to appear and the flame is well stabilized between the two shear layers.

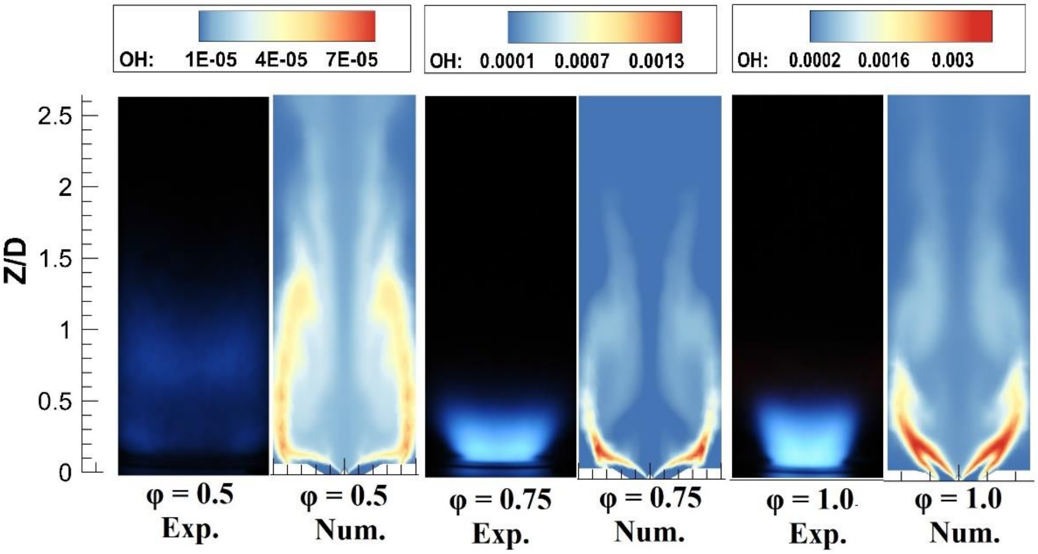

Figure 57. Comparison between experimental (photos taken by a high-speed camera) and numerical (based on *OH* contour plots) flame shapes at different equivalence ratios.

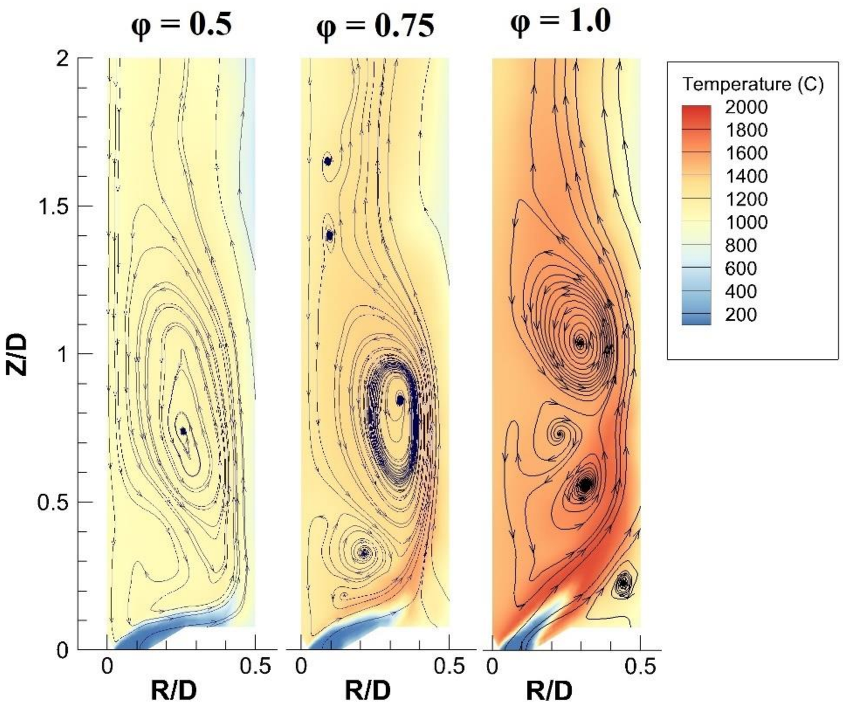

Figure 58. Velocity flow-field mapped over temperature contour at different equivalence ratios.

The axial temperature profiles for all the three cases are shown in Figure 59. The temperature level decreases along the axial direction as the combustion gets leaner. The temperature profiles in the radial direction are plotted at the height of *Z/D=0.1* and *Z/D=0.5* from the burner Figure 60. The peak at the height of *Z/D=0.1* is distinct and closer to the center of the burner at *φ=1.0* and gets diffused and lower as we move towards the leaner regimes. The peaks represent the colder reactive gases jet, surrounded by the burnt hot gases represented by the valleys on both sides. The valley at *φ=0.5* is attached to the wall where the flame is stabilized without any outer recirculations. Whereas, at *φ=1.0* the temperature level decreases lower than the other two cases because of the existence of a distinct *ORZ*. The temperature profiles at *Z/D=0.5* show similar trends with decreasing temperature level as the combustion gets leaner. Moreover, near the combustor wall, the temperature level decreases as a result of the radiative and convective losses to the surrounding. The rate of product formation (*PFR*) along the radial direction at the height of *Z/D=0.1* and *Z/D=0.5* from the burner is presented in Figure 61. At the stoichiometric combustion, *PFR* has peaks closer to the burner center with a valley between the two peaks, representing the unburnt jet. As the combustion gets leaner, the peaks shift away from the burner center and valley gets shallower. Also, fluctuations in the PFR profile at leaner combustion is observed due to the effect of high strain rate and local quenching of the flame. Moreover, the magnitude of the *PFR* decreases with reduction in the equivalence ratio signifying slower reaction rates.

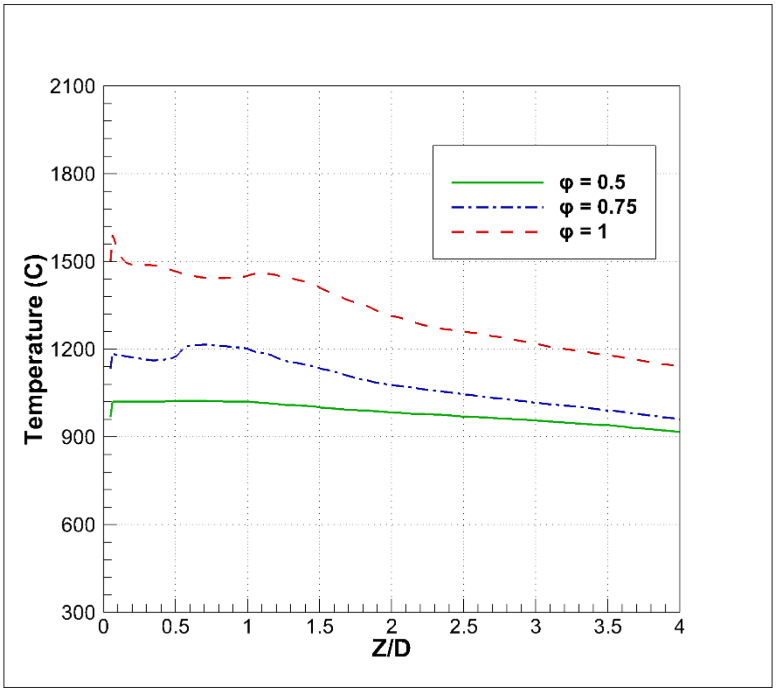

Figure 59. Axial temperature profile at different equivalence ratios.

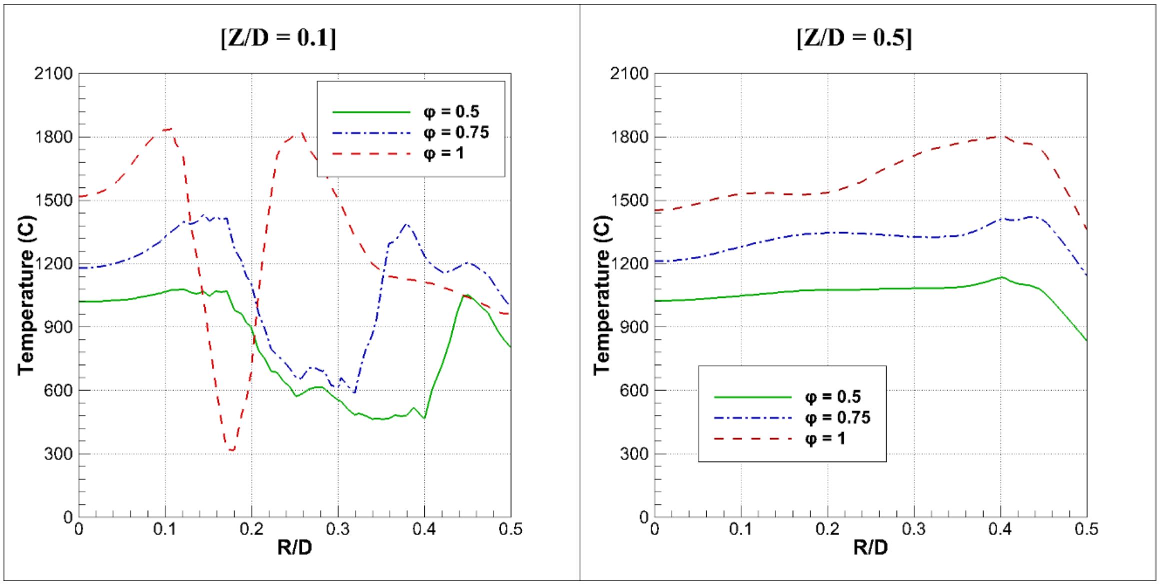

Figure 60. Radial temperature profile at the height of *Z/D=0.1* and *Z/D=0.5* from the burner at different equivalence ratios.

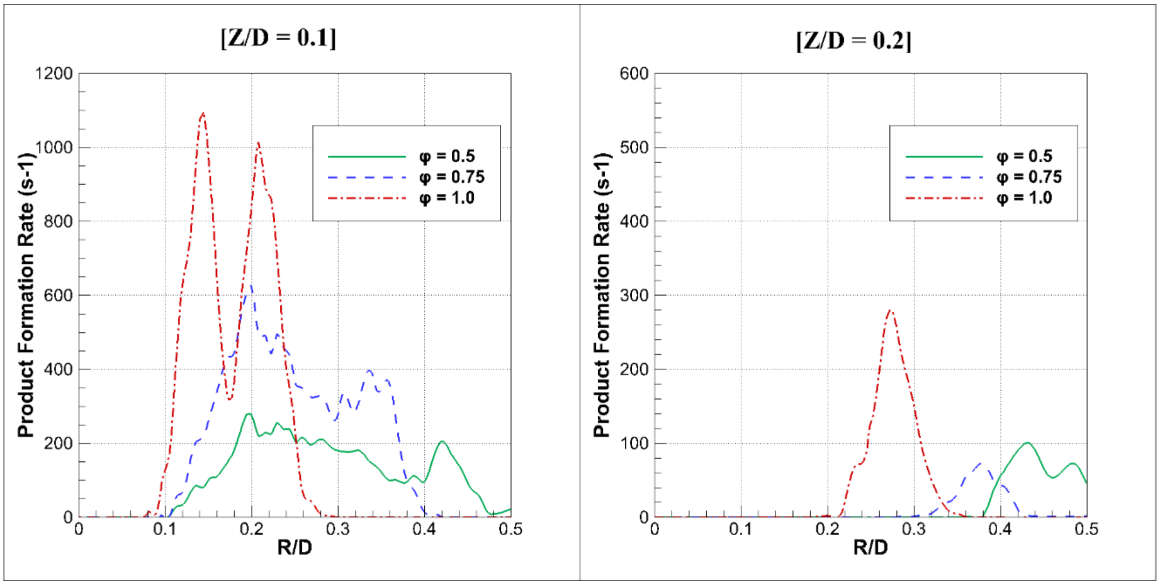

Figure 61. Product formation rate along the radial directions at the height of *Z/D=0.1* and *Z/D=0.5* from the burner at different equivalence ratios.

The effect of equivalence ratio on the flame thickness is presented in Figure 62. The flame thickness increases from *31.9 µm* at $\varphi=1.0$ to *55.5 µm* at $\varphi=0.75$. A further reduction in the equivalence ratio ($\varphi=0.5$), increases the flame thickness more than three times than at the stoichiometric combustion. Hence, at lower equivalence ratios, the flame thickness gets comparable to the Kolmogorov scales. This is apparent from Figure 63 as the Karlovitz number increases from *0.24* to *1.82* when the equivalence ratio is changed from *1.0* to *0.5*, respectively. Hence it can be concluded that the integral time scale is still larger than the chemical time scale, however, the smallest eddies are comparable to the flame thickness and are able to interact with the inner flame structure. The Damkohler number has reduced from *1672* ($\varphi=1.0$) to *9159* ($\varphi=0.5$), indicating the reaction rate is still dominated by the chemical kinetics. This kind of flame is well known as thickened flame regime. Moreover, the stretch induced by the Kolmogorov eddies also gets closer to the critical flame stretch, increasing the probability of flame quenching. The model is able to predict this phenomenon as can be seen from Figure 64. Both the critical rate of strain and the flame strain rate decrease as the equivalence is reduced. However, the critical strain rate decreases significantly as compared to the flame strain rate until both values get nearly the same at $\varphi=0.5$, and the effect of flame quenching gets discernible. This is also supported by the experimental results, where any attempt to reduce the equivalence ratio lower than *0.5* was unsuccessful and the flame blowout was observed.

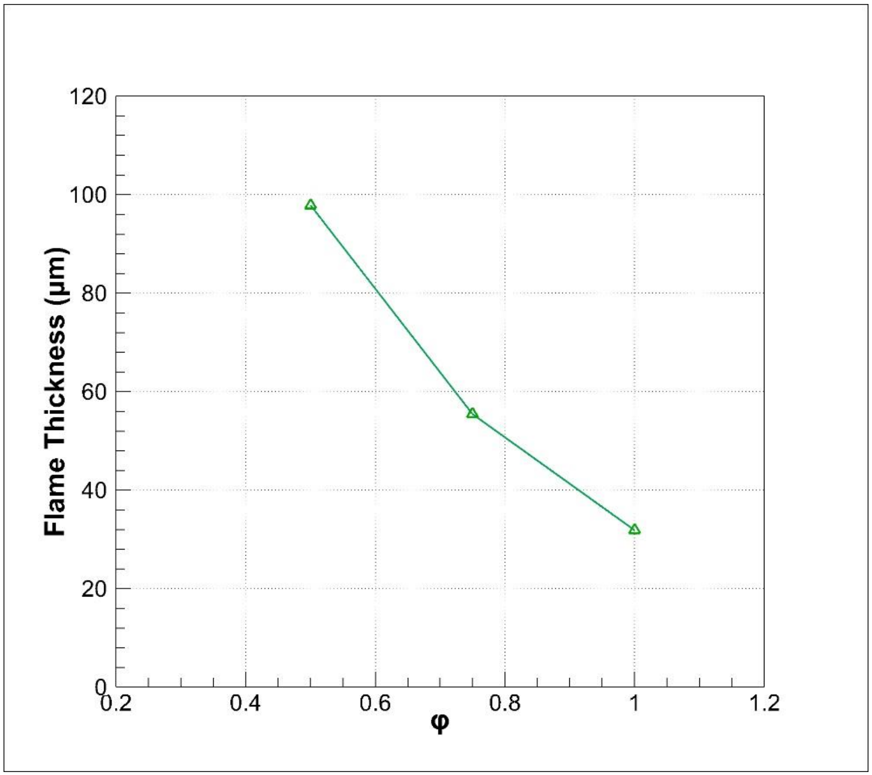

Figure 62. Effect of equivalence ratio on the flame thickness.

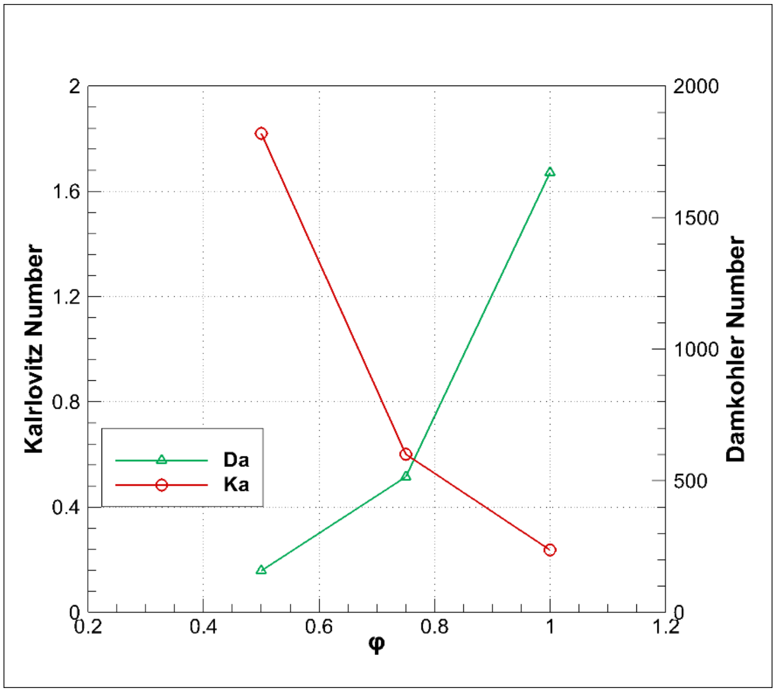

Figure 63. Effect of equivalence ratio on the Karlovitz number and the Damkohler number.

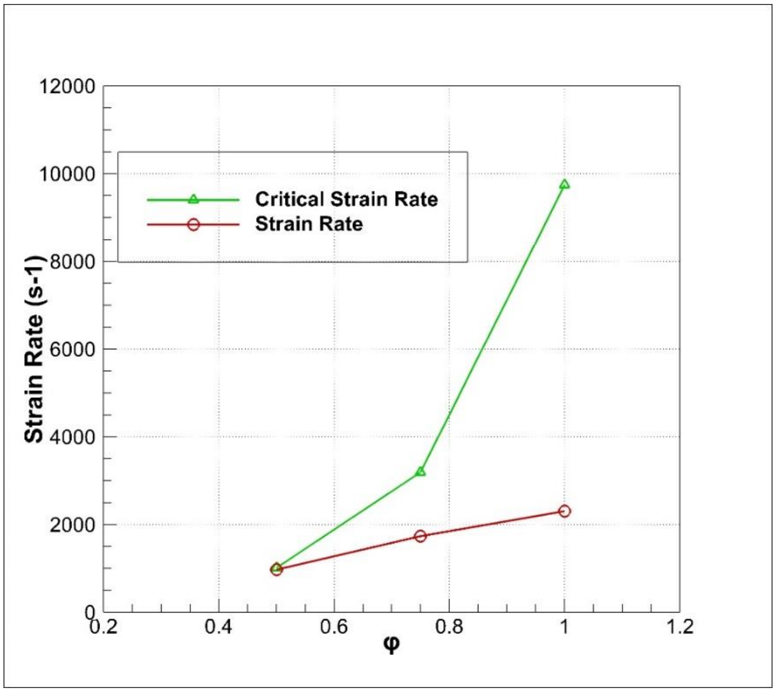

Figure 64. Strain rate and critical strain rate at different equivalence ratios.

6.3.3 Effect of the Reynolds Number

The presents section investigates the effect of throat Reynolds number on the flame characteristics and structure. The volumetric flow rates of the reactant gases were altered to get the Reynolds numbers value of *7696*, *9095* and *10494*, based on the hydraulic throat diameter. The equivalence ratio and the hydrogen fraction were set at *1.0* and *50%*, respectively. Figure 65 shows the experimental flame images, captured by high definition camera, and *OH* radical concentration contours from the numerical results. The shapes of the flames were found not to be affected by the Reynolds number except a slight elongation in the flame length was observed, as represented by both the experimental and numerical flame shapes. The flames at all the investigated Reynolds number are typical *V*-shaped, stabilized in both the inner and the outer shear layers. Better visualization of the regime is apparent from Figure 66, showing the velocity flow-field over the contours of temperature for all the three cases. The flames are characterized with a large *IRZ* and a distinct *ORZ*. With increasing Reynolds number, the center of the large eddy in the *IRZ* shifts downstream away from the burner. Moreover, at the higher Reynolds number, the primary eddy elongates and engulfs the secondary smaller eddies, which are distinct at the lower Reynolds number. However, the recirculation zones were to have only a marginal effect on the flame structure. The axial temperature profiles for all the three cases are shown in Figure 67. No significant difference is observed in the axial temperature distribution, however, the temperature level at Reynolds number *9095* was found to be slightly higher than the other two cases. This can be attributed to the entrainment of the colder air along the centerline is more prominent in the other two cases than at the Reynolds number of *9095*. The radial temperature profiles at the height of *Z/D=0.1* (Figure 68) shows a peak corresponding to the unburnt colder gases near the burner. The width and the height of the peaks were found to be increasing with the increasing Reynolds number, suggesting that the unburnt gases penetrating deeper into the combustor. At *Z/D=0.5*, again the temperature level at the Reynolds number of *9095* was found to be slightly greater than the other cases.

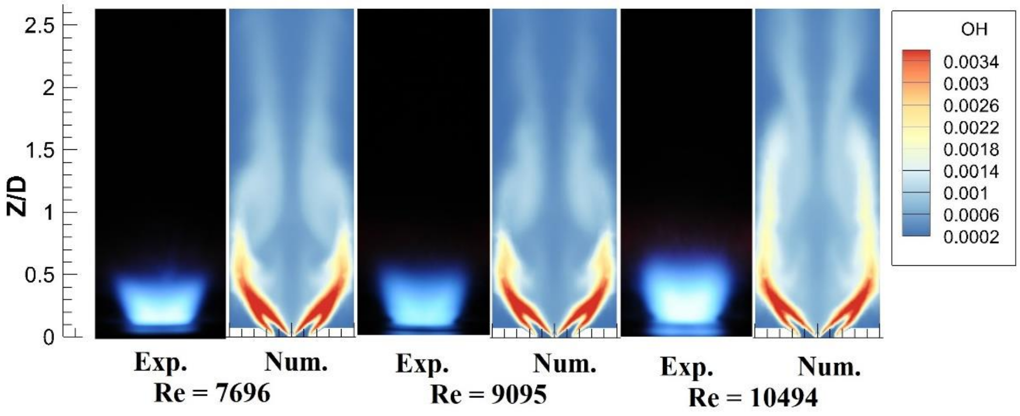

Figure 65. Comparison between experimental (photos taken by a high-speed camera) and numerical (based on *OH* contour plots) flame shapes at different Reynolds numbers.

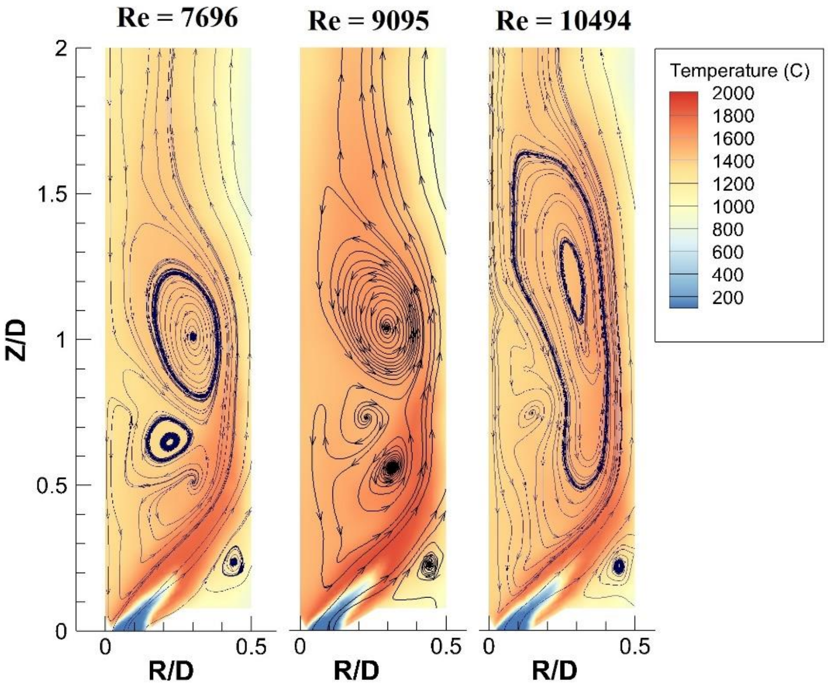

Figure 66. Velocity flow-field mapped over temperature contour at different Reynolds numbers.

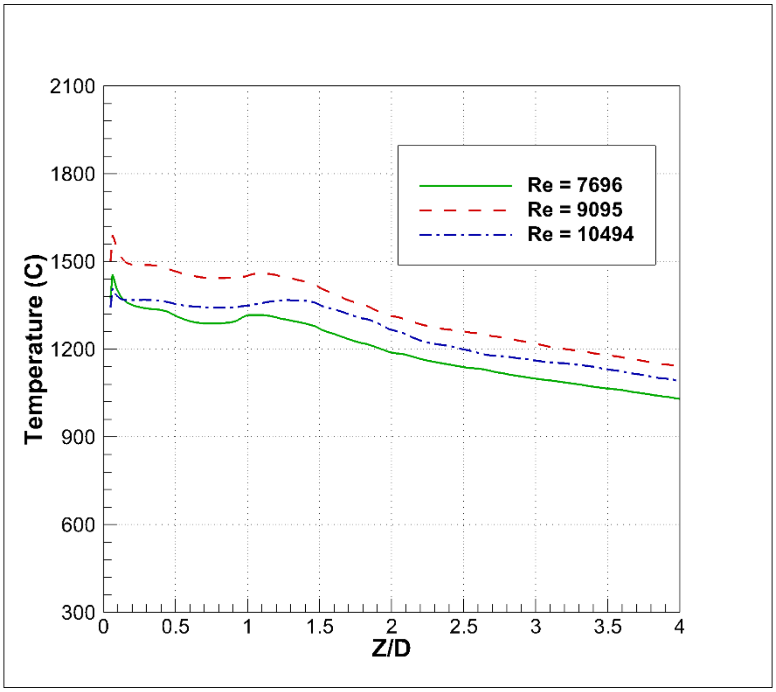

Figure 67. Axial temperature profile at different Reynolds numbers.

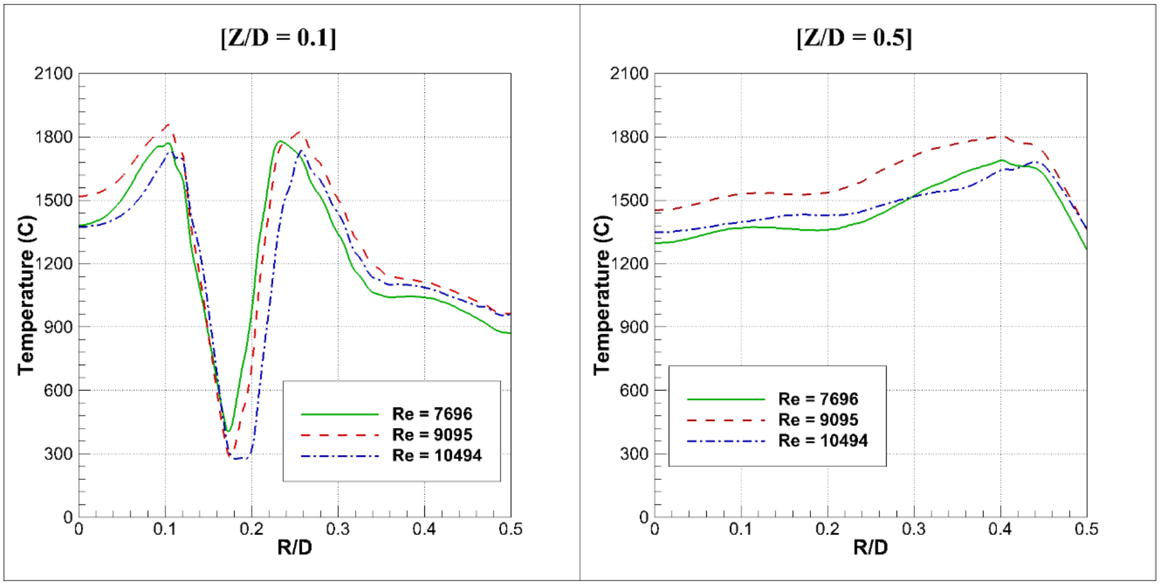

Figure 68. Radial temperature profile at the height of *Z/D=0.1* and *Z/D=0.5* from the burner at different Reynolds numbers.

Figure 69 shows the *PFR* at the height of *Z/D=0.1* and *Z/D=0.2* from the burner. It can be seen from the figure that the reaction rate increases monotonically with the increase in the Reynolds number. Moreover, the width of the reaction zone also increases with the Reynolds number. The Damkohler number was found to increase from *1050* at *Re=7596* to *1670*, however, no significant change was observed when the Reynolds number increased further (Figure 70). The effect of Reynolds number on the Karlovitz number was also observed to diminish as the Reynolds number was increased beyond *9000*. The effect of the throat Reynolds number on the strain rate is presented in Figure 71. The strain rate was found to increase from $2033\ s^{-1}$ to $2665\ s^{-1}$ as the Reynolds number increases from *7596* to *10494*, respectively. However, this marginal increase in the strain rate is still far below than the critical rate of strain for these cases and hence, no significant effect on the flame is observed.

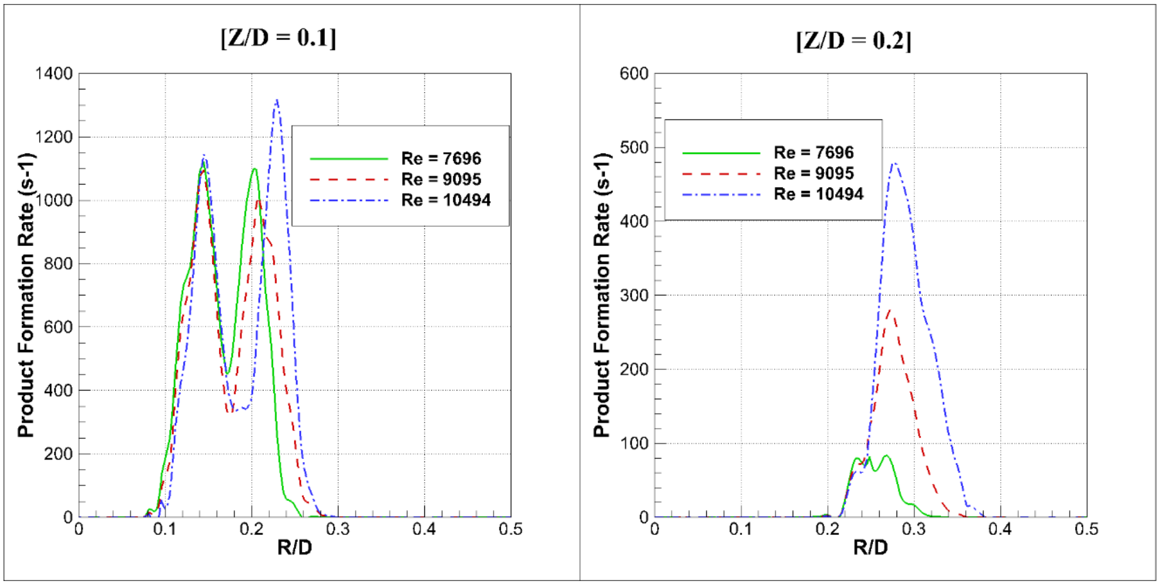

Figure 69. Product formation rate along the radial directions at the height of *Z/D=0.1* and *Z/D=0.5* from the burner at different Reynolds numbers.

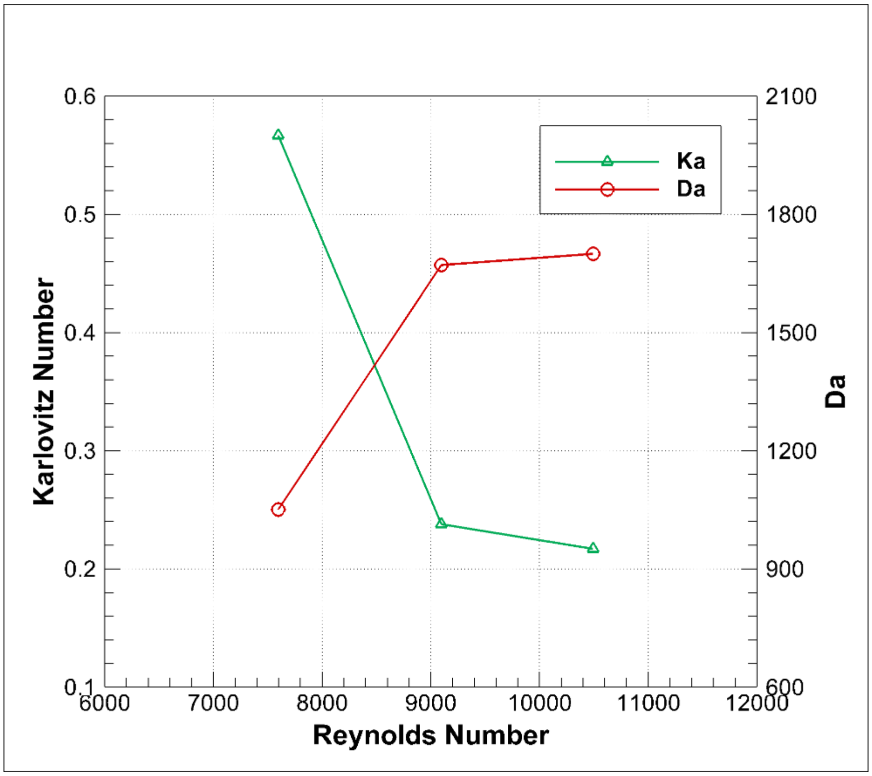

Figure 70. Effect of Reynolds number on the Karlovitz number and the Damkohler number.

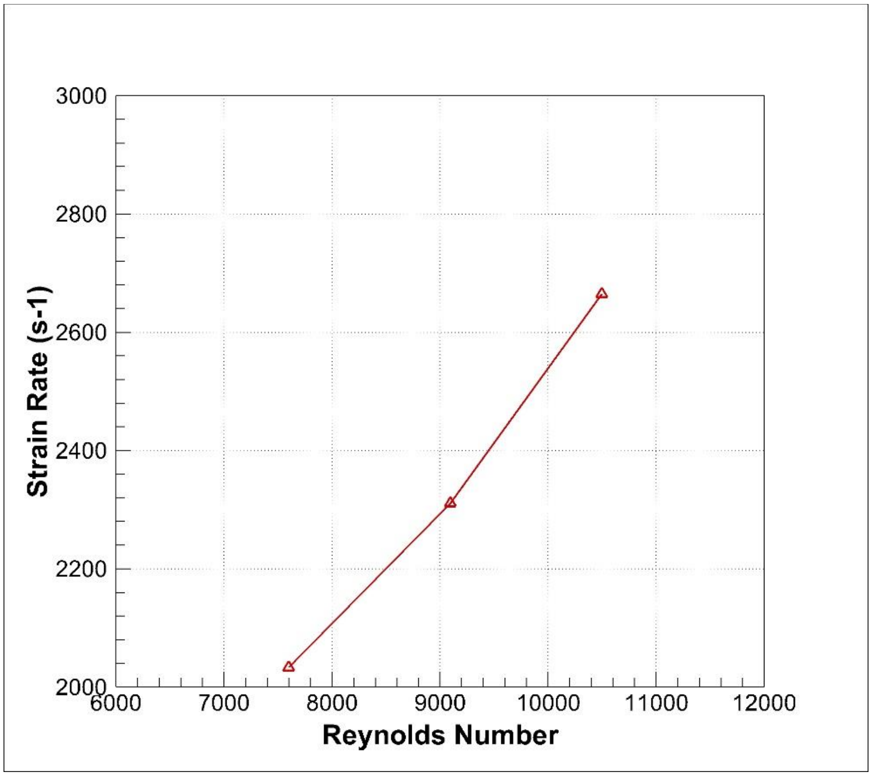

Figure 71. Strain rate at different Reynolds numbers.

6.3.4 Effect of the Swirl Number

In this section, the effect of the swirl number on the flame structure and the characteristics is studied. The volumetric flow rates in all the cases were kept constant, however, the tangential component of the velocity was changed to alter the swirl number. The hydrogen fraction was set to *50%*, while the oxygen fraction in the oxidizer stream was fixed to 30%. All the flames were investigated at the stoichiometric conditions. The contours of *OH* mole fraction for the three investigated cases are presented in Figure 72. The flame at the lower swirl number (*SN=0.69*) was found to have a longer length and characteristic *V*-shape. As the *SN* is increased, the flame length reduces and widens as can be seen from the figure. The flames at *SN=0.69* and *SN=0.98* is stabilized at both the inner and the outer shear layers, while, at higher swirl number (*SN=1.48*), the flame tends to stabilize at the inner shear layer, similar to the flames at lower equivalence ratios as discussed earlier. The velocity flow-field are plotted over the temperature contours in Figure 73. A primary large eddy (rotating counterclockwise) is observed in the *IRZ* with a small secondary eddy rotating in the clockwise direction at the lower swirl number (*SN=0.69*). A distinct *ORZ* is also observed in this regime. As the swirl number is increased to *0.98*, more secondary eddies appear and the *ORZ* is squeezed, however, still distinct. The primary eddy in the *IRZ* shifts further downstream away from the burner. The higher swirl number (*SN=1.48*) is characterized by a large primary eddy in the *IRZ*, engulfing all the smaller eddies. Moreover, another recirculation zone appears to develop further downstream of the combustor, both rotating in the counterclockwise direction. The *ORZ* diminishes and the flame tends to stabilize at the inner shear layer.

Figure 74 shows the axial temperature profile along the centerline of the combustor. It was observed that the effect of the *SN* is significant only in the region *Z/D<1*, while the temperature level further downstream are similar. The temperature levels near the burner region are highest at *SN=0.69* and reduce as the *SN* is increased. This is due to flattening of the flames as discussed earlier. The radial temperature profiles at the height of *Z/D=0.1* and *Z/D=0.5* from the burner is shown in Figure 75. At *Z/D=0.1*, low swirl flows are characterized by a peak, which shifts away from the centerline of the combustor as the swirl number is increased. The peak disappears at the high swirl number (*SN=1.48*), as the flame flattens. At further downstream (*Z/D=0.5*), the temperature level decreases with the increasing swirl number with lower temperature gradient near the combustor wall.

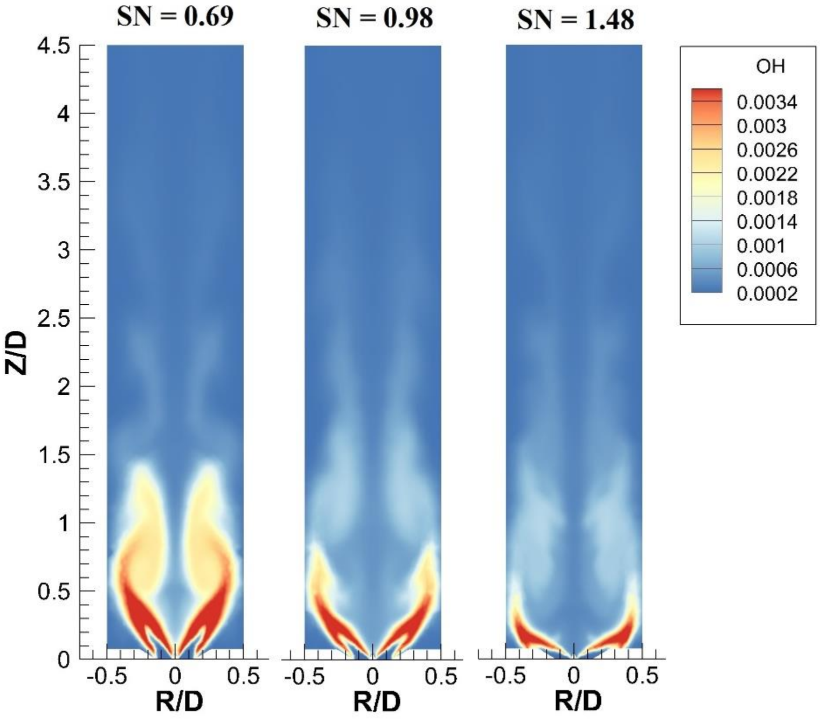

Figure 72. Numerical (based on *OH* contour plots) flame shapes at different swirl numbers.

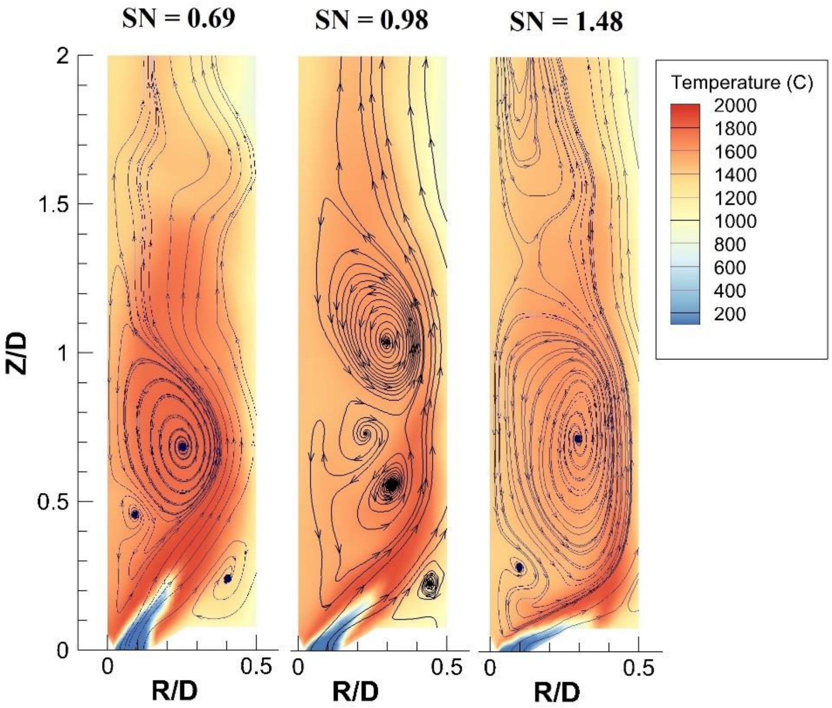

Figure 73. Velocity flow-field mapped over temperature contour at different swirl numbers.

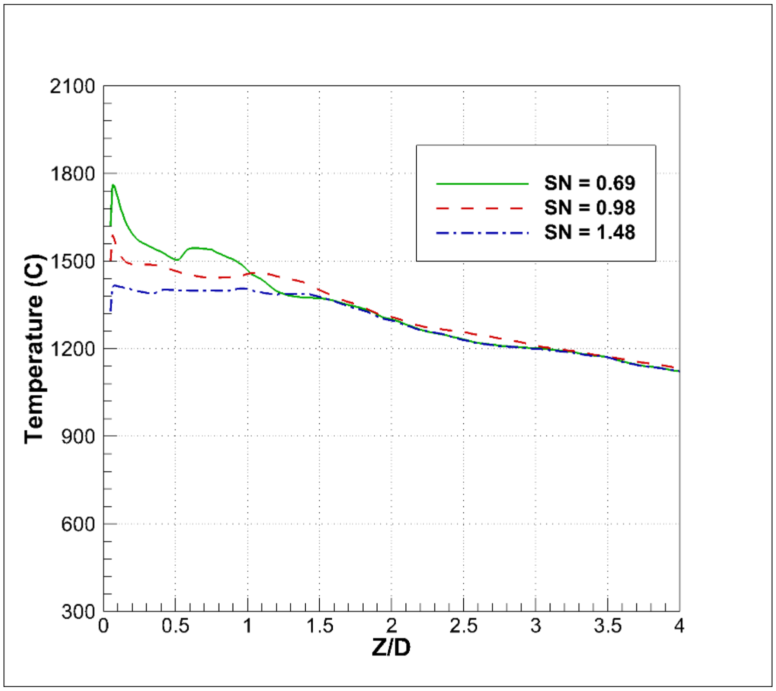

Figure 74. Axial temperature profile at different swirl numbers.

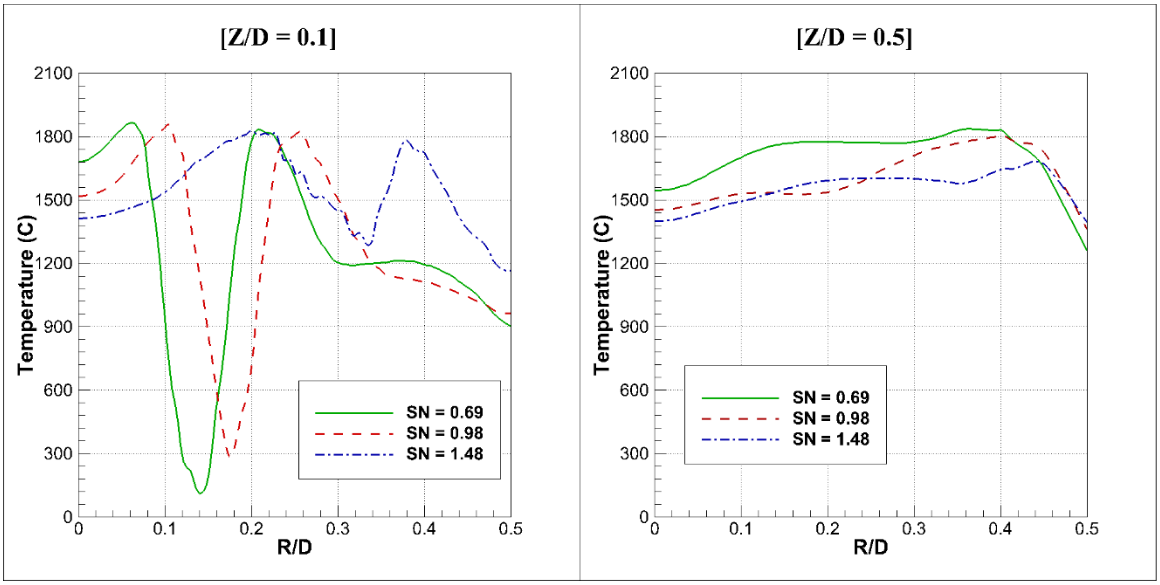

Figure 75. Radial temperature profile at the height of *Z/D=0.1* and *Z/D=0.5* from the burner at different swirl numbers.

Figure 76 shows the product formation rates in the radial direction at the height of *Z/D=0.1* and *Z/D=0.2*. The peaks of the *PFR* is shifts away from the center of the burner as the swirl number is increased. Moreover, the valley between the peaks at the height of *Z/D=0.1* disappears at the *SN=1.48* as the flame is stabilized at the corner. The *PFR* also reduces significantly at the height of *Z/D=0.2* for higher swirl number (*SN=1.48*) due to the complete combustion.

Effect of swirl number on the Karlovitz number and Damkohler number is presented in Figure 77. Both the non-dimensional numbers increase with the swirl number, however, the increase in *Ka* is only marginal, rising from *0.22* to *0.29* with the increase in *SN* from *0.69* to *1.48*, respectively. This suggests that the Kolmogorov scale decreases with swirl number, due to higher turbulence. Nevertheless, a huge jump (from *1300* to *2140*) in the *Da* is observed within the same change in the swirl number, indicating larger integral time scale as compared to the chemical time scale due to the augmentation of the large eddy as shown earlier in Figure 73. The strain rate was found to increase monotonically from *1540* s^{-1} to *2917* s^{-1} when the swirl number was increased from *0.60* to *1.48* (Figure 78), respectively.

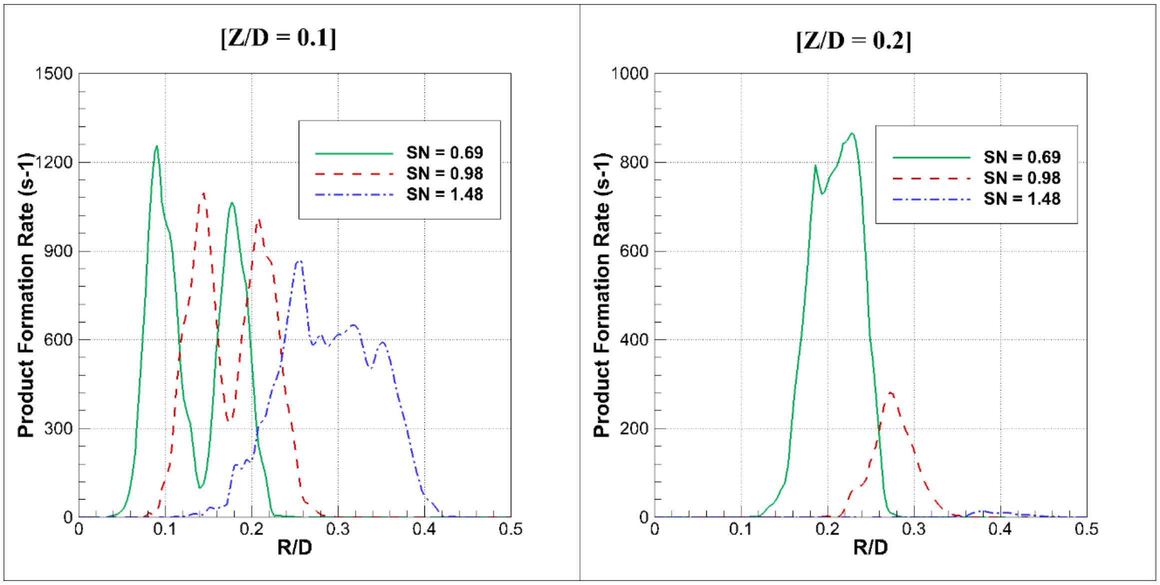

Figure 76. Product formation rate along the radial directions at the height of Z/D=0.1 and Z/D=0.5 from the burner at different swirl numbers.

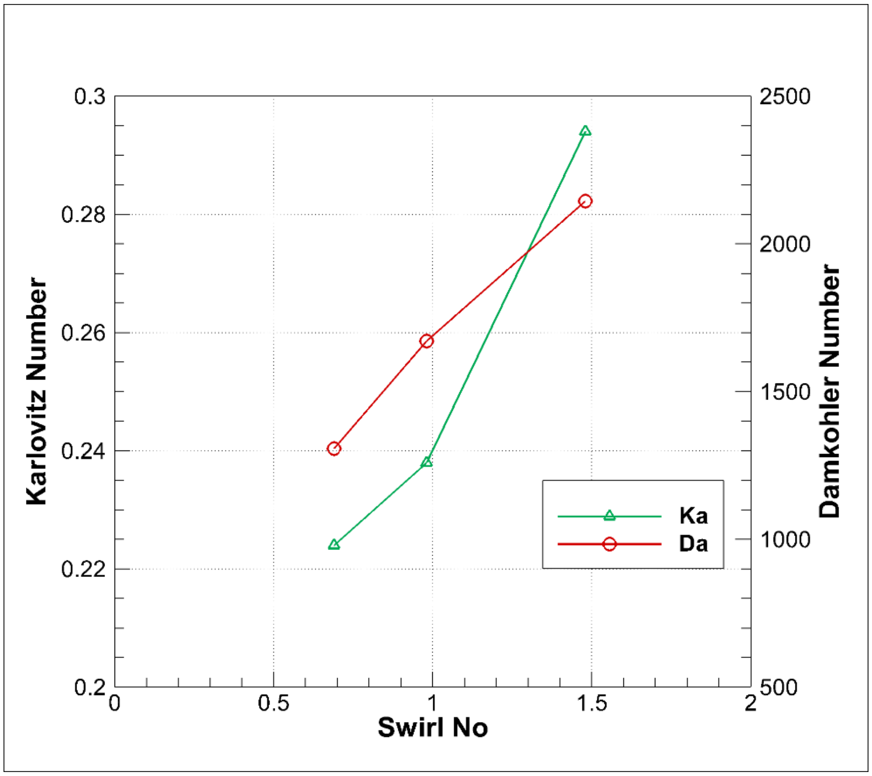

Figure 77. Effect of swirl number on the Karlovitz number and the Damkohler number.

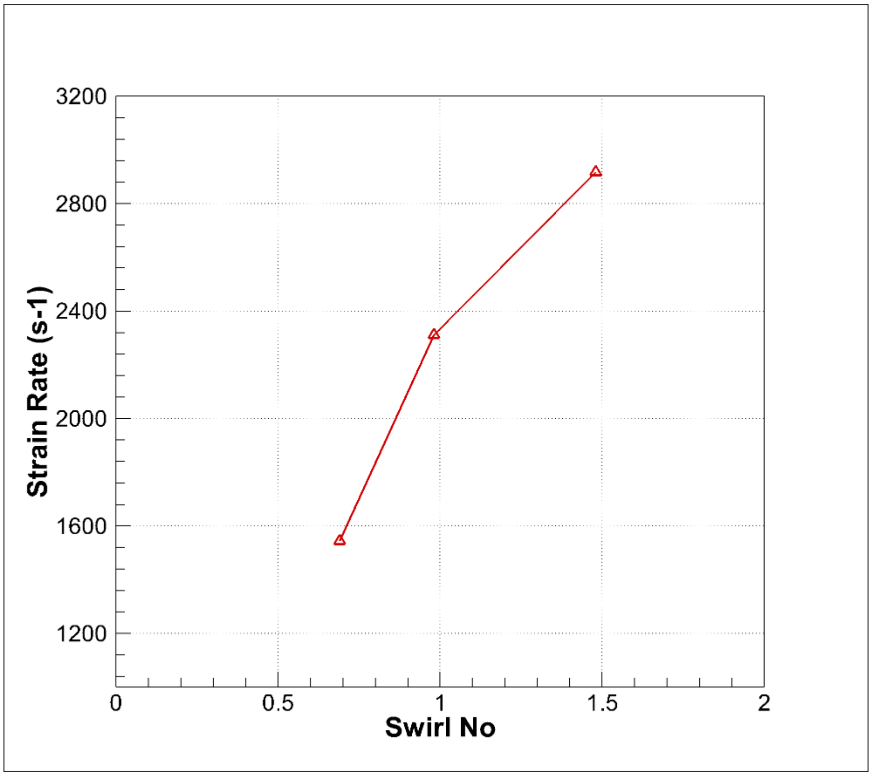

Figure 78. Strain rate at different swirl numbers.

6.4 Concluding Remarks

A detailed numerical study on the combustion characteristics of a premixed oxy-flame in a swirl-stabilized combustor was conducted to investigate the effect of hydrogen enrichment in methane flames. Moreover, the effects of equivalence ratio, throat Reynolds number and swirl number on the macrostructure of the flames and combustion characteristics are also investigated. A *LES* of the premixed turbulent flame was carried out using a commercial software package. The flames at higher hydrogen fractions are swirl stabilized with characteristic *V*-shaped flames and anchored at the tip of the center body. At *10% HF*, the flame is stabilized near the corner, spreading out to take the shape of the confinement. With the hydrogen enrichment, the combustion is characterized by the typical *V*-shape swirl stabilized flames with strong inner recirculation zones. Reaction rates are enhanced, and the flames tend to be more compact and intense with the increase in hydrogen percentage until the flashback is observed. At higher *HFs*, the inner recirculation zone is characterized by more than one single eddy, and the number and size of eddies are mainly function of *HF*. The role of outer recirculation zone in controlling flame stability diminishes at higher *HFs*. The rate of strain increases marginally with the increased *HF* in the fuel stream, however, the effect of HF on the critical strain rate is significant. Hence, the flames are more stable against quenching under the lean combustion with higher hydrogen fractions. Moreover, the reaction rate enhances with the hydrogen addition and carbon has to compete for oxygen, consequently characterized with higher *CO* emissions. The chemical time scale is found to be shorter than the smallest eddy time scale and hence, the inner flame structure is not affected by the turbulence. The reaction is governed by the laminar burning rate for all the cases considered.

The model also successfully predicted the flame macrostructure at different equivalence ratios. The flames at lower equivalence ratios are characterized by corner stabilization and single primary eddy in the *IRZ*. Higher equivalence ratio flames are swirl stabilized with the appearance of secondary smaller eddies and a distinct *ORZ*. The effect of Reynolds number on the flame structure was not found to be significant, however, it affected the *IRZ* downstream of the combustor. The flame shapes and the recirculation zones were also significantly affected by the swirl number. A detailed analysis of the combustion characteristics is presented.

CHAPTER 7

CONCLUSIONS AND RECOMMENDATIONS

The present thesis work can be subdivided into three major headings. The first part demonstrated the feasibility of oxy-combustion cycles with various configurations to see the effect of carbon capture on the cycle efficiency. In the second section, experimental investigations on the characteristics of hydrogen-enriched flames in a swirl-stabilized premixed combustor have been carried out through stability mapping and flame visualization. Lastly, a numerical study on the combustion characteristics of a premixed oxy-flame in a swirl-stabilized combustor was conducted to investigate the effect of hydrogen enrichment in methane flames.

7.1 Thermodynamic Analysis of the Oxy-combustion Cycles

The proposed cycles are the pre-mixed oxy-combustion with a separate *ASU* based on *ITM* technology, and the non-premixed oxy-combustion cycle with *ITM* integrated reactor and a gasification unit. The performance of both the cycles has been compared to a basic air-combustion cycle to demonstrate the effect of additional energy cost for oxygen separation on cycle performance. The thermodynamic analysis of the different systems in terms of first law and second law efficiencies has been presented. The major conclusions of the study can be summarized as follows:

- The thermal efficiency of the assumed base case system was calculated to be *42.7%.* The highest exergy loss was found to be in the reactor with an overall second law efficiency of *48.7%.*
- The non-premixed oxy-combustion system, based on the integrated *ITM* reactor, has lower efficiencies than that of the assumed base case air-combustion system with the thermal efficiency of the cycle of *37.8%.*
- The second law efficiency was around *50%*, with the largest exergy destructions in the H_2O splitter and the combustion chamber, where highly irreversible reactions taking place.
- In the proposed premixed oxy-combustion system the cost of oxygen separation via *ASU* dominates as the parameter to affect the cycle efficiency.
- The modification was able to improve the first law (*42.3%*) and the second law (*52.8%*) efficiencies of the system significantly to be much closer to those of the base case air-combustion cycle.

- The hydrogen blending in the fuel stream of the premixed system increases the overall first and second law efficiencies of the system, however, the change is only marginal.

7.2 Experimental Investigations of Hydrogen-enriched Flames

Experimental investigations on the characteristics of hydrogen-enriched flames in a swirl-stabilized premixed combustor have been carried out through stability mapping and flame visualization. A two-dimensional stability mapping was obtained by varying ϕ and *HF* over ranges of *0.3* to *1.0* and *0%* to *75%*, respectively. The selected flames at $\phi = 1$ with varying *HFs* and at $HF = 50\%$ with varying equivalence ratio have been imaged using a high definition camera. The major conclusions of the study can be summarized as follows:

- The flashback and blowout limits tend to move towards the leaner side with increasing hydrogen fraction in the fuel stream indicating increased flame speed.
- Increase in the heat release factor and wider operability range with hydrogen addition in the fuel blends has been observed.
- The stability limits are observed to follow the Reynolds number indicating its key role in controlling flame static stability limits.
- Corner stabilized flames were observed with lower hydrogen fractions and while high the flames at hydrogen fractions characterized by swirl stabilization.
- The equivalence ratio at which a transition of flame stabilization from the inner shear layer (*ISL*) to the outer recirculation zone (*ORZ*) occurs is determined for different inlet bulk velocities.

- The value of the transition equivalence ratio is reduced while increasing the inlet bulk velocity.
- The effect of throat velocities on the flame shape was found to be prominent for $\phi < 0.80$, suggesting the flame speed to be a weaker function of turbulent intensity near stoichiometric combustion.

7.3 Numerical Investigations of Hydrogen-enriched Flames

The combustion characteristics of a swirl-stabilized premixed oxy-flame has been investigated numerically to determine the effect of hydrogen blending with methane. Large Eddy Simulation (*LES*) of the premixed turbulent flame was carried out using a commercial software package. The major conclusions of the study can be summarized as follows:

- With the hydrogen enrichment, the combustion is characterized by the typical *V*-shape swirl stabilized flames with strong inner recirculation zones.
- Reaction rates are enhanced, and the flames tend to be more compact and intense with the increase in hydrogen percentage in the fuel blend.
- At higher *HFs*, the inner recirculation zone is characterized by more than one single eddy, and the number and size of eddies are mainly function of *HF*. The role of outer recirculation zone in controlling flame stability diminishes at higher *HFs*.
- The hydrogen enrichment increases the critical rate of strain and diminishes the possibility of flame quenching.
- Higher hydrogen fraction flames are also characterized by higher Damkohler number and lower Karlovitz number, indicating that the flame thickness is smaller than the smallest eddy present in the flow.

- The reaction is, thus, dominated by the chemical reaction rate and turbulence is not able to alter the inner flame structure.
- The model also successfully predicted the flame macrostructure at different equivalence ratios, Reynolds number, and swirl number.
- A detailed analysis of the combustion regimes has been presented.

7.4 Recommendations

The future work may include experimental investigations on the laminar flame speed calculations in oxy-combustion regime at different fuel and oxidizer compositions. Experimental investigation of oxy-flames using Laser diagnostics can be implemented to validate and develop a more robust numerical model. Moreover, numerical and as well as experimental investigation on the dynamic stability of the flame may provide further insight into the combustion characteristics as well as the applicability of *LES* framework in the prediction of the oxy-flames.

NOMENCLATURE

Abbreviations

AFT	Adiabatic Flame Temperature
ASU	Air Separation Unit
ATR	Autothermal Reactor
CCPS	Combined Cycle Power Generation System
CCS	Carbon Capture and Sequestration
CFD	Computational Fluid Dynamics
CLC	Chemical Looping Combustion
CTM	Continuous Thermodynamics
DM	Discrete Multicomponent
DO	Discreet Ordinates
EDM	Eddy Dissipation Model
EGR	Exhaust Gas Recirculation
ER	Equivalence Ratio
FBL	Flashback Limit
FSM	Full Second-order moment
GA	Genetic Algorithm
GHG	Green House Gases
GT	Gas Turbine
HF	Hydrogen Fraction

IGCC	Integrated Gasification Combined Cycle
IRZ	Inner recirculation Zone
ISL	Inner Shear Layer
ITM	Ion Transport Membrane
LBO	Lean Blowout
LES	Large Eddy Simulation
LSI	Low Swirl Injector
MEA	Monoethanolamine
MILD	Moderate or Intense Low-oxygen Dilution
MOF	Metal-Organic Framework
NGCC	Natural Gas Combined Cycle
OF	Oxygen Fraction
ORZ	Outer Recirculation Zone
OSL	Outer Shear Layer
OTM	Oxygen Transport Membrane
PD	Power Density
PDF	Probability Density Function
PPF	Partially Premixed Flame
RKE	Realizable k-ε model
RNG	Renormalization Group k-ε model
RSM	Reynolds Stress model

RTE	Radiative transfer equation
SIMPLE	Semi-Implicit Method for Pressure-Linked Equations
SKE	Standard k-ε model
SOFC	Solid Oxide Fuel Cell
TRI	Turbulence Radiation Interaction
WGS	Water Gas Shift
WSGGM	Weighted Sum of Gray Gas Model

Symbols

h	Specific enthalpy (*J/kg*)
s	Specific entropy (*J/K/kg*)
T	Temperature (*K*)
R	Universal gas constant (*J/K mol*)
Re	Reynolds number
Ka	Karlovitz number
Da	Damkohler number
L_s	Mixing length scale (*m*)
Sc	Schmidt number
Sw	Swirl number
S_L	Laminar flame speed (*m/s*)

S_T	Turbulent flame speed (m/s)
u'	Root mean square turbulent fluctuation (m/s)
f	Mixture fraction
f'	Mixture fraction variance
g_{cr}	Critical strain rate (s^{-1})

Greek Symbols

α	Thermal diffusivity (m^2/s)
λ	Thermal conductivity ($W/m\ K$)
ρ	Density (kg/m^3)
δ	Flame thickness (m)
ν	Kinematic viscosity (m^2/s)
Γ_Φ	Diffusion coefficient (m^2/s)
τ_{ij}	Subgrid-scale stress tensor (N/m^2)
μ_t	Turbulent viscosity ($kg/m\ s$)
η	Efficiency
κ	von Karman constant
γ	Heat release factor
k	Turbulent kinetic energy (m^2/s^2)
ε	Turbulent dissipation rate (m^2/s^3)

ϕ Equivalence ratio

REFERENCES

[1] *Advancing the Science of Climate Change, National Research Council-2010*.

[2] Solomon, S., Qin, D., Manning, M., Chen, Z., Marquis, M., Averyt, K. B., Miller, H. L., and Tignor, M., 2007, *Climate Change 2007 - The Physical Science Basis: Working Group I Contribution to the Fourth Assessment Report of the IPCC*, Cambridge University Press.

[3] *Commonwealth Scientific and Industrial Research Organization*.

[4] Armor, J. N., 2007, “Addressing the CO2 Dilemma,” Catal. Letters, 114(3–4), pp. 115–121.

[5] Lupion, M., Diego, R., Loubeau, L., and Navarrete, B., 2011, “CIUDEN CCS Project: Status of the CO2 Capture Technology Development Plant in Power Generation,” Energy Procedia, 4, pp. 5639–5646.

[6] Boden, T. A., Marland, G., and Andres, R. J., 2010, “Global, Regional, and National Fossil-Fuel CO2 Emissions,” Carbon Dioxide Inf. Anal. Center, Oak Ridge Natl. Lab. U.S. Dep. Energy, Oak Ridge, Tenn., U.S.A.

[7] Wall, T. F., 2007, “Combustion Processes for Carbon Capture,” Proc. Combust. Inst., 31(1), pp. 31–47.

[8] Simpson, A. P., and Simon, A. J., 2007, “Second Law Comparison of Oxy-Fuel Combustion and Post-Combustion Carbon Dioxide Separation,” Energy Convers. Manag., 48, pp. 3034–45.

[9] Eide, L., and Bailey, D., 2005, “Pre-Combustion Decarbonisation Process,” Oil gas Sci. Technol., 60, pp. 475–484.

[10] Dyer, P., Richards, R., Russek, S., and Taylor, D., 2000, “Ion Transport Membrane Technology for Oxygen Separation and Syngas Production,” Solid State Ionics, 134, pp. 21–33.

[11] Zhang, N., and Lior, N., 2008, “Two Novel Oxy-Fuel Power Cycles Integrated with Natural Gas Reforming and CO 2 Capture,” Energy, 33(2), pp. 340–351.

[12] “Http://Www.Globalccsinstitute.Com/.”

[13] Bailey, D., and Feron, P., 2005, “Post-Combustion Decarbonisation Process,” Oil gas Sci. Technol., 60, pp. 461–474.

[14] Rubin, E., Meyer, L., and Coninck, H., 2005, *Carbon Dioxide Capture and Storage, Technical Summary*.

[15] Singh, D., Croiset, E., Douglas, P., and Douglas, M., 2003, "Techno-Economic Study of CO2 Capture from an Existing Coal-Fired Power Plant: MEA Scrubbing vs. O2/CO2 Recycle Combustion," Energy Convers. Manag., 44, pp. 3073–3091.

[16] Li, J.-R., Ma, Y., McCarthy, M. C., Sculley, J., Yu, J., Jeong, H.-K., Balbuena, P. B., and Zhou, H.-C., 2011, "Carbon Dioxide Capture-Related Gas Adsorption and Separation in Metal-Organic Frameworks," Coord. Chem. Rev., 255(15–16), pp. 1791–1823.

[17] Nemitallah, M. A., Habib, M. A., Badr, H. M., Said, S. A., Jamal, A., Ben-Mansour, R., Mokheimer, E. M. A., and Mezghani, K., 2017, "Oxy-Fuel Combustion Technology: Current Status, Applications, and Trends," Int. J. energy Res.

[18] Amato, A., Hudak, B., D'Carlo, P., Noble, D., Scarborough, D., Seitzman, J., and Lieuwen, T., 2011, "Methane Oxycombustion for Low CO2 Cycles: Blowoff Measurements and Analysis," J. Eng. Gas Turbines Power, 133(6), p. .

[19] Chen, L., and Ghoniem, A. F., 2012, "Simulation of Oxy-Coal Combustion in a 100 KW Th Test Facility Using RANS and LES: A Validation Study," Energy & Fuels, 26(8), pp. 4783–4798.

[20] Imteyaz, B., and Habib, M. A., 2015, "Study of Combustion Characteristics of Ethanol at Different Dilution With the Carrier Gas," J. Energy Resour. Technol., 137(3), p. 032205.

[21] Imteyaz, B., Habib, M. A., and Ben-Mansour, R., 2017, "The Characteristics of Oxycombustion of Liquid Fuel in a Typical Water-Tube Boiler," Energy & Fuels, 31(6), pp. 6305–6313.

[22] Park, S., Kim, T., Sohn, J., and Lee, Y., 2011, "An Integrated Power Generation System Combining Solid Oxide Fuel Cell and Oxy-Fuel Combustion for High Performance and CO2 Capture," Appl. Energy, 88(4), pp. 1187–1196.

[23] Kakaras, E., Koumanakos, a., Doukelis, a., Giannakopoulos, D., and Vorrias, I., 2007, "Oxyfuel Boiler Design in a Lignite-Fired Power Plant," Fuel, 86(14), pp. 2144–2150.

[24] Zhu, L., and Fan, J., 2015, "Thermodynamic Analysis of H2 Production from CaO Sorption-Enhanced Methane Steam Reforming Thermally Coupled with Chemical Looping Combustion as a Novel Technology," Int. J. energy Res., 39, pp. 356–369.

[25] Atsonios, K., Panopoulos, K. D., Doukelis, a., Koumanakos, a., and Kakaras, E., 2012, "Exergy Analysis of a Hydrogen Fired Combined Cycle with Natural Gas Reforming and Membrane Assisted Shift Reactors for CO 2 Capture," Energy Convers. Manag., 60, pp. 196–203.

[26] Pak, P. S., Lee, Y. D., and Ahn, K. Y., 2010, "Characteristic Evaluation of a CO2-Capturing Repowering System Based on Oxy-Fuel Combustion and Exergetic Flow Analyses for Improving Efficiency," Int. J. energy Res., 34, pp. 1272–1284.

[27] Fu, C., and Gundersen, T., 2010, "Heat Integration of an Oxy-Combustion Process for Coal-Fired Power Plants with CO2 Capture by Pinch Analysis," Chem. Eng. Trans., 21, pp. 181–186.

[28] Fu, C., and Gundersen, T., 2012, “Using Exergy Analysis to Reduce Power Consumption in Air Separation Units for Oxy-Combustion Processes,” Energy, 44(1), pp. 60–68.

[29] Fu, C., and Gundersen, T., 2013, “Exergy Analysis and Heat Integration of a Coal-Based Oxy-Combustion Power Plant,” Energy and Fuels, 27(11), pp. 7138–7149.

[30] Hunt, A., Dimitrakopoulos, G., and Ghoniem, A. F., 2015, “Surface Oxygen Vacancy and Oxygen Permeation Flux Limits of Perovskite Ion Transport Membranes,” J. Memb. Sci., 489, pp. 248–257.

[31] Hunt, A., Dimitrakopoulos, G., Kirchen, P., and Ghoniem, A. F., 2014, “Measuring the Oxygen Profile and Permeation Flux across an Ion Transport Membrane and the Development and Validation of a Multistep Surface Exchange Model,” J. Memb. Sci., 468, pp. 62–72.

[32] Sunarso, J., Baumann, S., Serra, J. M., Meulenberg, W. A., Liu, S., Lin, Y. S., and Diniz da Costa, J. C., 2008, “Mixed Ionic-Electronic Conducting (MIEC) Ceramic-Based Membranes for Oxygen Separation,” J. Memb. Sci., 320(1–2), pp. 13–41.

[33] Mancini, N. D., and Mitsos, A., 2011, “Ion Transport Membrane Reactors for Oxy-Combustion – Part I: Intermediate-Fidelity Modeling,” Energy, 36(8), pp. 4701–4720.

[34] Kirchen, P., Apo, D. J., Hunt, A., and Ghoniem, A. F., 2013, “A Novel Ion Transport Membrane Reactor for Fundamental Investigations of Oxygen Permeation and Oxy-Combustion under Reactive Flow Conditions,” Proc. Combust. Inst., 34(2), pp. 3463–3470.

[35] Xiong, J., Zhao, H., and Zheng, C., 2011, “Exergy Analysis of a 600 MW Oxy-Combustion Pulverized-Coal- Fired Power Plant,” Energy and Fuels, 25(8), pp. 3854–3864.

[36] Xiong, J., Zhao, H., and Zheng, C., 2012, “Thermoeconomic Cost Analysis of a 600MWeoxy-Combustion Pulverized-Coal-Fired Power Plant,” Int. J. Greenh. Gas Control, 9, pp. 469–483.

[37] Scaccabarozzi, R., Gatti, M., and Martelli, E., 2016, “Thermodynamic Analysis and Numerical Optimization of the NET Power Oxy-Combustion Cycle,” Appl. Energy, 178, pp. 505–526.

[38] Ziółkowski, P., Zakrzewski, W., Kaczmarczyk, O., and Badur, J., 2013, “Thermodynamic Analysis of the Double Brayton Cycle with the Use of Oxy Combustion and Capture of CO2,” Arch. Thermodyn., 34(2), pp. 23–38.

[39] Pfaff, I., and Kather, A., 2009, “Comparative Thermodynamic Analysis and Integration Issues of CCS Steam Power Plants Based on Oxy-Combustion with Cryogenic or Membrane Based Air Separation,” Energy Procedia, 1(1), pp. 495–502.

[40] Castillo, R., 2011, “Thermodynamic Analysis of a Hard Coal Oxyfuel Power Plant with High Temperature Three-End Membrane for Air Separation,” Appl. Energy, 88(5), pp. 1480–1493.

[41] Skorek-Osikowska, A., Bartela, Ł., and Kotowicz, J., 2015, "A Comparative Thermodynamic, Economic and Risk Analysis Concerning Implementation of Oxy-Combustion Power Plants Integrated with Cryogenic and Hybrid Air Separation Units," Energy Convers. Manag., 92, pp. 421–430.

[42] Mancini, N. D., and Mitsos, a., 2011, "Ion Transport Membrane Reactors for Oxy-Combustion–Part II: Analysis and Comparison of Alternatives," Energy, 36(8), pp. 4721–4739.

[43] Mazas, A., Lacoste, D., Fiorina, B., and Schuller, T., 2009, "Effects of Water Vapor Addition on the Laminar Burning Velocity of Methane Oxygen-Enhanced Flames at Atmospheric Pressure," Proc. Eur. Combust. Meet., (January 2009), pp. 1–6.

[44] Li, Y. H., Chen, G. B., Lin, Y.-C., Wu, F.-H., and Chao, Y. C., 2013, "Effects of Flue Gas Addition on the Premixed Oxy-Methane Flames," 24th Int. Colloq. Dyn. Explos. React. Syst.

[45] Marsh, R., Runyon, J., Giles, A., Morris, S., Pugh, D., Valera-Medina, A., and Bowen, P., 2016, "Premixed Methane Oxycombustion in Nitrogen and Carbon Dioxide Atmospheres: Measurement of Operating Limits, Flame Location and Emissions," *Proceedings of the Combustion Institute*, Elsevier Inc., p. .

[46] Srodowiska, R. O., and Jerzak, W., 2015, "Formation of CO in the Oxy-Fuel Premixed Flame," Annu. Set Environ. Prot., (September).

[47] Osaka, Y., Kobayashi, N., Razzak, M. a., Ohno, N., Takamura, S., and Uesugi, Y., 2010, "Basic Study on the Generation of RF Plasmas in Premixed Oxy-Combustion with Methane," Plasma Fusion Res., 5(X), pp. 010–010.

[48] Taamallah, S., Chakroun, N. W., Watanabe, H., Shanbhogue, S. J., and Ghoniem, A. F., 2015, "On the Characteristic Flow and Flame Times for Scaling Oxy and Air Flame Stabilization Modes in Premixed Swirl Combustion," *Proceedings of the Combustion Institute*, Elsevier Inc., pp. 3799–3807.

[49] Shroll, A. P., Shanbhogue, S. J., and Ghoniem, A. F., 2012, "Dynamic-Stability Characteristics of Premixed Methane Oxy-Combustion," J. Eng. Gas Turbines Power, 134(5), p. 051504.

[50] Jourdaine, P., Mirat, C., Beaunier, J., Joumani, Y., and Schuller, T., 2015, "A Comparison of the Structure of N2 and CO2 Diluted CH4 / O2 Premixed Flames in a Swirled Combustor," *Proceedings of the European Combustion Meeting*.

[51] Jourdaine, P., Mirat, C., Caudal, J., Lo, A., and Schuller, T., 2016, "A Comparison between the Stabilization of Premixed Swirling CO2-Diluted Methane Oxy-Flames and Methane/Air Flames," Fuel.

[52] Wang, J., Huang, Z., Tang, C., Miao, H., and Wang, X., 2009, "Numerical Study of the Effect of Hydrogen Addition on Methane-Air Mixtures Combustion," Int. J. Hydrogen Energy, 34(2), pp. 1084–1096.

[53] Ditaranto, M., Anantharaman, R., and Weydahl, T., 2013, "Performance and NOx Emissions of Refinery Fired Heaters Retrofitted to Hydrogen Combustion," Energy Procedia, 37, pp. 7214–7220.

[54] Riahi, Z., Bounaouara, H., Hraiech, I., Ali Mergheni, M., Sautet, J.-C., and Ben Nasrallah, S., 2017, “Combustion with Mixed Enrichment of Oxygen and Hydrogen in Lean Regime.”

[55] Rezgui, Y., and Guemini, M., 2017, “Effect of Hydrogen Addition on Equimolar Dimethyl Ether/Iso-Octane/Oxygen/Argon Premixed Flames,” Int. J. Hydrogen Energy, 42(49), pp. 29557–29573.

[56] Kim, H. S., Arghode, V. K., and Gupta, A. K., 2009, “Flame Characteristics of Hydrogen-Enriched Methane-Air Premixed Swirling Flames,” Int. J. Hydrogen Energy, 34(2), pp. 1063–1073.

[57] Wietschel, M., and Ball, M., 2009, “The Future of Hydrogen – Opportunities and Challenges,” Hydrog. Econ. Oppor. Challenges, 9780521882(2), pp. 613–639.

[58] Edwards, P. P., Kuznetsov, V. L., David, W. I. F., and Brandon, N. P., 2008, “Hydrogen and Fuel Cells: Towards a Sustainable Energy Future,” Energy Policy, 36(12), pp. 4356–4362.

[59] 2008, *European Commission. Hyways: The European Hydrogen Roadmap: Contract SES6-502596, EUR-OP*, Luxembourg.

[60] Choudhuri, A. R., and Gollahalli, S. R., 2000, “Combustion Characteristics of Hydrogen-Hydrocarbon Hybrid Fuels,” Int. J. Hydrogen Energy, 25(5), pp. 451–462.

[61] Gu, M., Chu, H., and Liu, F., 2016, “Effects of Simultaneous Hydrogen Enrichment and Carbon Dioxide Dilution of Fuel on Soot Formation in an Axisymmetric Coflow Laminar Ethylene/Air Diffusion Flame,” Combust. Flame, 166, pp. 216–228.

[62] Park, S. H., Lee, K. M., and Hwang, C. H., 2011, “Effects of Hydrogen Addition on Soot Formation and Oxidation in Laminar Premixed C2H2/Air Flames,” Int. J. Hydrogen Energy, 36(15), pp. 9304–9311.

[63] Pandey, P., Pundir, B. P., and Panigrahi, P. K., 2007, “Hydrogen Addition to Acetylene-Air Laminar Diffusion Flames: Studies on Soot Formation under Different Flow Arrangements,” Combust. Flame, 148(4), pp. 249–262.

[64] Gülder, Ö. L., Snelling, D. R., and Sawchuk, R. A., 1996, “Influence of Hydrogen Addition to Fuel on Temperature Field and Soot Formation in Diffusion Flames,” Symp. Combust., 26(2), pp. 2351–2358.

[65] Boushaki, T., Dhué, Y., Selle, L., Ferret, B., and Poinsot, T., 2012, “Effects of Hydrogen and Steam Addition on Laminar Burning Velocity of Methane-Air Premixed Flame: Experimental and Numerical Analysis,” Int. J. Hydrogen Energy, 37(11), pp. 9412–9422.

[66] Guo, H., Smallwood, G. J., Liu, F., and Ju, Y., 2004, “Accepted for Publication in The Effect of Hydrogen Addition on Flammability Limit and NOx Emission in Lean Counterflow CH 4 / Air Premixed Flames,” engine.princeton.edu, 30(2).

[67] Shy, S. S., Chen, Y. C., Yang, C. H., Liu, C. C., and Huang, C. M., 2008, “Effects of H2 or CO2 Addition, Equivalence Ratio, and Turbulent Straining on Turbulent Burning Velocities for Lean Premixed Methane Combustion,” Combust. Flame,

153(4), pp. 510–524.

[68] Imteyaz, B., medhat A Nemitallah, Ahmed A Abdelhafez, and Mohamed A Habib, 2018, "Combustion Behavior and Stability Map of Hydrogen-Enriched Oxy-Methane Premixed Flames in a Model Gas Turbine Combustor," Int. J. Hydrogen Energy, 43(34), pp. 16652–16666.

[69] Abdelwahid, S., Nemitallah, M. A., Imteyaz, B., Abdelhafez, A. A., and Habib, M. A. M., 2018, "On the Effects of H2-Enrichment and Inlet Velocity on Stability Limits and Shape of CH4/H2-O2/CO2 Flames in a Premixed Swirl Combustor," Energy & Fuels, 32, p. acs.energyfuels.8b01958.

[70] Halter, F., Chauveau, C., and Gökalp, I., 2007, "Characterization of the Effects of Hydrogen Addition in Premixed Methane/Air Flames," Int. J. Hydrogen Energy, 32(13), pp. 2585–2592.

[71] Hu, E., Huang, Z., He, J., Jin, C., and Zheng, J., 2009, "Experimental and Numerical Study on Laminar Burning Characteristics of Premixed Methane – Hydrogen – Air Flames," Int. J. Hydrogen Energy, 34, pp. 4876–4888.

[72] Schefer, R. W., 2003, "Hydrogen Enrichment for Improved Lean Flame Stability," Int. J. Hydrogen Energy, 28, pp. 1131–1141.

[73] Gersen, S., Anikin, N. B., Mokhov, A. V., and Levinsky, H. B., 2008, "Ignition Properties of Methane/Hydrogen Mixtures in a Rapid Compression Machine," Int. J. Hydrogen Energy, 33(7), pp. 1957–1964.

[74] Cheng, R. K., and Oppenheim, A. K., 1984, "Autoignition in Methanehydrogen Mixtures," Combust. Flame, 58(2), pp. 125–139.

[75] Yu, G., Law, C. K., and Wu, C. K., 1986, "Laminar Flame Speeds of Hydrocarbon + Air Mixtures with Hydrogen Addition," Combust. Flame, 63(3), pp. 339–347.

[76] Law, C. K., and Kwon, O. C., 2004, "Effects of Hydrocarbon Substitution on Atmospheric Hydrogen-Air Flame Propagation," Int. J. Hydrogen Energy, 29(8), pp. 867–879.

[77] Ilbas, M., Crayford, A. P., Yilmaz, I., Bowen, P. J., and Syred, N., 2006, "Laminar-Burning Velocities of Hydrogen-Air and Hydrogen-Methane-Air Mixtures: An Experimental Study," Int. J. Hydrogen Energy, 31(12), pp. 1768–1779.

[78] Dirrenberger, P., Le Gall, H., Bounaceur, R., Herbinet, O., Glaude, P. A., Konnov, A., and Battin-Leclerc, F., 2011, "Measurements of Laminar Flame Velocity for Components of Natural Gas," Energy and Fuels, 25(9), pp. 3875–3884.

[79] Katharina, G., Albin, E., Krüger, O., Paschereit, C. O., Katharina, G., Albin, E., Krüger, O., Oliver, C., and Burning, P., 2016, "Burning Velocities of Hydrogen-Methane-Air Mixtures at Highly Steam-Diluted Conditions To Cite This Version : HAL Id : Hal-00954523 BURNING VELOCITIES OF HYDROGEN-METHANE-AIR."

[80] Dahoe, A. E., 2005, "Laminar Burning Velocities of Hydrogen-Air Mixtures from Closed Vessel Gas Explosions," J. Loss Prev. Process Ind., 18(3), pp. 152–166.

[81] Sarli, V. Di, and Benedetto, A. Di, 2007, "Laminar Burning Velocity of Hydrogen

– Methane / Air Premixed Flames,” 32, pp. 637–646.

[82] Tang, C., Huang, Z., Jin, C., He, J., Wang, J., Wang, X., and Miao, H., 2008, “Laminar Burning Velocities and Combustion Characteristics of Propane – Hydrogen – Air Premixed Flames,” Int. J. Hydrogen Energy, 33, pp. 4906–4914.

[83] Sankaran, R., and Im, H. G., 2006, “Effects of Hydrogen Addition on the Markstein Length and Flammability Limit of Stretched Methane/Air Premixed Flames,” Combust. Sci. Technol., 178(January 2012), pp. 37–41.

[84] Nakahara, M., and Kido, H., 2008, “Study on the Turbulent Burning Velocity of Hydrogen Mixtures Including Hydrocarbons,” AIAA J., 46(7).

[85] Daniele, S., Jansohn, P., Mantzaras, J., and Boulouchos, K., 2011, “Turbulent Flame Speed for Syngas at Gas Turbine Relevant Conditions,” Proc. Combust. Inst., 33(2), pp. 2937–2944.

[86] Daniele, S., Jansohn, P., and Boulouchos, K., 2009, “Experimental Investigation of Lean Premixed Syngas Combustion at Gas Turbine Relevant Conditions: Lean Blow Out Limits, Emissions and Turbulent Flame Speed,” *Italian Section of the Combustion Institute*.

[87] Cheng, R. K., and Littlejohn, D., 2008, “Laboratory Study of Premixed H2-Air and H2–N2-Air Flames in a Low-Swirl Injector for Ultralow Emissions Gas Turbines,” J. Eng. Gas Turbines Power, 130(3), p. 031503.

[88] Ghoniem, A. F., Annaswamy, A., Park, S., and Sobhani, Z. C., 2005, “Stability and Emissions Control Using Air Injection and H2 Addition in Premixed Combustion,” Proc. Combust. Inst., 30 II(2), pp. 1765–1773.

[89] Chen, S., and Zheng, C., 2011, “Counterflow Diffusion Flame of Hydrogen-Enriched Biogas under MILD Oxy-Fuel Condition,” Int. J. Hydrogen Energy, 36(23), pp. 15403–15413.

[90] Riahi, Z., Mergheni, M. A., Sautet, J. C., and Ben Nasrallah, S., 2016, “Experimental Study of Natural Gas Flame Enriched by Hydrogen and Oxygen in a Coaxial Burner,” Appl. Therm. Eng., 108, pp. 287–295.

[91] Sanusi, Y. S., Mokheimer, E. M. A., Shakeel, M. R., Abubakar, Z., and Habib, M. A., 2017, “Oxy-Combustion of Hydrogen-Enriched Methane: Experimental Measurements and Analysis,” Energy and Fuels, 31(2), pp. 2007–2016.

[92] Qiu, L., Lee, T. H., Liu, L. M., Yang, Y. L., and Jacobson, A. J., 1995, “Oxygen Permeation Studies of SrCo0.8Fe0.2O3-D,” Solid State Ionics, 76(3–4), pp. 321–329.

[93] Qi, X. W., Lin, Y. S., and Swartz, S. L., 2000, “Electric Transport and Oxygen Permeation Properties of Lanthanum Cobaltite Membranes Synthesized by Different Methods,” Ind. Eng. Chem. Res., 39(3), pp. 646–653.

[94] van Hassel, B. A., Kawada, T., Sakai, N., Yokokawa, H., and Dokiya, M., 1993, “Oxygen Permeation Modelling of La1-YCayCrO3-D,” Solid State Ionics, 66, pp. 41–47.

[95] Yang, Z., and Lin, Y. S., 2002, “A Semi-Empirical Equation for Oxygen

Nonstoichiometry of Perovskite-Type Ceramics," Solid State Ionics, 150(3–4), pp. 245–254.

[96] Xu, S. J., and Thomson, W. J., 1999, "Oxygen Permeation Rates through Ion-Conducting Perovskite Membranes," Chem. Eng. Sci., 54(17), pp. 3839–3850.

[97] Wang, H., Cong, Y., and Yang, W., 2002, "Oxygen Permeation Study in a Tubular Ba0.5Sr0.5Co0.8Fe0.2O3- δ Oxygen Permeable Membrane," J. Memb. Sci., 210(2), pp. 259–271.

[98] Van Hassel, B. A., 2004, "Oxygen Transfer across Composite Oxygen Transport Membranes," Solid State Ionics, 174(1–4), pp. 253–260.

[99] Liu, S., and Gavalas, G. R., 2005, "Oxygen Selective Ceramic Hollow Fiber Membranes," J. Memb. Sci., 246(1), pp. 103–108.

[100] Tan, X., Pang, Z., Gu, Z., and Liu, S., 2007, "Catalytic Perovskite Hollow Fibre Membrane Reactors for Methane Oxidative Coupling," J. Memb. Sci., 302(1–2), pp. 109–114.

[101] Behrouzifar, A., Asadi, A. A., Mohammadi, T., and Pak, A., 2012, "Experimental Investigation and Mathematical Modeling of Oxygen Permeation through Dense Ba 0.5Sr 0.5Co 0.8Fe 0.2O 3-?? (BSCF) Perovskite-Type Ceramic Membranes," Ceram. Int., 38(6), pp. 4797–4811.

[102] Veynante, D., and Vervisch, L., 2002, "Turbulent Combustion Modeling," Prog. Energy Combust. Sci., 28(3), pp. 193–266.

[103] Versteeg, H. K., and Malasekara, W., 1995, *An Introduction to Computational Fluid Dynamics, the Finite Volume Method*, Longman Group Ltd, Essex.

[104] Poinsot, T., and Veynante, D., 2005, *Theoretical and Numerical Combustion*.

[105] Ducros, F., and Nicoud, F., 1999, "Subgrid-Scale Stress Modelling Based on the Square of the Velocity Gradient Tensor," Flow, Turbul. Combust., pp. 1–36.

[106] 2010, *Ansys Fluent Theory Guide*, Ansys Inc., Canonsburg.

[107] Dillon, D. J., Panesar, R. S., Wall, R. A., Allam, R. J., White, V., Gibbins, J., and Haines, M. R., 2005, "Oxy-Combustion Processes for CO2 Capture from Advanced Supercritical PF and NGCC Power Plant.," *Greenhouse Gas Control Technologies*, pp. 211–220.

[108] Joshi, N. D., Epstein, M. J., Durlak, S., and Marakovits, S., 1994, "DEVELOPMENT OF A FUEL AIR PREMIXER FOR AERO- DERIVATIVE DRY LOW EMISSIONS COMBUSTORS .," ASME Pap. 94-GT, 4, p. 253.

[109] Amato, A., Hudak, B., D'Carlo, P., Noble, D., Scarborough, D., Seitzman, J., and Lieuwen, T., 2011, "Methane Oxycombustion for Low CO[Sub 2] Cycles: Blowoff Measurements and Analysis," J. Eng. Gas Turbines Power, 133(6), p. 061503.

[110] Driscoll, J. F., 2008, "Turbulent Premixed Combustion: Flamelet Structure and Its Effect on Turbulent Burning Velocities," Prog. Energy Combust. Sci., 34(1), pp. 91–134.

[111] Cheng, R. K., Littlejohn, D., Nazeer, W. A., and Smith, K. O., 2008, "Laboratory

Studies of the Flow Field Characteristics of Low-Swirl Injectors for Adaptation to Fuel-Flexible Turbines," J. Eng. Gas Turbines Power, 130(2), p. 021501.

[112] Aliyu, M., Nemitallah, M. A., Said, S. A., and Habib, M. A., 2016, "Characteristics of H2-Enriched CH4-O2 Diffusion Flames in a Swirl-Stabilized Gas Turbine Combustor: Experimental and Numerical Study," Int. J. Hydrogen Energy, 41, pp. 20418–20432.

[113] Taamallah, S., Shanbhogue, S. J., and Ghoniem, A. F., 2016, "Turbulent Flame Stabilization Modes in Premixed Swirl Combustion: Physical Mechanism and Karlovitz Number-Based Criterion," Combust. Flame, 166, pp. 19–33.

[114] Porter, R., Liu, F., Pourkashanian, M., Williams, a., and Smith, D., 2010, "Evaluation of Solution Methods for Radiative Heat Transfer in Gaseous Oxy-Fuel Combustion Environments," J. Quant. Spectrosc. Radiat. Transf., 111(14), pp. 2084–2094.

[115] Rajhi, M. A., Ben-Mansour, R., Habib, M. A., Nemitallah, M. A., and Andersson, K., 2014, "Evaluation of Gas Radiation Models in CFD Modeling of Oxy-Combustion," Energy Convers. Manag., 81, pp. 83–97.

[116] Johansson, R., Leckner, B., Andersson, K., and Johnsson, F., 2011, "Account for Variations in the H2O to CO2 Molar Ratio When Modelling Gaseous Radiative Heat Transfer with the Weighted-Sum-of-Grey-Gases Model," Combust. Flame, 158(5), pp. 893–901.

[117] Sivathanu, Y. R., and Faeth, G. M., 1990, "Generalized State Relationships for Scalar Properties in Nonpremixed Hydrocarbon/Air Flames," Combust. Flame, 82(2), pp. 211–230.

[118] Zimont, V., Polifke, W., Bettelini, M., and Weisenstein, W., 2008, "An Efficient Computational Model for Premixed Turbulent Combustion at High Reynolds Numbers Based on a Turbulent Flame Speed Closure," J. Eng. Gas Turbines Power, 120(3), p. 526.

[119] Gaitonde, U., 2008, *Quality Criteria for Large Eddy*.

[120] Ufot, E., Lebele-Alawa, B. T., and Bob-Manuel, K. D. ., 2011, "Influence of Convection Heat Transfer Coefficient on Heat Transfers and Wall Temperatures of Gas-Turbine Combustors," Int. J. Appl. Sci. Technol., 1(6), pp. 210–218.

[121] Négishi, N., 1982, "Lean Premixture Combustion on a Coaxial Burner," Symp. Combust., 19(1), pp. 441–447.

VITAE

Name	:	Binash Imteyaz
Nationality	:	Indian
Date of Birth	:	02-Feb-1990
Email	:	binashahmad@kfupm.edu.sa ahmadatbit@gmail.com
Address	:	202-Manjushree Aptt. - C, Bank Road, Patna – 800 001, Bihar, India.
Academic background	:	Ph.D. (Mechanical Engineering), April 2019 King Fahd University of Petroleum & Minerals (KFUPM), Dhahran, Saudi Arabia.
		MSc (Mechanical Engineering), Dec. 2014 King Fahd University of Petroleum & Minerals (KFUPM), Dhahran, Saudi Arabia.
		B.Eng. (Production Engineering), Dec. 2012 Birla Institute of Technology, Mesra (BIT Mesra) Ranchi, India.

Publications :

- Imteyaz, B.A., Nemitallah, M.A. and Habib, M.A. Second law analysis of premixed and non-premixed oxy-fuel combustion cycle utilizing oxygen separation membranes (Submitted to J of Membrane Science)
- Imteyaz, B.A., Nemitallah, M.A. and Habib, M.A. Experimental and computational study on combustion and stability characteristics of CH_4-H_2-O_2-CO_2 premixed flames for gas turbine applications. (Submitted to Applied Energy)
- Imteyaz, B.A., Nemitallah, M.A. and Habib, M.A. Experimental and numerical investigations on the effect of combustion parameters on CH_4/H_2-O_2/CO_2 premixed flames. (Manuscript under preparation)
- Imteyaz, B.A., Nemitallah, M.A., Abdelhafez, A.A. and Habib, M.A., 2018. Combustion behavior and stability map of hydrogen-enriched oxy-methane

premixed flames in a model gas turbine combustor. International Journal of Hydrogen Energy, 43(34), pp.16652-16666.

- Abdelwahid, S., Nemitallah, M., Imteyaz, B., Abdelhafez, A. and Habib, M., 2018. Effects of H_2 Enrichment and Inlet Velocity on Stability Limits and Shape of $CH_4/H_2–O_2/CO_2$ Flames in a Premixed Swirl Combustor. Energy & Fuels, 32(9), pp.9916-9925.
- Imteyaz, B. and Zubair, S.M., 2018. Effect of pressure drop and longitudinal conduction on exergy destruction in a concentric-tube micro-fin tube heat exchanger. International Journal of Exergy, 25(1), pp.75-91.
- Imteyaz, B., Habib, M.A. and Ben-Mansour, R., 2017. The Characteristics of Oxycombustion of Liquid Fuel in a Typical Water-Tube Boiler. Energy & Fuels, 31(6), pp.6305-6313.
- Khalifa, A.E., Imteyaz, B.A., Lawal, D.U. and Abido, M.A., 2017. Heuristic Optimization Techniques for Air Gap Membrane Distillation System. Arabian Journal for Science and Engineering, 42(5), pp.1951-1965.
- Qasem, N.A.A., Imteyaz, B., Ben-Mansour, R. and Habib, M.A., 2017. Effect of Radiation Heat Transfer on Naturally Driven Flow Through Parallel-Plate Vertical Channel. Arabian Journal for Science and Engineering, 42(5), pp.1817-1829
- Imteyaz, B., Habib, M.A., Nemitallah, M.A. and Jamal, A., 2015. Investigation of liquid ethanol evaporation and combustion in air and oxygen environments inside a 25 kW vertical reactor. Proceedings of the Institution of Mechanical Engineers, Part A: Journal of Power and Energy, 229(6), pp.647-661.
- Imteyaz, B. and Habib, M.A., 2015. Study of Combustion Characteristics of Ethanol at Different Dilution With the Carrier Gas. Journal of Energy Resources Technology, 137(3), p.032205.
- Lawal, D.U., Imteyaz, B.A., Abdelkarim, A.M. and Khalifa, A.E., 2014. Performance of Spark-Ignition Engine using Gasoline-91 and Gasoline-95. International Journal of Innovative Science, Engineering & Technology, Vol. 1 Issue 6.

Conferences

- Qasem, N., Imteyaz, B., & Antar, M. A. (2016, November). Investigation of the Effect of the Top and the Bottom Temperatures on the Performance of Humidification Dehumidification Desalination Systems. In ASME 2016 International Mechanical Engineering Congress and Exposition (pp. V06AT08A051-V06AT08A051). American Society of Mechanical Engineers.
- Imteyaz, B. and Habib, M.A. “Study of combustion characteristics of ethanol oxy-combustion at different dilution with carrier gas”- ES-FuelCell2014-6514 – ASME 2014 8th International Conference on Energy Sustainability.